UNIVERSITÀ DEGLI STUDI DI PISA

FACOLTÀ DI SCIENZE MATEMATICHE, FISICHE E NATURALI
CORSO DI LAUREA MAGISTRALE IN FISICA

Study of Requirements and performances of the electromagnetic calorimeter for the Mu2e experiment at FermiLab

TESI DI LAUREA MAGISTRALE

Candidato **Gianantonio Pezzullo**

gianantonio.pezzullo@pi.infn.it

Relatore
Prof. Franco Cervelli,
Dott. Stefano Miscetti
Università di Pisa,
Laboratori Nazionali di Frascati
dell'INFN

Controrelatore
Prof. Flavio Costantini,
Prof. Francesco Forti
Università di Pisa

ANNO ACCADEMICO 2011/2012

Contents

Introduction

The aim of the Mu2e experiment is to measure the ratio between the rate of the neutrinoless, coherent conversion of muons into electrons in the field of a nucleus, and the rate of ordinary muon capture on the nucleus:

$$R_{\mu e} = \frac{\mu^- + A(Z, N) \rightarrow e^- + A(Z, N)}{\mu^- + A(Z, N) \rightarrow \nu_\mu + A(Z - 1, N)}. \tag{1}$$

The conversion process is an example of charged lepton flavor violation (CLFV). Thus far no CLFV interaction has been observed experimentally; the current best experimental limit on muon-to-electron conversion is from the SINDRUM II experiment, using a gold target [1]:

$$R_{\mu e} < 6.1 \times 10^{-13} \quad (90\%CL).$$

Figure (1) shows the history of charged lepton flavor violation searches in muon decays.
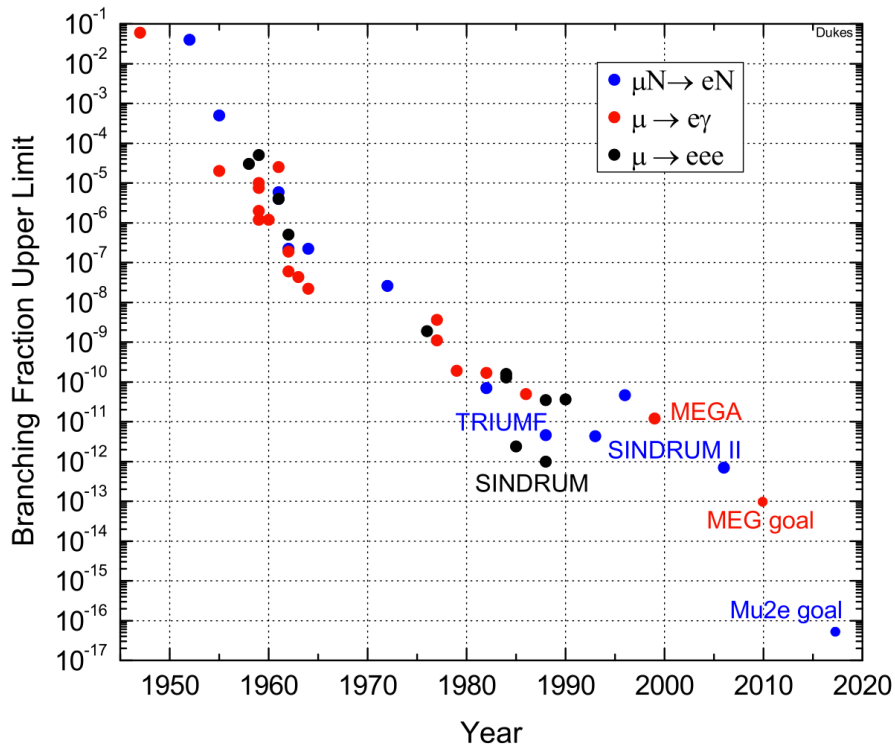
Figure 1: History of charged lepton flavor violation searches in muon decays. The MEG and Mu2e sensitivity goals are shown.

Mu2e intends to probe four orders of magnitude beyond the SINDRUM II sensitivity, measuring $R_{\mu e}$ with a sensitivity of 6×10^{-17} at 90% CL. When a muon is stopped in a target it rapidly (10^{-16} s) cascades down to the 1S state. Several processes can then occur, the most likely being muon decay-in-orbit, $\mu^- N_{A,Z} \rightarrow e^- \nu_\mu \bar{\nu}_e N_{A,Z}$, and

muon capture, $\mu^- N_{A,Z} \to \nu_\mu N_{A,Z-1}$, the former dominant for light nuclei and the latter dominant for heavy nuclei. Neutrinoless conversion of a muon into an electron, $\mu^- N_{A,Z} \to e^- N_{A,Z}$, results in an electron with an energy slightly less than that of the rest mass energy of the muon:

$$E_{CE} = m_\mu c^2 - B_\mu(Z) - C(A), \tag{2}$$

where Z and A are the number of protons and nucleons in the nucleus, B_μ is the atomic binding energy of the muon, and $C(A)$ is the nuclear recoil energy. In the case of muonic aluminum, $B_{\mu,1S}(13) = 0.48$ MeV, $C(27) = 0.21$ MeV, and $E_{CE}(Al) = 104.97$ MeV. This energy is well above the bulk of the dominant background, i.e. electrons from muon decay-in-orbit. Energy spectrum of the muon decay-in-orbit electron has a tail falling off as $(E - E_e)^5$ near the endpoint: only 3×10^{-13} of the electrons have an energy within 3 MeV of the endpoint energy. This gives muon-to-electron conversion a major experimental advantage over most other CLFV experiments, and makes it potentially the most sensitive of all.

In order to achieve a sensitivity of $\sim 10^{-17}$, in excess of 10^{18} muons must be stopped; roughly 50 billion per second in a two-year running period. A continuous muon beam, with its attendant pions and electrons, would produce unacceptably high detector rates and backgrounds. To mitigate this, in Mu2e experiment the muon beam is bunched with a separation of roughly twice the muon lifetime: 864 ns in Al. The detector is turned off for some 700 ns after the intense bunched beam impacts muon stopping target so to avoid the large flux of particles emanating from the target. Then the detector is turned on until the next bunch arrives. The experimental signature is an isolated 105 MeV energy electron exiting the stopping target 700 ns after the bunched beam arrival.

Chapter 1

About the muon conversion
$\mu + N \rightarrow e + N$

1.1 Charged Lepton Flavour Violation

Before the discovery of neutrino oscillations, it was generally understood that lepton flavor changing processes were forbidden in the Standard Model (SM) and that the lepton flavor numbers L_e, L_μ and L_τ were conserved. This is because neutrinos were taken to be massless, which trivially allows one to diagonalize the mass matrices for the charged leptons and neutrinos simultaneously. But neutrino oscillations allow mixing among the lepton families, giving rise to lepton flavor violating (LFV) processes. This will also be generically true for any model that includes a mechanism for generating neutrino masses. The rate at which LFV processes occur in the neutrino sector is constrained by the measured neutrino mixing parameters, but the rate at which charged lepton flavor violating (CLFV) occur is model dependent and can vary over many orders of magnitude. For example, in the minimal extension to the SM where neutrino mass is generated by introducing three right-handed SU(2) singlet fields and three new Yukawa couplings, the CLFV process $\mu^- N \rightarrow e^- N$ can only occur through loop diagrams whose amplitudes are proportional to $(\delta m_{ij}^2 / M_W^2)^2$ where δm_{ij}^2 is the mass-squared difference between the ith and jth neutrino mass eigenstates. Because the neutrino mass differences are so small relative to Mw the rates of CLFV decays in the modified SM are effectively zero (e.g. $< 10^{-50}$ for both $\mu^+ \rightarrow e^+\gamma$ and $\mu^- N \rightarrow e^- N$). On the other hand, many New Physics (NP) models predict significant enhancements to CLFV rates and to the $\mu^- N \rightarrow e^- N$ process in particular. In particular, many well-motivated physics models predict rates for CLFV processes that are within a few orders of magnitude of the current experimental bounds. These include the MSSM with right-handed neutrinos, SUSY with R-parity violation; models with leptoquarks, new gauge bosons, large extra-dimensions and a non-minimal Higgs sector [2]. The Mu2e experiment, with a single-event sensitivity of a few 10^{-17} for the ratio of $\mu^- N \rightarrow e^- N$ conversions to conventional muon captures, will have excellent discovery potential over a wide range of new physics models and could prove to be a powerful discriminant.

There is an active global program to search for CLFV processes using rare decays of muons, taus, kaons, and B-mesons. The ratio of rates among various CLFV processes is model dependent and varies widely depending on the underlying physics responsible. Thus, it is important to pursue experiments sensitive to different processes in order to elucidate the mechanism responsible for CLFV effects. The most stringent limits come from the muon sector because of the relative "ease" with which an intense source of muons can be produced. Three rare muon processes stand out: $\mu^+ \rightarrow e^+\gamma$, $\mu^+ \rightarrow e^+e^+e^-$ and $\mu^-N \rightarrow e^-N$. Searches for these processes have yielded null results and set upper limits on the corresponding rates. The experimental limits (all at 90% CL) on the branching ratios are: for B($mu^+ \rightarrow e^+\gamma$) $< 2.4 \times 10^{-12}$ [3], B($\mu^+ \rightarrow e^+e^+e^-$)$< 1.0 \times 10^{-12}$ [4], and B($\mu \rightarrow e$ conversion on gold) $< 7 \times 10^{-13}$ [5].

The MEG experiment [6], operating at PSI, has already reached 2.4×10^{-12} and hopes to achieve a sensitivity better than 10^{-13} for the $\mu^+ \rightarrow e^+\gamma$ branching ratio, while the proposed COMET [7] experiment at JPARC and Mu2e at Fermilab will reach sensitivities of 10^{-16} - 10^{-17} on R$_{\mu e}$(Al). It is important to note that these two processes have complementary sensitivity to new physics effects and the results from both are helpful in order to untangle the underlying physics. In fact the sensitivity of a given CLFV process can be achieved in a model independent manner by adding lepton-flavor-violating effective operators to the Standard Model Lagrangian:

$$L_{\text{CLFV}} = \frac{m_\mu}{(1+\kappa)\Lambda^2}\bar{\mu}_R\sigma_{\mu\nu}e_L F^{\mu\nu} + \frac{\kappa}{(1+\kappa)}\bar{\mu}_L\gamma_\mu e_L \left(\sum_{q=u,d}\bar{q}_L\gamma^\mu q_L\right) \qquad (1.1)$$

where Λ is the mass scale of new physics and κ is an arbitrary parameter controlling the relative contribution of the two terms [8]. Most new physics contributions are accounted for in these two classes of effective operators. If $\kappa \ll 1$, the first term, a dimension five magnetic-moment-type operator, is dominant. If $\kappa \gg 1$, the second term, a four-fermion interaction-type operator, is dominant. The first term arises from loops with an emitted photon. If the photon is real, one observes $\mu^+ \rightarrow e^+\gamma$. The second term includes contact terms and a variety of other processes not resulting in a photon. Therefore, $\mu^-N \rightarrow e^-N$ and $\mu^+ \rightarrow e^+e^+e^-$ processes are sensitive to new physics regardless of the relative contributions of the first and second terms. The new physics scale, Λ, to which these two processes are sensitive as a function of κ is shown in figure 1.1.

The projected sensitivity of the MEG experiment will probe Λ values up to 2000 - 4000 TeV for $\kappa \ll 1$ scenarios, while having little sensitivity for the case that $\kappa \gg 1$. The projected sensitivity of the Mu2e experiment will probe Λ values from 3000 to over 10000 TeV over all values of κ. It should be noted that these effective operators provide a good description of most of the new physics scenarios in which large CLFV effects might appear in $\mu^+ \rightarrow e^+\gamma$ and $\mu^-N \rightarrow e^-N$, and the conclusions regarding relative sensitivity are generically true. As demonstrated by figure 1.1, a Mu2e experiment sensitive to rates in the range of 10^{-16} - 10^{-17} is interesting and important in all MEG scenarios. If MEG observes a signal, then Mu2e should also, and the ratio of measured rates can be used to simultaneously constrain Λ and κ (limiting which types of new physics models remain viable). On the other hand, a null result from MEG does not preclude a Mu2e discovery since the new physics may be dominated by interactions to which the $\mu^+ \rightarrow e^+\gamma$ process is blind. An example of the complementary nature of these two processes in the context of a specific model is provided in figure 1.2, which depicts a scan of the parameter space of a Littlest Higgs Model with T-parity [9]. The different
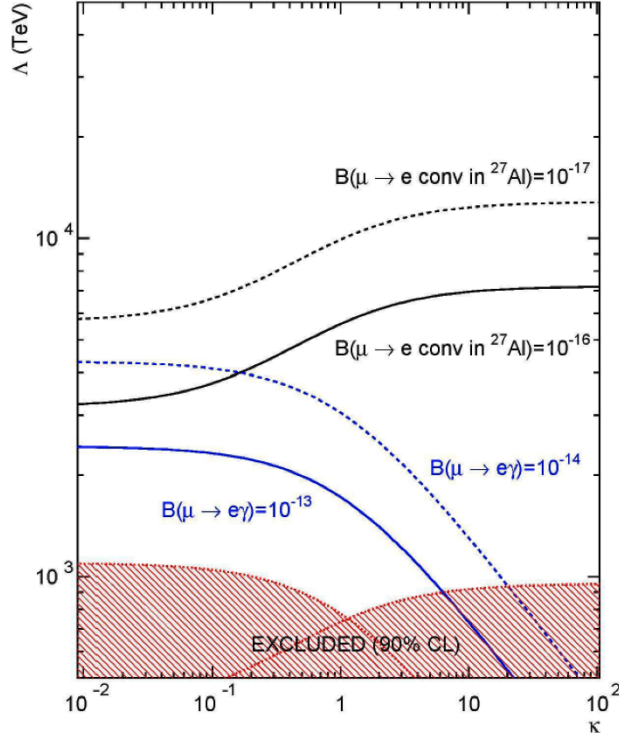
Figure 1.1: The sensitivity to the scale of new physics, Λ, as a function of κ, for a muon to electron conversion experiment with a sensitivity of 10^{-16} - 10^{-17} is compared to that for a muon-to-electron-gamma experiment with a sensitivity of 10^{-13} - 10^{-14}. The excluded region of parameter space, based on current experimental limits, is shaded.

colored points refer to different choices for the structure of the mirror-lepton mixing matrix that gives rise to the CLFV effects. The combination of results from MEG and Mu2e would severely constrain the allowed parameter space of this model and could distinguish between the Littlest Higgs Model and the Minimal Supersymmetric models in a transparent way, as the correlations between the two CLFV processes are significantly different in the two models.

1.2 The $\mu + N \rightarrow e + N$ process

When a negatively charged muon stops in a target it rapidly cascades down to the 1S state [10]. Capture, decay or conversion of the muon takes place with a mean lifetime that has been measured in various materials and ranges from less than ~100 ns (high-Z nuclei) to over 2 μs (low-Z nuclei) [11]. The conversion of a muon to an electron in the field of a nucleus is coherent: the muon recoils off the entire nucleus and the kinematics are those of two-body decay. The mass of a nucleus is large compared to the electron mass so the recoil terms are small. As a result neutrinoless conversion of a muon will produce an electron with an energy that is slightly less than the rest mass of the muon
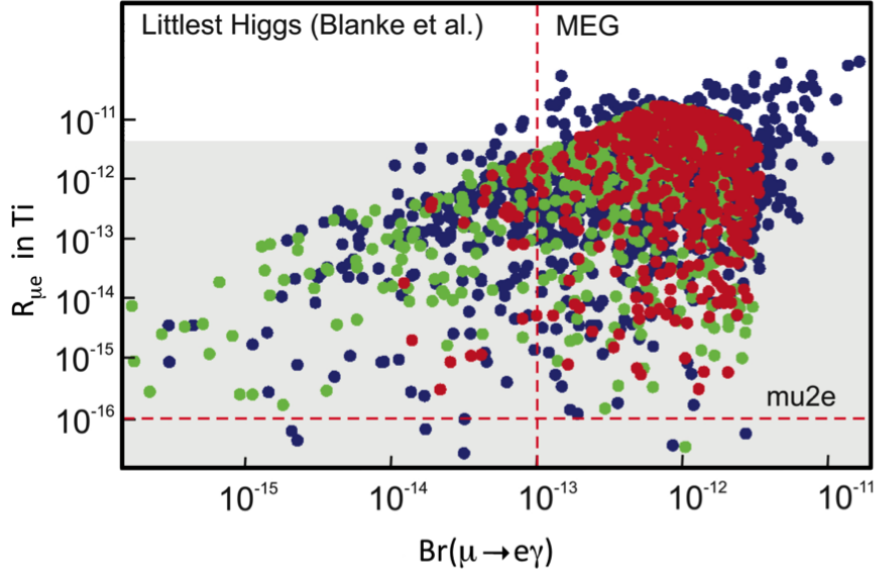
Figure 1.2: The predicted rate of muon to electron conversion in titanium is compared to the predicted branching ratio for $\mu^+ \to e^+\gamma$ in the context of the Littlest Higgs model with T-parity [9]. The red points assume that a PMNS-like matrix describes the mixing matrix of the mirror leptons, while the green points assume that a CKM-like Matrix describes the mixing. The blue points are a general scan of the parameters of the mirror lepton mixing matrix. The shaded region is the parameter space not excluded by current CLFV results in conversion experiments.

and depends on the target nucleus:

$$E_e = m_\mu \, c^2 - B_\mu(Z) - C(A) \qquad (1.2)$$

where Z and A are the number of protons and nucleons in the nucleus, B_μ is the atomic binding energy of the muon and C(A) is the nuclear recoil energy. In the case of muonic aluminum, the energy of the conversion electron is 104.97 MeV and the muon lifetime is 864 ns [11]. An electron of this energy signals the conversion. This distinctive signature has several experimental advantages including the near-absence of background from accidentals and the suppression of background electrons near the conversion energy from muon decays. For example the muon energy of 105.6 MeV is well above the maximum energy of the electron from muon decay (given by the Michel spectrum) at 52.8 MeV; hence, the vast majority of muon decays do not cause background.

1.2.1 Physics backgrounds

At the proposed Mu2e sensitivity there are a number of processes that can mimic a muon-to-electron conversion signal. The control of these potential backgrounds drives the overall design of Mu2e. Backgrounds result principally from five sources:

1. Intrinsic processes that scale with beam intensity; like muon decay-in-orbit (DIO) and radiative muon capture (RMC);

2. Processes that are delayed because of particles that spiral slowly down the muon beam line, such as antiprotons;

3. Prompt processes where the detected electron is nearly coincident in time with the arrival of a beam particle at the muon stopping target (e.g. radiative pion capture, pion and muon decay-in-flight);

4. Electrons or muons that are initiated by cosmic rays;

5. Fake events induced by additional activity in the detector from conventional processes.

A free muon decays according to the Michel spectrum with a peak probability at the maximum energy at about half the muon rest energy (52.8 MeV) is far from the 105 MeV conversion electron energy. Never the less, if the muon is bound in atomic orbit, the outgoing electron can exchange momentum with the nucleus and might have an energy (ignoring the neutrino mass) equal to that of a conversion electron. At the kinematic limit of the bound decay, the two neutrinos carry away no momentum and the electron recoils against the nucleus, simulating the two-body final state of muon to electron conversion. The differential energy spectrum of electrons from muon decay-in-orbit falls rapidly near the endpoint, approximately as $(E_{endpoint} - E_e)^5$. The spectrum of electron energies that results from muon decays in orbit in aluminum is illustrated in figure 1.3 where the most prominent feature is the Michel peak. But the nuclear recoil slightly distorts the Michel peak and gives rise to a small tail that extends out to the conversion energy. Because of the rapid decrease in the DIO rate as the electron energy approaches the endpoint, the background can be suppressed through adequate resolution on the electron momentum.

To date, there have been no experimental measurements of the DIO spectrum with sufficient sensitivity near the endpoint energy. In fact the rate is very low and an unprecedented muons fluxes are required. The shape of the spectrum near the endpoint is dominated by phase space considerations that are generally understood but important corrections to account for nuclear effects must also be included. The reliability of these corrections is untested by experiment. However, a number of theoretical calculations of the DIO spectra of various nuclei have been done over the years, in particular a recent one by Czarnecki, et al. [12] The uncertainty in the rate versus energy near the endpoint is estimated at less than 20%.

Radiative muon capture on the nucleus ($\mu^-Al \rightarrow \gamma\nu Mg$) is an intrinsic source of high energy photons that can convert to an electron-positron pair in the stopping target or other surrounding material, producing an electron near the conversion electron energy. Photons can also convert internally. These internal and external rates, by numerical accident, are approximately equal for in Mu2e stopping target configuration. Because the energy of photons from RMC is shifted by the difference in mass of the initial and final nuclear states, the stopping target can be chosen so that the minimum masses of daughter nuclei be all at least a couple of MeV/c^2 above the rest mass of the stopping target nucleus. In this way the RMC photon energy is pushed below the conversion electron energy: as an example, for aluminum the RMC endpoint energy is 102.4 MeV, about 2.6 MeV below the conversion electron energy. The shape of the photon spectrum and the rate of radiative muon capture are not well known for medium mass nuclei and no experimental observation is available for events near the kinematic endpoint. Anyway the electrons resulting from photon conversions cannot exceed the RMC kinematic
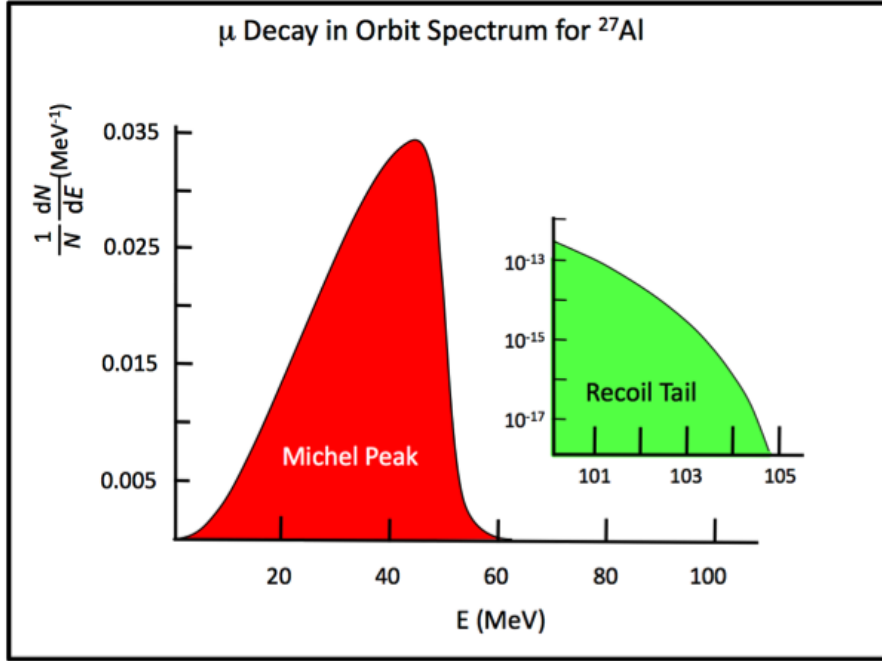
Figure 1.3: The electron energy spectrum for muon decay-in-orbit in aluminum. The recoiling nucleus results in a small tail (blown up on the right) that extends out to the conversion energy.

endpoint allowed by the energy of the radiated photon.

Most low-energy muon beams have large pion contaminations. Pions can produce background either when they are captured in the stopping target or surrounding material (producing a high energy photon through radiative pion capture (RPC)) and also via decay-in-flight.

Radiative pion capture belongs the following process:

$$\pi^- N \to \gamma N^* \tag{1.3}$$

RPC account for 2.1% of pion captures in aluminum target. The kinematic endpoint is near the pion rest mass energy with a broad distribution that peaks at about 110 MeV. The photon can mimic electron near the conversion energy, as in the case of the RMC. In addition, the photon can internally convert:

$$\pi^- N \to e^+ e^- N^* \tag{1.4}$$

Thus electrons resulting from photon conversions, both internal and external, can produce background. RPC background can be suppressed with a pulsed primary proton beam, so to delay the search for conversion electrons until virtually all pions have decayed or annihilated in material.

A negative pion with momentum larger than 56.5 MeV/c can decay to an electron with an energy above 103.5 MeV through the decay channel

$$\pi^- \to e^- \nu_e$$

10
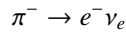
The electron from the decay can be mistaken for a conversion electron if it is produced by the decay of an out-of-time pion that arrives during the data taking of the detectors.

Beam electrons near the conversion energy that scatter in the target, along with the decay-in-flight decay of a muon in the region of the stopping target are other examples of prompt backgrounds. A negative muon with momentum larger than 76.7 MeV/c can decay to an electron with energy above 103.5 MeV through normal muon decay-in-flight. The electron can be mistaken for a conversion electron if it is produced by a muon that arrives during the measurement period and decays in the vicinity of the stopping target. Also the antiprotons will quickly annihilate and produce a ~ 2 GeV shower of secondary particles including pions, kaons, neutrons, protons, electrons, positrons, and gamma rays. An electron near 105 MeV can be produced directly in the annihilation, through the decay of secondary particles, or through the interaction of secondaries in the stopping target or other nearby material, faking a conversion electron.

Cosmic rays (electrons, muons) are a potential source of electrons near the conversion electron energy. If such electrons have trajectories that appear to originate in the stopping target they can fake a muon conversion. Identifying an incoming cosmic ray particle can reject these events. Passive shielding and veto counters around the spectrometer help to suppress this background. Note that this background scales with the experiment's live time rather than with beam intensity.

Additional activity in the detector primarily originates from the muon beam, from multiple DIO electrons within a narrow time window, and from muon capture on a target nucleus that results in the emission of photons, neutrons and protons. The protons ejected from the nucleus following muon capture have a very small kinetic energy and are highly ionizing, so the large pulses they leave behind in the detectors can shadow hits from low energy electrons. Ejected neutrons can be captured on hydrogen or other atoms and produce low-energy photons. Electron-generated hits caused by neutron-generated photons are the most common and difficult to remove form of background activity. The rate of background activity scales linearly with beam intensity. The momentum resolution tails depend roughly linearly on the rate of additional detector activity. The scaling rates can be controlled through careful design of the detector and reconstruction software, and by using estimates of event reconstruction quality when selecting physics samples.

Chapter 2

The Mu2e Experiment

Introduction

In this chapter the experimental set-up and performance are presented. The design of the experiment was driven by both, the sensitivity goal and the experimental backgrounds that can afflict the detectors. The chapter is organized as follow:

1. in sec. (2.1) starting from the goal of a Single Event Sensitivity of $\approx 10^{-17}$ an estimation of the total number of protons needed for the experiment is given;

2. in sec. (2.2) the experimental set-up of Mu2e is presented;

3. in sec. (2.6) a qualitative and quantitative discussion of how this set-up remove the different backgrounds is showed.

2.1 Sensitivity

The goal of the Mu2e Experiment is to reach a factor 10^4 of improvement over world's previous best results rom the SINDRUM II experiment [13, 5], so Mu2e should reach a Single Event Sensitivity of $\approx 10^{-17}$. This will give to Mu2e a discovery sensitivity over a very broad range of New Physics Models: SuperSymmetry, LittleHiggs, Leptoquarks, Extended Technicolor, Extra Dimensions [14].

Starting from the SES definition is possible to give an estimation of the number of muons necessary for this goal. The Single Event Sensitivity ("SES") is defined as that branching ratio for which the expected number of events using whatever cuts have been determined by other considerations will be one event. The algorithm is:

1. For a given acceptance, calculate the expected number N_{CE} of signal events (Conversion electrons) detected, assuming that every nuclear capture of a $\mu^- \, stopped$ ends with that muon converting to a Conversion Electron;

2. the SES is equal to $\frac{1}{N_{CE}}$

So to achieve a SES of about $\approx 10^{-17}$ a total number of $\approx 10^{17}$ μ^- must be detected. The total number of protons needed depends from many machine parameters: the acceptance and the ratio between proton-on-target and stopped μ^-. Based on Mu2e project, preliminary results [14] set the efficiency at 5.25% and the ratio μ^-stopped / POT at (0.0016 ± 0.0004); From these values follows that the total number of protons-on-target is:

$$
\begin{aligned}
POT \quad &= \quad \frac{1}{\mu^- - stopped/POT \times SES \times efficiency \times capture - fraction} \\
&= \quad \frac{1}{0.0020 \times (10^{-17}) \times 0.2 \times 0.609} \\
&\approx \quad 1.6 \times 10^{20}
\end{aligned}
$$

where the *capture − fraction* [15] represent the fraction of stopped muons that undergo in capture process.

The Single Event Sensitivity is a very clean concept but is useless as an optimization target: it does not explicitly depend on the expected background, so it is unsuitable to optimize on, because that would inevitably pull the configuration and cuts in the direction of maximal number of accepted events, at the expense of arbitrarily large inflation of the background event expectation. In chapter (5) a discussion about the "best" figure of merit that can drive the experiment optimization is reported.

2.2   Experimental Setup

The Mu2e apparatus (see figure (2.1)) is conceptually identical to the MECO design proposed at Brookhaven [16]. It is characterized by three solenoidal magnets: the Production, Transport, and Detector solenoids, with fields ranging from 5.0 T at the far end of the Production Solenoid to 1.0 T at the opposite end of the detector solenoid. 8 GeV proton bunches enter the Production Solenoid and impact a water-cooled Tungsten target. Pions are produced, which decay into muons, and some are captured in the graded field of the Production Solenoid and reverse direction, spiraling into the Transport Solenoid. The Transport Solenoid is curved in order to prevent line of sight transport of gammas and neutrons to the stopping target and to separate the positively and negatively charged particles. A collimator at the midpoint of the Transport Solenoid removes the positively charged particles. Exiting from the Transport Solenoid, the negative muons reach the Detector Solenoid, where the 17 (0.2 mm thick) Al foils, forming the stopping target, are located. Approximately 0.25% of the protons impacting the production target produce muons that are captured in one of the 17 Al foils of the stopping target. Since the stopping target is in a graded magnetic field, particles emitted backward from the stopping target have their directions reversed.

Downstream the stopping target there are: 1) a proton absorber, 2) tracking system (the primary momentum measuring device), 3) an electromagnetic calorimeter (used to trigger and to provide energy and position measurements for comparison with the tracker response), and a neutron absorber (surrounding all the detectors area). The detectors sit in an evacuated vessel inside the 1 T field of the Detector Solenoid. The Mu2e detector has been designed:
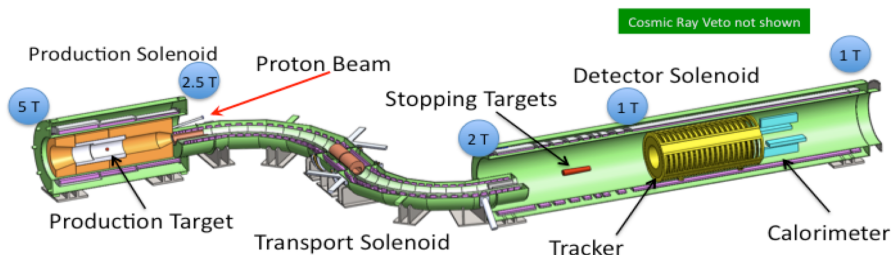
Figure 2.1: Layout of the Mu2e apparatus. The proton beam enters the Production Solenoid from the left, and muons are collected and transported via the Transport Solenoid to the Detector Solenoid.

- to ensure that the intense non-stopped beam from the production target is transported with minimal interactions to a beam stop at the end of the Detector Solenoid;

- to minimize the detector acceptance for electrons from backgrounds such as muon decay-in-orbit;

- to have excellent momentum resolution (better than 1MeV for $\sim$ 100 MeV/c electrons).

On the following sections an accurate description of the three superconducting solenoids is given.

2.2.1 Production Solenoid

Figure 2.2 shows the Production Solenoid: it is a relatively high field solenoid with an axial grading that varies from 4.6 Tesla to 2.5 Tesla. The Production Solenoid houses the production target. The purpose of the Production Solenoid is to trap charged pions escaping the production target and direct them towards the Transport Solenoid. In the Production Solenoid the uniform, axially graded magnetic field is obtained by using three solenoid coils with 3, 2 and 2 layers of aluminum stabilized NbTi superconducting cable: each coil has the same inner diameter. Aluminum stabilizer is used to reduce both the weight of the solenoid and the amount of nuclear heating around the conductor. Nuclear heating can result from the large flux of secondaries from the production target. Furthermore this high current, low-inductance cable allows efficient energy extraction during a quench, and fewer layers are required to reach the requested field strength. Furthermore this cable minimizes thermal barriers between the conductor and cooling channels. Protons enter the Production Solenoid through a small port on the low field side of the solenoid and intercept the production target. Remnant protons that are not absorbed by the target and very forward-produced secondary particles exit at the high field end of the solenoid. Pions in the forward direction with angles greater than ~30°, relative to the solenoid axis, are reflected back by the higher field and move along with the backward produced particles in helical trajectories towards the Transport Solenoid.
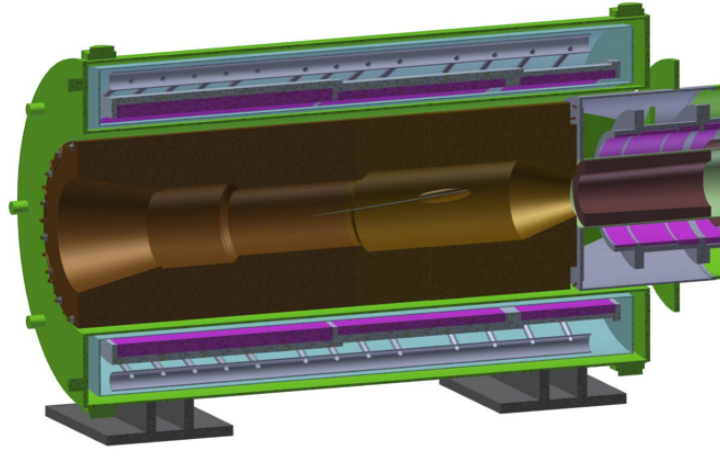
Figure 2.2: The Mu2e Production Solenoid. The beam tube for the incoming proton beam is shown in the upper right.

2.2.2 Transport Solenoid

The S-shaped Transport Solenoid (see figure 2.3) consists of a set of superconducting solenoids and toroids. These magnets generate forming a magnetic channel where low energy negatively charged muons travel with helical trajectories from the Production Solenoid to the Detector Solenoid.

Negatively charged particles with high energy, positively charged particles and line-of-sight neutral particles are almost all eliminated by absorbers and collimators before reaching the Detector Solenoid. Selection of negatively charged muons is accomplished by toroids where positives and negatives drift in opposite directions. Most of the positively charged particles are absorbed in the central collimator. To minimize the transport of particles spending a too long time in the magnetic system, the field in the straight, central sections has a negative gradient. This eliminates traps, where particles may bounce between local maxima in the field until they eventually scatter out and reach the Detector Solenoid at late time. The requirement on a negative gradient is relaxed in the curved sections of the TS because bouncing particles will eventually drift vertically out of the clear bore so to be absorbed by surrounding material.

2.2.3 Detector Solenoid

The Detector Solenoid (see figure (2.4)) is a large, low field magnet that houses the muon stopping target and the detection system devoted to identify and analyze conversion electrons. The muon stopping target resides in a graded field that varies from 2 Tesla to 1 Tesla. Conversion electrons, that are emitted in the direction opposite the detection system, are back reflected by the graded field; furthermore the graded field shifts the pitch of beam particles entering the Detector Solenoid, so to subtract a dangerous background. The actual detector components reside in an uniform field region. The inner bore of the Detector Solenoids is evacuated to 10^{-4} Torr to limit backgrounds from particle-gas interactions.
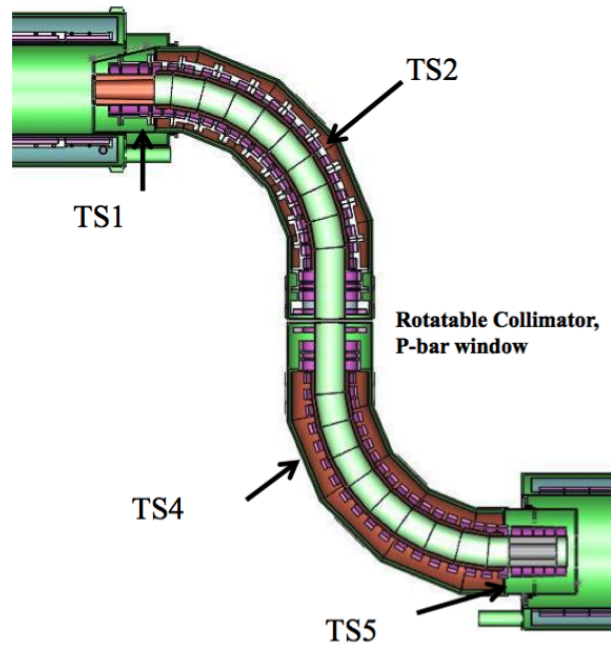
Figure 2.3: The Mu2e Transport Solenoid: the red circle is around the central collimator.

The graded and uniform field sections of the Detector Solenoid are wound on separate mandrels but housed in a common cryostat. The conductor is aluminum stabilized NbTi. The gradient is achieved by introducing spacers to effectively change the winding density of the superconducting cable.
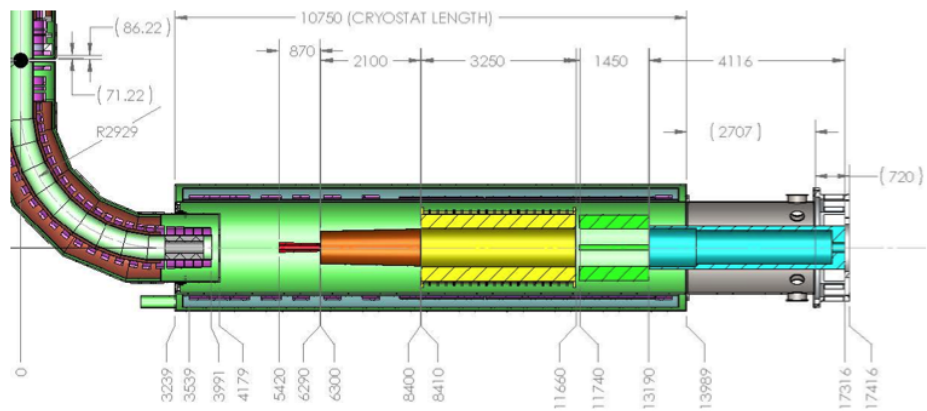

Figure 2.4: The Mu2e Detector Solenoid. The upstream section has a graded field to capture more conversion electrons. The downstream section has a uniform field in the region occupied by the detector elements.

2.3 Muons beam

As previously showed in Section (2.1) Mu2e requires $\approx 10^{17}$ negatively charged muons to be detected. In order to efficiently transport muons, minimize scattering with residual gas molecules, minimize multiple scattering of conversion electrons and prevent electrical discharge from detector high voltage, the Muon Beamline must be evacuated to the level of 10^{-4} Torr [14]. Muon Beamline can be divided into three main parts:

1. Production and collection;

2. Transport and selection;

3. The stopping targets.

2.3.1 Production and collection in the Production Solenoid

The evaluation of particle fluxes in the muon beam are based on GEANT-4 [17] simulations of proton interactions in a Tungsten target. GEANT-4 [17] has a variety of hadron interaction codes and the cross sections and kinematic distributions can vary significantly between them; QGSP-BERT [18] is the specific physics list of GEANT-4 [17] that actually is used in the Mu2e framework. In order to reduce exposure to the uncertainty in the hadronic models of low energy hadron production, the results from GEANT-4 [17] have been normalized to data from the HARP experiment [19] and checked successfully with the results from the SERP experiment at Novosibirsk [20]. Pions originated by the proton-target interactions are trapped in the magnetic field gradient so to allow the collection of the muons (from the pions decays) in the downstream part of the Production Solenoid, where a copper collimator provides a first charge and momentum selection and links the Production Solenoid with the Transport Solenoid.

2.3.2 Transport and selection of μ^- along the TS

The S-shaped Transport Solenoid filters unwanted charged and neutral particles from the beam. A set of three collimators is positioned along this solenoid: the first links the Production Solenoid with the Transport Solenoid, the second is in the middle of the TS and the last is in the downstream part, just in front of the Detector Solenoid. The three collimators are very similar in composition (essentially copper) and shape. The collimators in the Transport Solenoid are designed to suppress the transport of particles with momenta above 100 MeV/c, allowing the suppression of either the flux of electrons produced in the Production and Transport Solenoids and also the antiprotons produced in the Production Solenoid.

These beam electrons can be produced in the production target, primarily through π^0 production followed by conversion of the decay photons. They can also be produced by decays or interactions of beam particles. The antiprotons represent a very dangerous background for all the detector system, because when an antiproton annihilates it produces ≈ 2 GeV of particles shower. So an antiproton target is located in the cen-

tral collimator such to reduce the antiphons flux that can reach the Detector Solenoid
.

2.3.3 The stopping targets in the Detector Solenoid

The muon stopping target consists of 17 circular aluminum foils that are arranged coaxially. They are equally spaced (50 mm) and have a thickness of 0.2 mm. The radii range from 83 mm to 65 mm and are tapered with decreasing radii in the direction of decreasing magnetic field. The position of the target in the Detector Solenoid is such that in the first foil the magnetic field is 1.57 T and at the last is 1.30 T. The foils are designed to be massive enough to stop a significant fraction of the incident muon beam but not so massive to corrupt the momentum measurement of conversion electrons that emerges: low energy muons allow thin targets. The momentum distribution of muons at the Mu2e stopping target is shown in figure (2.5). Aluminum was selected as target
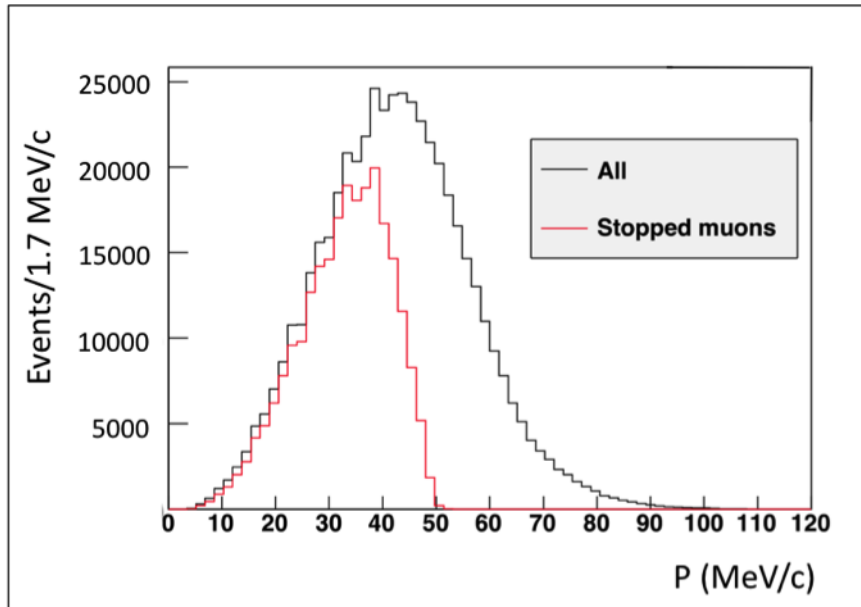

Figure 2.5: Particle momentum at the Mu2e stopping target. The black curve is the momentum of all muons that reach the stopping target, while the red curve is the momentum spectrum of muons that stop in the target.

material for two main reasons:

- Al, instead of other materials, does not suffer oxygen contamination that can lead to a severe background (oxygen has a lower Z and therefore than aluminum the endpoint of the muon decay-in-orbit spectrum is higher [12]);

- The lifetime of the muon in the Al target (864 ns) is long so that a significant fraction of muons decay after 700 ns, but it is also short enough that most of the

muons decay before the arrival of the following (pulses time distance: 1700 ns, see figure (2.6)).
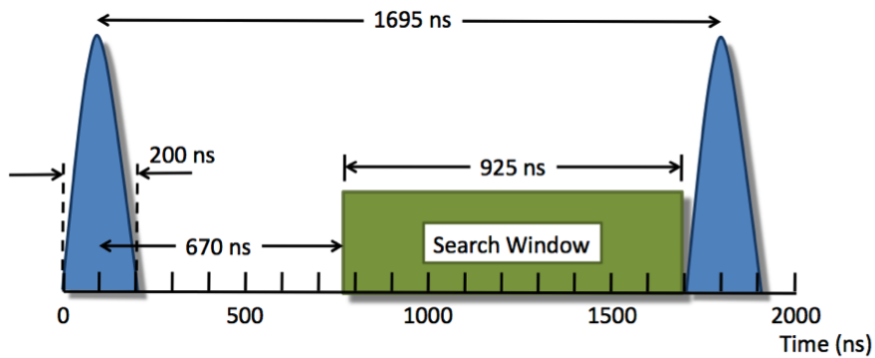

Figure 2.6: The Mu2e spill cycle for the proton beam and the delayed search window that allows for the effective elimination of prompt backgrounds.

The number of muons that reach and stop in the Al targets depends on a number of factors, like: the target material and geometry, the proton beam energy, the magnetic field in the Production and Transport Solenoids, the clear bore of the solenoids and the design of the collimators. In the chosen experimental configuration 0.0016 ± 0.0004 stopped μ^- are expected per each proton. The overall uncertainty on the stopped muon rate is conservatively estimated to be at the 25% level [14].

2.4 Detectors shielding

2.4.1 Proton absorber

The proton absorber (see figure (2.7)) is a tapered cylindrical shell 0.5 mm thick of high-density polyethylene (HDPE) with a radius slightly smaller than the inner radius of the tracker. The proton absorber is 210 cm in length and extends from the end of the stopping target to the beginning of the tracker. The design of the proton absorber was optimized to reduce the rate of protons, reaching the tracker while minimizing energy loss and scattering of conversion electrons crossing the absorber [14].
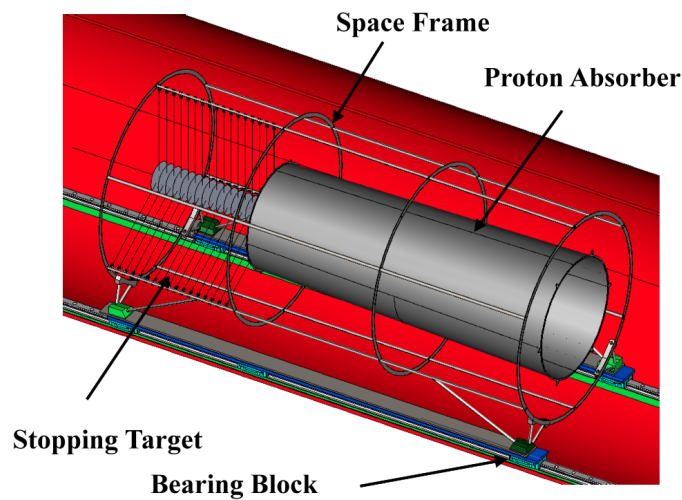
Figure 2.7: The proton absorber, stopping target and stainless steel space frame that supports the target and proton absorber.

2.4.2 Muon Beam Stop

The purpose of the Muon Beam Stop is to absorb the energy of beam particles reaching the downstream end of the Detector Solenoid to minimize the rate of accidental particles due to muons decay and, at the same time, captures in the Beam Stop. The Muon Beam Stop is located within the warm bore of the Detector Solenoid, downstream of the calorimeter (see figure (2.8)). The Muon Beam Stop consists of several cylinders of different materials: stainless steel, lead and HDPE.
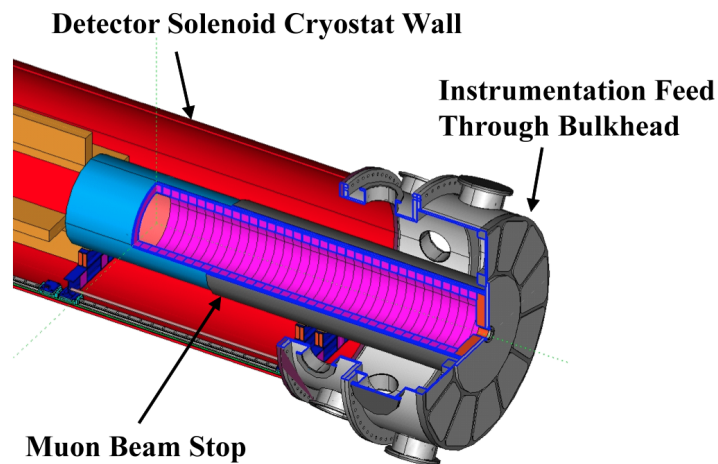
Detector Solenoid Cryostat Wall

Instrumentation Feed Through Bulkhead

Muon Beam Stop

Figure 2.8: The proton absorber, stopping target and stainless steel space frame that supports the target and proton absorber.

2.4.3 Neutron absorber

Absorbers (see figure (2.9)) must be placed around the Detector Solenoid to limit the number of neutrons (from the sopping targets) reaching the Cosmic Ray Veto. These absorbers surround the Detector Solenoid vacuum enclosure and will be supported independently from the Detector Solenoid. The Absorbers mainly consist of concrete blocks. The blocks include magnetic steel reinforcement bars and brackets [21]. An analysis is in progress to determine if steel parts so close to the DS solenoid field are acceptable.
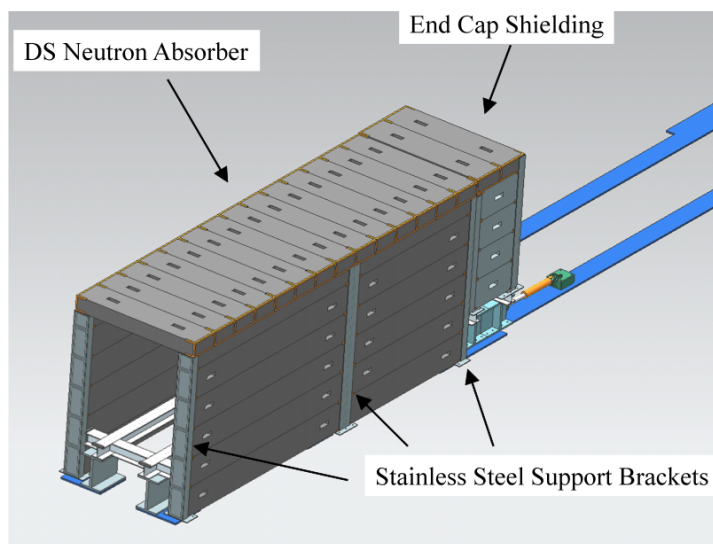

DS Neutron Absorber

End Cap Shielding

Stainless Steel Support Brackets

Figure 2.9: Overall view of Neutron Absorbers and Shielding.

2.5 Detector

The Mu2e detector is located inside the evacuated warm bore of the Detector Solenoid in a uniform 1 Tesla magnetic field and is designed to efficiently and accurately identify the helical trajectories of ~105 MeV electrons in the high, time varying rate environment of Mu2e. The detector consists of a tracker and a calorimeter that provide redundant energy/momentum, timing, and trajectory measurements. A cosmic ray veto, consisting of both active and passive elements, surrounds the Detector Solenoid.

2.5.1 Tracker

The Mu2e tracker is designed to accurately measure the trajectory of electrons in a uniform 1 Tesla magnetic field in order to determine their momenta. The limiting factor in trajectory reconstruction is the electron multiple scattering in the tracker. High rates in the detector may lead to errors in pattern recognition so reducing the acceptance for signal events. Errors in pattern recognition may also generate backgrounds, if hits from lower energy particles combine to create trajectories that are consistent with conversion electrons. Therefore a low mass, highly segmented detector is required to minimize multiple scattering and handle the high rates.

Mu2e Tracker (T-tracker, see figure (2.11)) is an array of straw drift tubes aligned transversely to the axis of the Detector Solenoid. The basic detector element is a 25 μm sense wire inside a 5 mm diameter tube made of 15 μm thick metalized Mylar. The tracker will have ~22,000 straws distributed into 18 measurement planes across a ~3 m length. Planes are constructed from two layers of straws, as shown in figure (2.10), to improve efficiency and to determine on which side of the sense wire a track passes (the classic "left-right" ambiguity). A 1 mm gap is maintained between straws to allow for manufacturing tolerance and diameter expansion due to gas pressure. The straws are designed to withstand changes in differential pressure ranging from 0 to 1 atmosphere for operation in vacuum. The straws are supported at their ends by a ring at large radius, outside of the active detector region.
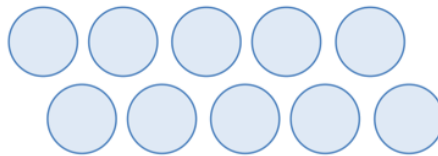
Figure 2.10: A section of a two-layer tracker straw plane. The two layers improve efficiency and help resolve the left-right ambiguity.

Each straw will be instrumented on both ends with preamps and TDCs so to measure the drift time and consequently determining the distance of the charged tracks from the drift wire. The arrival time of the signal at each end of the straw will measure the location of the track intercept along the length of the straw. Each straw will also be instrumented with an ADC for dE/dx measurement so to separate electrons from highly ionizing protons. To minimize feed-through into the vacuum, digitization will be done
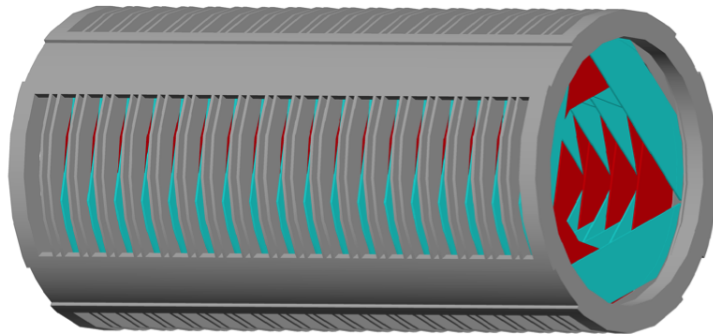
Figure 2.11: The Mu2e straw tube tracker. The straws are oriented transverse to the solenoid axis.

at the detector, with readout via optical fibers. A liquid cooling system will be required to maintain an appropriate operating temperature of the electronics in vacuum.

The tracker is designed to intercept only a small fraction of the significant flux of electrons from muon decays-in-orbit. The inner radius of the tracker planes is such that only electrons with energies greater than about 53 MeV will be observed in the tracker. Lower energy electrons will curl in the field of the Detector Solenoid and pass unobstructed through the hole in the center of the tracker. Just for this reason the vast majority (97%) of electrons from muon DIO, that are usually below 60 MeV (see figure 2.12), will not reach on the tracker. This is illustrated in figure 2.12.

Tracker resolution is very important in determining the level of several critical backgrounds. The tracker is required to have a momentum resolution better than 180 keV [22]. The requirement on the low-side tail is less stringent since it smears background away from the signal region, while a high-side tail smears background into the signal region. Current simulations indicate that the high side resolution of the Mu2e tracker can be well represented by the sum of two Gaussians. The high-side resolution has a core component sigma of 115 KeV/c, and a significant tail sigma of 176 KeV/c. The net resolution is significantly smaller than the one, due to energy loss in the upstream material.

2.5.2 Calorimeter

The Mu2e calorimeter supplies energy, position, and timing information on tracks that have been reconstructed by the tracker. Calorimeters and tracking devices use different technologies and physical processes to measure the required physical quantities, so the sources of error from the two systems are quite different. These different but redundant measurements help to eliminate backgrounds and provide a cross check to verify the validity of signal events. The calorimeter could also provide a fast trigger for high energy electron candidates, reducing the throughput requirements on the data acquisition system. A detailed description of the calorimeter is presented in the chapter (3) .
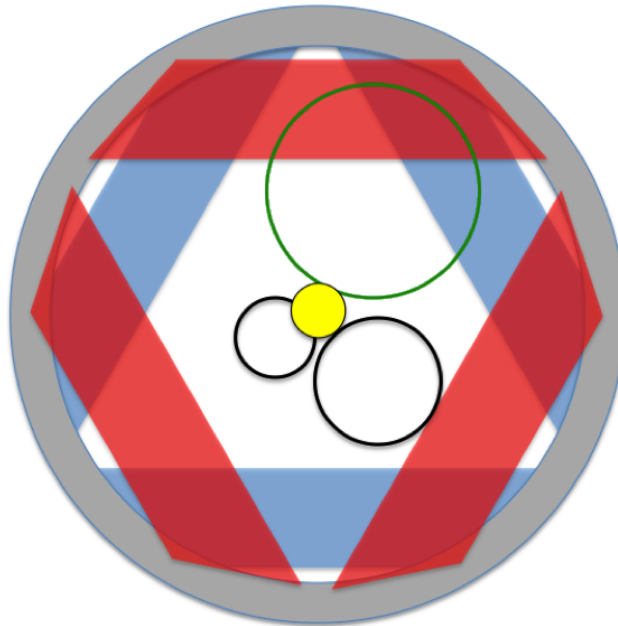
Figure 2.12: Cross sectional view of the Mu2e tracker with the trajectories of a 105 MeV conversion electron (top) and a 53 MeV Michel electron (lower right) superimposed. The disk in the center is the stopping target. Electrons with energies smaller than 53 MeV (lower left), representing most of the rate from muon decays-in-orbit, miss the tracker entirely.

2.5.3 Cosmic Ray Veto

Cosmic-ray muons hitting the muon stopping target and other materials in the detector region can produce delta rays that may have the right energy and may fall within the detector acceptance, so producing conversion-like background events. Cosmic ray muons can also decay, producing electrons that could mimic a conversion signal. The background from cosmic rays is directly proportional to the live time of the experiment, so the first protection level is the pulsed beam structure and the restricted time window to accepted events. Passive shielding, including either the overburden above and on the sides of the detector enclosure, either the neutron shield surrounding the Transport and Detector Solenoids, eliminates background sources other than penetrating muons. Muons cannot be suppressed, but have to be identified. The Veto will consist of three layers of extruded scintillator bars with embedded wavelength shifting fibers that are read out with Silicon photomultipliers (SiPMs). The CRV surrounds the Detector Solenoid on 3 sides (figure (2.13)) and extends up to the midpoint of the Transport Solenoid.

Approximately one conversion-like event per day from cosmic-ray muons is expected: the design of the cosmic ray veto was performed such to reduce that rate to 0.05 events during the entire running period.The Veto signal corresponds to coincident hits in two-out-of-three layers. In the region of the muon stopping target the Cosmic Ray Veto is 99.99% efficient.
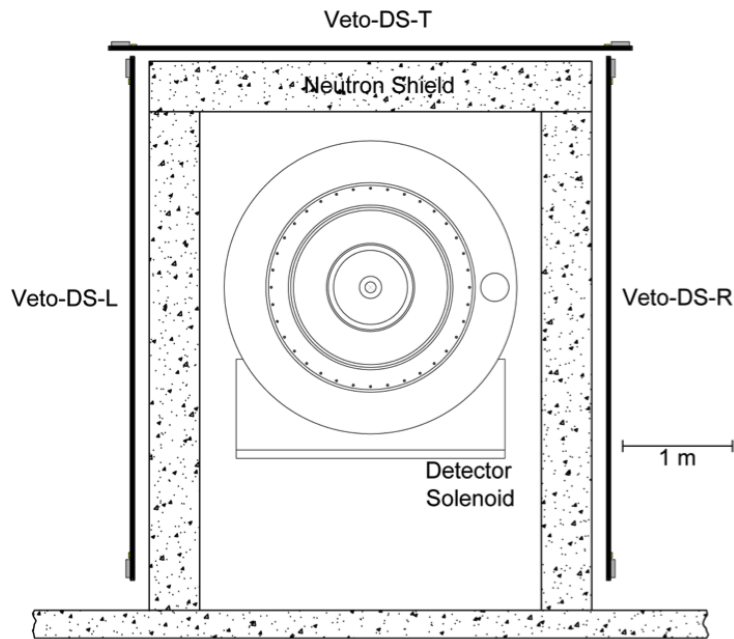
Figure 2.13: View of the Cosmic Ray Veto.

The Cosmic Ray Veto is designed also to survive an intense neutron flux coming primarily from the muon stopping target. Most of the neutrons have kinetic energies below 10 MeV, with the most probable energy about 1 MeV. Studies [14] show that the rate in the counters comes primarily from gammas that are produced from neutron capture on hydrogen. Passive shielding outside the Transport and Detector Solenoids will moderate and capture most of the neutrons. The magnitude and pattern of energy deposition in multiple layers of scintillator is expected to be different for neutrons and muons, which can further help to eliminate false veto signals from neutrons.

2.6   Background estimation

The known processes that may create electrons with energy equal to the one from muon conversion were discussed in general in section (1.2.1). In this section an estimate of these expected backgrounds is reported. The presented numbers for backgrounds are based on full reconstruction and cuts are made on reconstructed quantities. The reconstruction algorithm is still in its infancy and Mu2e is actively studying improvements to the algorithm as well as using it to improve the detector design.

For calculating all the different contributes a signal window of 103.5 to 104.7 MeV/c for the reconstructed momentum (p) was defined. This momentum range was chosen in order to optimize the crude figure-of-merit of $S/\sqrt{B}$, where S is the signal and B is the total background.

Mu2e has developed an algorithm to find and reconstruct electron tracks using just the tracker information; this algorithm was performed in order to achieve a momentum resolution as good as possible, so to minimize the number of electrons reconstructed with higher momentum. The track reconstruction uses the straw hit position, time, measured pulse height, and time division along the straws to separate signal hits from background. Hits consistent in time and space coming from a helix are collected and fit using successively more accurate algorithms, culminating in a Kalman filter fit [14]. Tracks are selected based on their measured parameters and fit quality.

Figure 2.14 shows the overall acceptance of 5.25%. The main cuts are:

1. Events in the live gate, which leaves 51%. The live gate begins ~700 ns after the proton pulse and ends when the next proton pulse arrives. This is required to remove pions that can produce radiative pion capture;

2. More than twenty straw hits used in the fit;

3. The "pitch cut" described elsewhere in the text ("reco pitch" in figure 2.14) is made after the twenty active hit cuts. One loses about another factor of two in acceptance. The active hit cut strongly selects for events in the pitch range and as a result the pitch cut does not appear to have a large effect in the figure. The pitch cut is defined by $0.5 < \cos\theta$ ($= p_z/p$, where p_z is the component along the solenoid axis) < 0.707, or $0.7 < p_T/p$ (p_T is the radial component) < 0.9, and all these forms were used for expressing the cut;

4. The cut on momentum window 103.5 MeV/c $< p <$ 104.7 MeV/c. The window cuts off a significant portion of the tail, cutting $\sim 40\%$ of the events in order to minimize the background contamination.

The reconstructed momentum resolution with this set of cuts is shown in figure 2.15

Using this set of cuts, the different backgrounds were estimated using Mu2e framework. Table 2.1 summarizes the simulation results:
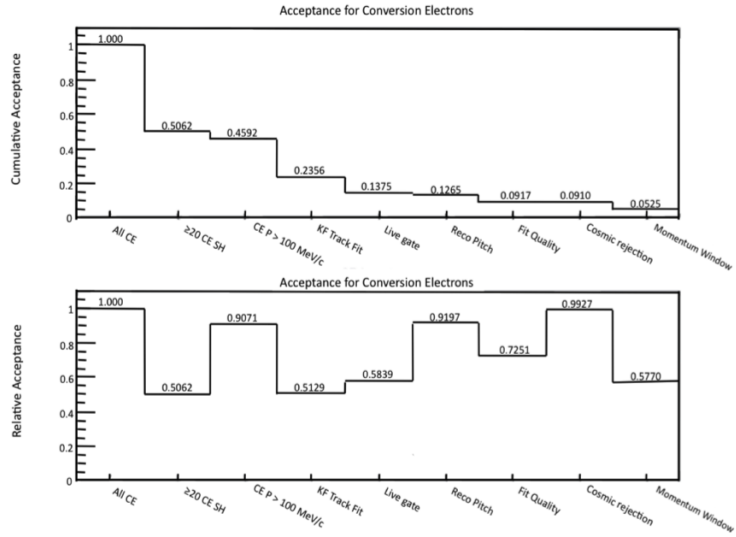
Figure 2.14: Cuts used in the simulation, applied in order (top panel) and stepwise (reduction from previous step.).
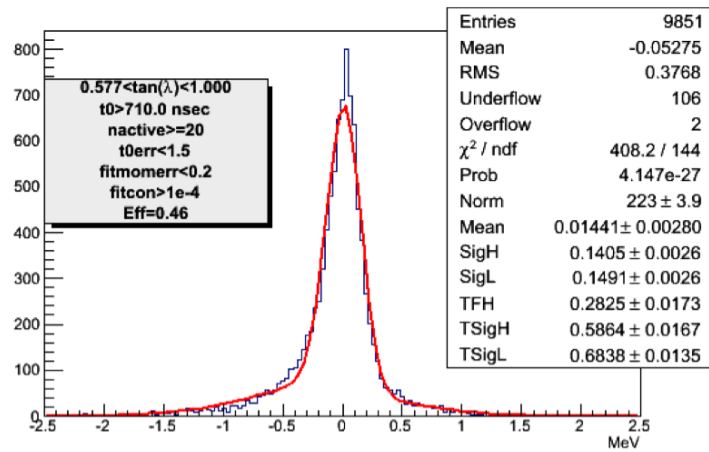

Figure 2.15: Reconstructed track momentum resolution with cuts used in the text. A double-sided Gaussian was fit to indicate the size and width of the tails.

27

Background	Background estimate	Error estimate	Justification
Muon decay-in-orbit	0.22	± 0.06	Acceptance and energy loss modeling, spectrum calculation, reconstructionalgorithm
Cosmic Rays	0.05	± 0.013	Statistics of sample
Radiative Pion Capture	0.03	± 0.007	Acceptance and energy loss modeling
Pion decay-in-flight	0.003	± 0.0015	Cross-section, acceptance and modeling
Muon decay-in-flight	0.01	± 0.003	Cross-section, acceptance and modeling
Antiproton	0.10	± 0.04	Cross-section, acceptance and modeling
Beam electrons	0.0006	± 0.0003	Cross-section and acceptance (this is an upper limit)
Radiative muon capture	$< 2 \times 10^{-6}$	-	Calculation
Total	**0.42**	**± 0.08**	**Add in quadrature**

Table 2.1: Summary of background estimates and errors.

Chapter 3

Crystal Calorimeter for Mu2e

3.1 Introduction

The Mu2e detector contains components that operate in the evacuated warm bore of the Detector Solenoid as well as components outside of the Detector Solenoid. It must accurately and redundantly measure the energy of 105 MeV electrons that signal muon conversions in aluminum while eliminating backgrounds. This requires good momentum resolution and particle ID in the presence of high rates. High rates of hits in the tracker may cause pattern recognition errors that add tails to the resolution function and result in background. Accidental hits can combine with or obscure hits from lower energy particles to leave behind a set of hits that might reconstruct a trajectory consistent with a higher energy conversion electron. Extrapolating the reconstructed trajectory to the downstream calorimeter and comparing the calculated intercept with the measured position in the calorimeter may help to identify backgrounds. The calorimeter may also be used in hardware, software or firmware triggers.

3.2 Requirements

The primary functions of the calorimeter are to provide energy, position and timing information to validate the events reconstructed by the tracker. The calorimeter also required to provide a potential trigger for this experiment. This leads the following requirements:

1. An energy resolution of $\sigma_E = 2\%$ (FWHM / 2.35, since the response is non - Gaussian) or better at 100 MeV to confirm the precise energy measurement from the tracker. The uncertainty in the energy scale should be small compared to the resolution;

2. A $\sigma_{r,z} \sim$ resolution of ~ 1 cm or better for the position of the electromagnetic apex to allow comparison with the extrapolated trajectory from the tracker;

3. Additional information to be combined with information from the tracker, so to distinguish muons or pions form conversion electrons with 99% C.L.;

4. A timing resolution of ~1 ns to ensure that energy deposits in the calorimeter are in time with events reconstructed in the tracker, enabling rejection of backgrounds;

5. Provision for a trigger, either in hardware, software, or firmware that can be used to identify events with significant energy deposits;

6. Capability to operate in the unique, high-rate Mu2e environment and radiation hardness for exposures up to 50 Gy/year/cm^2;

7. Temperature and Gain stability such that the calorimeter response and its readout do not vary by more than ±0.5%, not to deteriorate the required energy resolution.

The energy resolution of a crystal calorimeter complements, but is not competitive with, that of the tracking detector. However even a coarse confirmation of track energy will help to reject backgrounds. The error due to the extrapolation of a track from the tracker to the calorimeter was estimated by means of Monte Carlo studies and is shown in figure (3.1). There is no need for the calorimeter position resolution to be better than the extrapolation error, driven by multiple scattering in the tracker. Based on this study, a position resolution of 1 cm is sufficient.
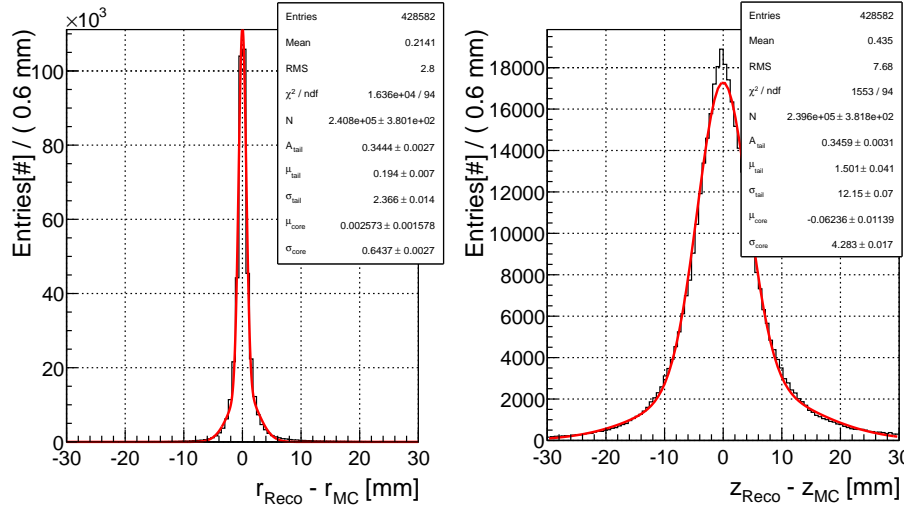

Figure 3.1: The error on the extrapolated position of tracks from the tracker to the calorimeter. The tracks were fitted with a Kalman filter and extrapolated to the calorimeter using the full covariance matrix. The z direction is along the solenoid axis and the r direction is transverse to the solenoid axis.

The signals from the tracker and from the calorimeter are correlated in time. The time resolution of the calorimeter should be comparable to the time resolution of extrapolated tracks from the tracker, estimated to be a few ns [23]. A calorimeter timing resolution of about 1 ns is consistent with the tracker and can easily be achieved.

3.3 Calorimeter Design

The design selected for the Mu2e calorimeter uses an array of LYSO crystals arranged in four vanes of 11×44 crystals that are approximately 1.3 m long. Electrons following helical orbits spiral into the side faces of the crystals, colored red in figure (3.2). Photodetectors, electronics and services are all arranged on the opposite face. The 4-vane geometry has been optimized (see chapter (4)) for the best acceptance at a given crystal volume. Each vane is composed of a matrix of LYSO crystals. The crystal dimensions are $3 \times 3 \times 11$ cm^3; there are a total of 1936 crystals. Each crystal is read out by two large area Avalanche Photo Diodes (APD). Solid-state photo-detectors are required because the calorimeter resides in the 1 T magnetic field of the Detector Solenoid. Front end electronics reside on the detector and digitizers for each channel are placed inside the DS. A flasher system provides light to each crystal for relative calibration and monitoring purposes. A liquid source system (inspired to the one used in the *BaBar* experiment [24]) provides absolute calibration and an energy scale. The crystals are supported by a lightweight carbon fiber support structure. Each of these components is discussed in the sections that follow. An alternative disk based configuration, where lead tungstate crystals (PbWO$_4$)are used, was also taken under consideration because this geometry allows improvements in acceptance (see appendix (A)).
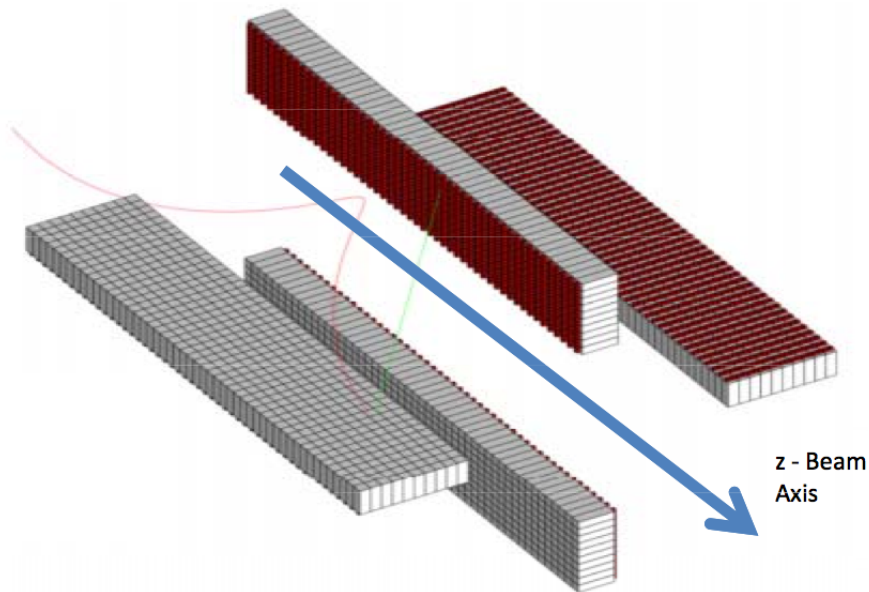

Figure 3.2: The Mu2e calorimeter, consisting of an array of LYSO crystals arranged in 4 vanes. Electrons spiral into the red faces.

3.4   Crystal Choice

In the 100 MeV energy regime, a total absorption calorimeter employing a homogeneous continuous medium is required to meet the resolution requirement. Two types of crystals have been considered for the Mu2e calorimeter: lutetium-yttrium oxyorthosilicate (LYSO) and a new version of lead tungstate ($PbWO_4$), called PWO-2.

3.4.1   Crystals

The basic calorimeter element is a lutetium-yttrium oxyorthosilicate (LYSO) crystal. LYSO is an excellent match to the problem at hand: it has a very high light output, a small Moliére radius (R_M), a fast scintillation decay time, excellent radiation hardness, and a scintillation spectrum that is well-matched to readout by large area APD's. The properties of LYSO are summarized and compared to those of lead tungstate in Table 3.1. In the vane geometry of Mu2e electrons hitting the upstream face of a calorimeter will be poorly measured: so to maximize the acceptance of the calorimeter a high premium is placed on dense crystals with a short radiation length. Short radiation length and fast emission time of LYSO are well matched to the Mu2e environment.

LYSO and $PbWO_4$ share certain desirable characteristics: they have fast scintillation decay times, have similar Moliére radii (R_M), are not hygroscopic, and have reasonable mechanical properties. There are differences, however: LYSO has a slightly lower density and a slightly longer radiation length, but has a much higher light yield. The light yield of LYSO is a factor of 200 better than the PWO-2 variant of $PbWO_4$ at room temperature. It is more radiation hard, and the scintillation light output is not rate- dependent, as it is for $PbWO_4$. The greatest advantage of LYSO crystals is the

Crystal	LYSO	PbWO$_4$
Density (g/cm^3)	7.28	8.28
Radiation length (cm) X_0	1.14	0.9
Moliére radius (cm) R_M	2.07	2.0
Interaction length (cm)	20.9	20.7
dE/dx (MeV/cm)	10.0	13.0
Refractive Index at λ max	1.82	2.20
Peak luminescence (nm)	402	420
Decay time τ (ns)	40	30.10
Light yield (compared to NaI(Tl)) (%)	85	0.3, 0.1
Light yield variation with temperature (% / °C)	-0.2	-2.5
Hygroscopicity	None	None

Table 3.1: Crystals parameters for LYSO and PbWO$_4$

excellent light yield that allows the achievement of excellent energy resolution without any thermal stabilization. $PbWO_4$ needs to operate at -25° to reach an almost comparable energy resolution. The much larger LYSO signals provide greater flexibility in the choice of photosensors and front end electronics (FEE). Furthermore LYSO is well radiation hard, as measured both with γ's and with neutrons. Negligible deterioration

of signals (10% loss in light yield) is observed with γ exposures of 10,000 Gy (i.e. 15 years of Mu2e running). A factor of 5 smaller induced absorption than PWO_2 is seen after irradiation with a flux of 1013 n/cm^2. Therefore, for LYSO no stimulated recovery mechanism is required. The main disadvantage of LYSO is the cost. LYSO crystals are commercially available from Saint-Gobain, SICCAS (Shanghai Institute of Ceramics), SIPAT (Sichuan Institute of Piezoelectric and Acousto-optic Technology) and Zecotek. Chinese producers result to able able to provide good quality material at reduced cost. Both SIPAT and SICCAS can produce $\sim$ 2000 crystals in a time span of 1 - 1.5 years. The LYSO crystal cost is a factor $\sim$ 2 larger than PWO_2. There are, however, compensating cost reductions. It is not necessary to cool the crystals to -25°C, no provision for radiation damage recovery need to be provided, and the performance and running efficiency of the experiment will be improved.

3.4.2 Photosensor

The presence of a 1 T magnetic field in the detector region precludes the use of conventional photomultipliers. Since PIN diodes show a large response to traversing charged particles ("nuclear counter effect"), their use has been excluded: only large area avalanche photo diodes (APD's), and the newest type of Silicon Photomultipliers (SIPMs) have been considered. At the moment large area SIPMs are still in the development phase and, for this reason, they are considered only as an alternative to APD's.

Large area APD's, with an active area of 5×5 mm^2 (Hamamatsu S8664-55) are used in large quantity by CMS at LHC. APD's are reverse-biased diodes with an internal electric field used for avalanche multiplication of charge carriers. As a standard a reverse type APD is composed of three parts, as shown in figure 3.3:

1. A conversion layer ($\sim 2\mu m$ thick) where the electron-hole pairs are generated;

2. A high electric field region ($\sim 6\mu m$), where the amplification of carriers occurs;

3. A drift-region of $\sim 200\mu m$ where the carriers drift towards the collection electrode.

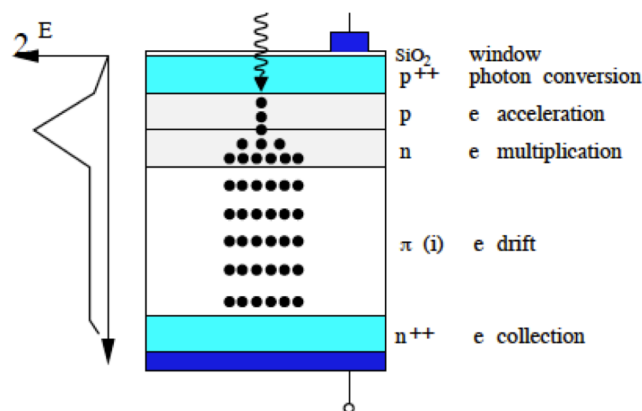Figure 3.3: Scheme of the structure of a Hamamatsu APD.

Larger area APD's, developed by Hamamatsu are now available in different sizes (10 × 10 mm^2 and 7 × 15 mm^2) both in standard and low capacitance versions. Other producers are able to provide similar size devices, such as Radiation Monitoring Devices (RMD) in the US, which offers 8 × 8 mm^2 and 13 × 13 mm^2 (S0814 and S1315) devices.

At the present two photosensor are the candidates for Mu2e: the RMD S1315 and the Hamamatsu S8664-55-1010. The relatively low gain of these APD's requires the use of a front-end amplification stage. Table 3.2 lists the properties of these devices. The large area of these devices ensures high light collection efficiency from the 30 × 30 mm^2 area of the crystal: 19% for the S1315, 11% for the S8664-1010. The quantum efficiency of the two candidate APD's is shown in figure 3.4 as a function of wavelength: both candidates have an high quantum efficiency that is well-matched to the emission spectra of the LYSO crystal (402 nm). They are also fast and radiation resistant. However their gain and dark current have a strong temperature dependence. Measurements done by CMS [25] and PANDA [26] indicate a gain dependence of ~ 2% / °C. Good temperature and voltage stability are therefore required. Temperature stability of ± 0.2°C and voltage stability of ± 20 mV are necesary to achieve a 0.4 % gain stability: this is not difficult to achieve in practice. Two other relevant parameters that drive the APD choice are the excess noise factor (F) and the nuclear counter effect (NCE).
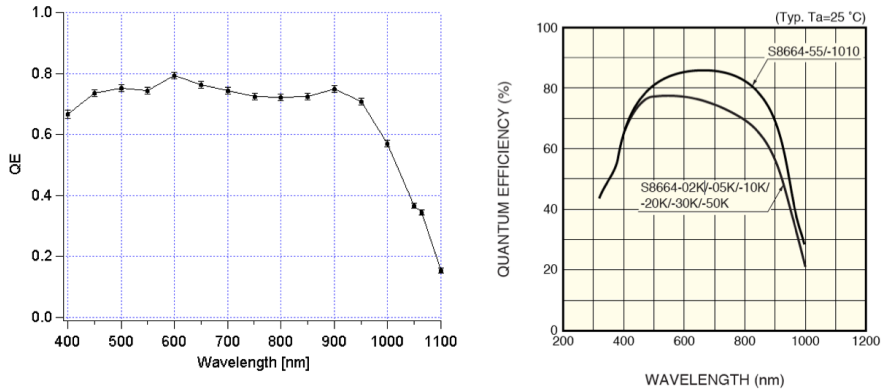

Figure 3.4: Quantum efficiency as a function of wavelength for Radiation Monitoring Devices S1315 (left) and for the Hamamatsu S8664-1010 (right).

For a light yield L of (N$_{pe}$) / MeV, at the APD conversion layer, the total signal for a shower of energy E(MeV) is $Q = MEL$ (where M is the gain) and the standard deviation σ of the peak in the pulse height spectrum is then $\sigma = M \sqrt{EL}$. The resulting resolution is

$$\frac{\sigma}{E} = \frac{\sqrt{F}}{\sqrt{EL}} \tag{3.1}$$

due to the combination of the photoelectron statistics and fluctuations in the amplification process. The F factor is relevant for the achievable energy and depends on both the device and on the applied voltage.

The NCE is the charge produced by a photosensor when a charged particle directly hits its surface. When this happens, owing to shower leakage or external accidental back-

34

Properties	S8664-55	S8664-1010	S1315 (RMD)
Active area (mm^2)	5×5	10×10	13×13
QE ($\sim$ 405 nm)	0.65	0.65	0.65
I_d (nA)	5	10	Not measured
Capacitance C$_d$ (pF)	80	270	120
Gain	50 @ 350 V	50 @ 350 V	100 @ 1700 V
Excess noise F	2.0 @ gain = 50	1.38 @ gain = 50	Not measured

Table 3.2: Properties of the RMD S1315 and the Hamamatsu S8664 APD's.

ground, the photosensor generate unwanted charges that deteriorate the energy resolution. In the APD, only carriers produced before the amplification layer experience full amplification; carriers produced in the avalanche region are amplified according to their location at creation. A quantitative NCE measurement is given by d_{eff} (the effective thickness of the Si amplification layer). This is obtained by exposing the APD to a ^{90}Sr source and by comparing the measured charge with the one from a PIN diode of known thickness d$_{PIN}$. The NCE is reduced by using APD's with a smaller d_{eff} and by increasing the crystal light yield. The normal capacitance of the S8664-1010 APD [26] shows a reasonably small NCE. To minimize the Nuclear Counter Effect, each crystal will be read by two APD's, so improving the overall number of photoelectrons/MeV and consequently the reliability of the calorimeter.

Chapter 4

Simulation and test of Crystal calorimetry

4.1 Introduction

To evaluate the calorimeter energy and position resolution, a simulation of the experimental events is performed using the GEANT-4 [17]package. For each particle, the LYSO calorimeter response is simulated A crystal with some deposited energy is defined as a hit cell. For each hit also the information about the vane number, the spatial position in the vane and the time associated to the shower are recorded; if more than one particle contributes to the energy deposited in a cell, all hits in a 100 ns time interval are summed.

For all the studies reported in this chapter, the coordinates are defined with resect to a local "vane" frame. This frame is identified by three orthogonal axis (u, v, w), where w represents the direction along the beam line, v the radial direction and u the direction normal to the vane (outgoing). Crystal position in a vane is also identified by the row and the column indexes: a crystal row is defined as the group of crystals aligned on the v direction, a column on the w direction. The indexes are ordered such that the first row is the closer to the beam line; the first column is the one closer to the Tracker.

Figure (4.1) shows a drawing of the adopted local frame.

A group of topologically connected hits, i.e. contiguous, fired crystals around the cell with maximum energy deposition, defines a cluster. Once the cluster is identified, the energy sum and the arrival time of the incident particle are evaluated. The arrival time, is calculated by means an energy weighted average of the time connected to the hits. Excluding cells already used for the first cluster, other clusters are searched following the same procedure. To reject energy coming from the environmental background, timing is used to distinguish overlapping particles.

Many experimental and technical details have been added to make the simulation more realistic, especially for the energy response and resolution. The presence of a large
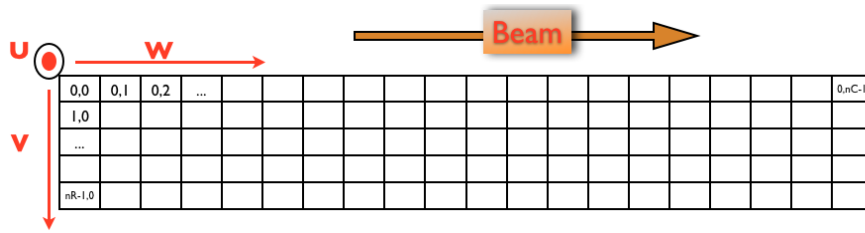
Figure 4.1: $\vec{u}$, $\vec{v}$ and $\vec{w}$ represent the three orthogonal axes which define the local vane frame. The $\vec{w}$ axis is along the beam line, $\vec{v}$ is on the radial direction and $\vec{u}$ is along the direction orthogonal to $\vec{v}$ and $\vec{w}$ on the opposite side of the avalanche photodiodes (APD's). By convention u = 0 is set in the front face of the crystal (opposite side of the APD's, where the electrons impact), w= 0 in the lateral edge of the calorimeter closest to the tracker and v = 0 at the bottom edge close to the beam line.

environmental background can degrade the calorimeter response. These backgrounds have a non uniform distribution.

A fiducial volume was identified so to prevent contamination of the reconstructed clusters by these backgrounds [27]. A reconstructed cluster is considered to belong to the fiducial volume if its most energetic crystal is not contained either in the first column (closer to the Tracker) and in the first row (closer to the beam line).

4.2   Geometrical optimizations

The calorimeter is required to have an acceptance as high as possible for signal events, while maintaining an adequate background rejection. In the Mu2e design, the four vanes surround the beam line, but at a distance sufficient to avoid the main bulk of the remnant muon beam and the background from decay-in-orbit/decay-in-flight electrons. A first estimate of the inner and the outer radii can be derived by simple kinematical considerations: the stopping target radii range between 6 - 10 cm and the maximum acceptance is observed for a pitch angle of about 60°. For an electron at $p \approx 60$ MeV (which is the typical energy of the DIO electron reaching the calorimeter), the helix radius is:

$$
\begin{aligned}
r_{inner} &\approx \frac{p\,sin(60°)}{0.3qB} + \text{radius of the stopping target} \\
&\approx 29.7 + 8 \\
&\approx 38\text{cm}
\end{aligned}
\tag{4.1}
$$

A crude estimate of the outer radius (r_{outer}) can also be made. The diameter of the helix for a conversion electron (≈ 103 MeV when impacting the calorimeter, see figure (4.12)) with 60°pitch is ≈ 60 cm; by adding 10 cm for the stopping target the outer radius results to be ≈ 70 cm, corresponding to a number of rows variable between 10 to 12.

The calorimeter acceptance was optimized by modifying the inner radius in the range 36 cm$\leq r_{inner} \leq 39$ cm and the number of rows between 10, 11 or 12.

The optimal geometrical configuration has been checked by maximizing the ratio ϵ:

$$\epsilon = \frac{N^{reco}_{cluster}}{N^{cuts}_{e^-}} \tag{4.2}$$

where $N^{reco}_{cluster}$ represents the number of reconstructed clusters with energy greater than $E_{cluster}$ from conversion electrons (N_{e^-}) passing the quality cuts of the tracker [28]. The statistical error of ϵ is derived from the equation (4.2), assuming $N^{reco}_{cluster}$ and $\left(N_{e^-} - N^{reco}_{cluster}\right)$ as Poissonian distributed:

$$\delta\epsilon = \sqrt{\frac{\epsilon(1 - \epsilon)}{N_{e^-}}} \tag{4.3}$$

The configuration finally chosen is a crystal matrix with 11 rows and 44 columns and $r_{inner} = 360$ mm. This choice represents the best compromise between cost savings and best efficiency. figure (4.2) shows ϵ as a function of $E_{cluster}$ for the chosen configuration.
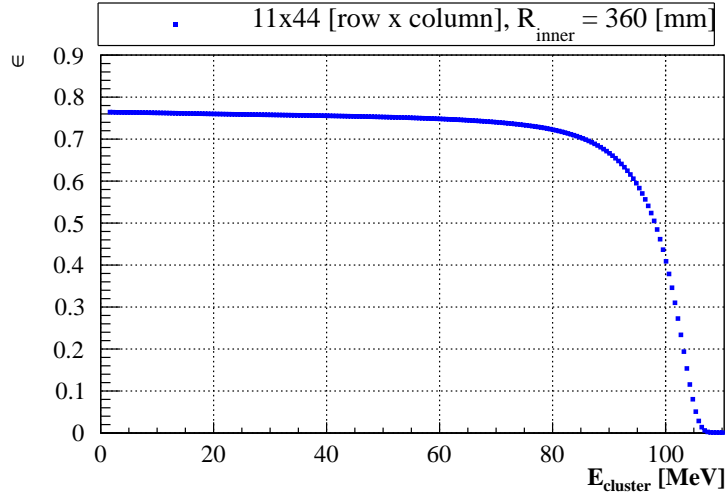
Figure 4.2: Distribution of ϵ as a function of $E_{cluster}$ for the configuration 11X44 and inner radius of 36 cm.

The cluster mapping was also studied starting from the distribution of the impact point of the seed particles. figures (4.3) and (4.4) show respectively the distribution with all rows and columns and the distribution obtained excluding either the first row and the first column (fiducial cuts).
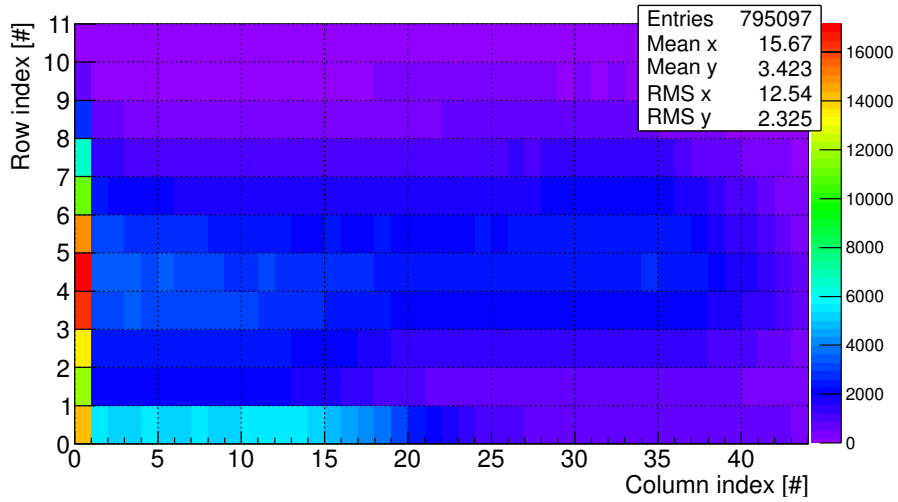
Figure 4.3: The plot shows the spatial distribution of the seed particles along the vane. The row and column indexes are used to identify the coordinates of the impact point.
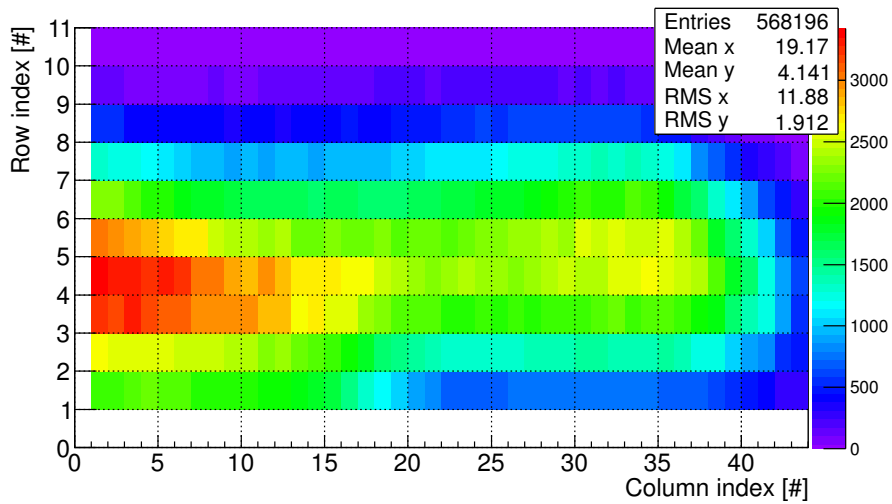
Figure 4.4: The plot shows the spatial distribution of the cluster seed particles along the vane without considering the the first row and the first column. The row and column indexes are used to identify the coordinates of the impact point.

From the comparison of figures (4.3) and (4.4) fiducial cuts result to reduce the number of the reconstructed clusters of $\sim 28\%$.

4.3 Energy resolution

As usual, also in the case of a LYSO calorimeter, the energy resolution can be parameterized by three terms added in quadrature:

$$\frac{\sigma}{E} = \frac{a}{\sqrt{E/GeV}} \oplus \frac{b}{E/GeV} \oplus c \qquad (4.4)$$

The first term is the stochastic term due to fluctuations in the signal. In a LYSO crystal light yield is large ($\approx$2000 p.h./MeV), and the a term is negligible. In crystals when "a" is very small, the first term is empirically parametrized as $a/E^{1/4}$, to account for more intrinsic signal fluctuations resulting from light self-absorption, geometrical uniformity and non-linearity in the response.

The second term, b, is due to the electronic noise and its contribution drops linearly for increasing energy. Recent experimental results [29] has shown that the noise is not a limiting factor to the energy resolution of a LYSO calorimeter for energies around 100 MeV.

The third term, c, is due to leakage or calibration errors and it is considered the ultimate resolution. This is the only relevant term at very high energies.

To understand the relevance of these three contributions, in Mu2e calorimeter many procedures were implemented trying to introduce all the experimental effects.

4.3.1 GEANT-4 Energy resolution response

Using GEANT-4 [17] the energy resolution is evaluated taking into account 1) the fluctuations of the stochastic processes describing the shower development in the crystals, 2) the effects due to eventual additional materials, such as wrapping and supports, and shower leakage. Energy resolution for a monochromatic electron beam with energy E = 104.97 MeV (conversion energy) is shown in figure (4.5). Such an asymmetric distribution can be fit by means of a logarithmic Gaussian shape [30] as follows:

$$f(E) = \frac{N \cdot \eta}{\sigma_E s_0 \sqrt{2\pi}} \exp\left[\frac{-1}{2s_0{}^2} \log^2\left[1 - \frac{\eta}{\sigma_E}\left(E - E_{peak}\right)\right] - \frac{s_0}{2}\right] \qquad (4.5)$$

where E_{peak} is the energy corresponding to the peak, σ_E = FWHM / 2.35, η is the asymmetric parameter and s_0 is

$$s_0 = \frac{2}{\xi} \sinh^{-1}\left(\frac{\eta\xi}{2}\right), \quad \xi = 2.35$$

The fit to figure (4.5) shows that the value of the energy resolution is $\approx$ 1.5%

4.3.2 Longitudinal response uniformity

The origin of the longitudinal non-uniformity (LRU) can be attributed to the LYSO chemical nature; light output depends both by the cerium concentration and by the
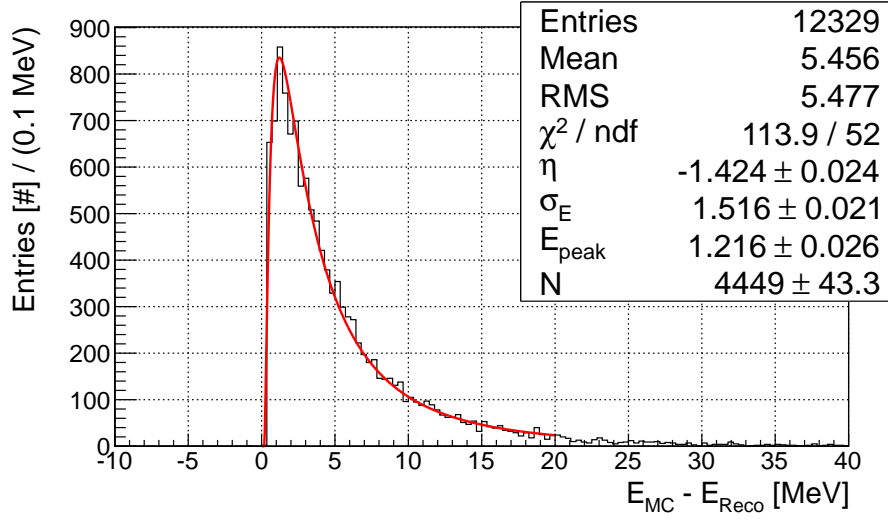
Figure 4.5: Distribution of the difference between the energy of the conversion electrons (E_{MC} = 104.973 MeV) and the one deposited inside by the calorimeter. Only clusters reconstructed in the fiducial volume are taken into account.

yttrium fraction, so any longitudinal variation of the cerium concentration or of the yttrium fraction would affect light response uniformity. There is also a contribution of the light collection efficiency that can have a linear dependence along the crystal length. Experimentally, the light output variation as a function of the distance of the particle from the readout device is parametrized as:

$$\frac{LO}{LO_{mid}} = 1 + \delta \left(x/x_{mid} - 1 \right) \tag{4.6}$$

where LO is the light output, LO_{mid} represents the light output when the energy is deposited in the middle of the crystal, δ represents the deviation from the response uniformity, x is the distance of the energy deposition from the readout device and x_{mid} is the crystal half lenght.

Experimental measurements [31, 32] on LYSO crystals (25mm×25mm×20cm) indicate that an uniformity δ better than 5% is achievable with a special treatment [32].

The non-uniformity effect was included in the simulations using eq.(4.6) with a value of δ which is extracted, for each crystal, from a Gaussian distribution of mean 0.05 and sigma 0.01 [31].

The resulting distribution of the residuals between the conversion electron energy (E_{MC}) and the deposited energy is showed in figure (4.6). The LRU has two consequences: the resolution is worst and a significant increase in the mean energy loss ($\approx$ 1.2 MeV) is generated.
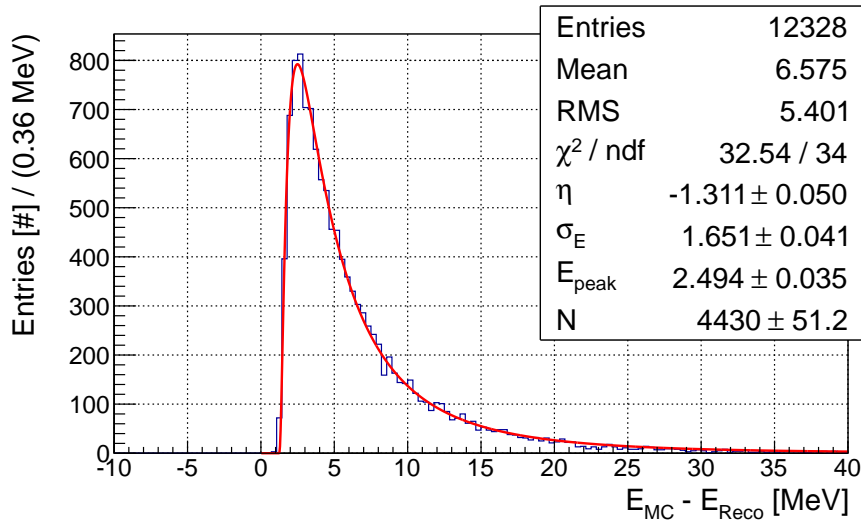
Figure 4.6: Distribution of the difference between the conversion electron energy (E_{MC} = 104.973 MeV) and the one reconstructed by the calorimeter; this plot belongs only to the clusters in the fiducial volume. The physical effect included is the non-uniformity.

4.3.3 Non-linearity

The last physical effect, that was included, is the non-linearity in response. The luminous efficiency (i.e. the number of scintillation photons per unit energy deposit) depends on the energy of the particle that excites it [33]. When the primary electron traverses the scintillator, it loses energy inside the scintillator and produces other relatively high-energy electrons (delta rays), which can also excite the scintillator. Thus, the scintillator is effectively excited by a number of electrons with different energies. Bcause the luminous efficiency depends on electron energy, the number of scintillation photons will not necessarily be the same, and these variations affect energy resolution; this phenomenon is usually called "non-linearity" or "non-proportionality".
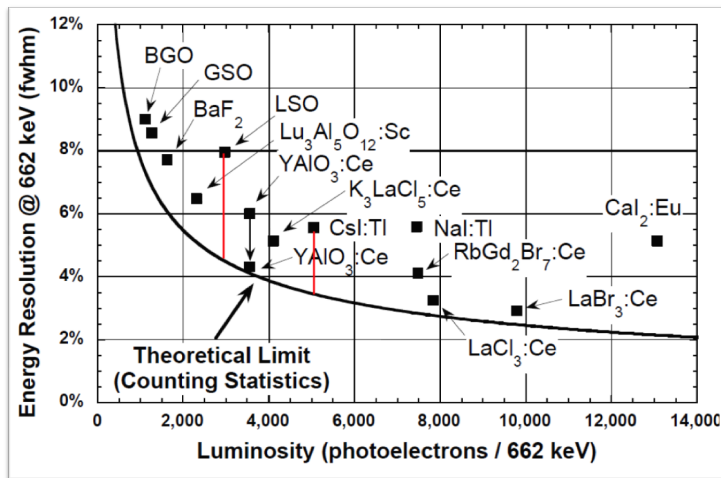
Figure 4.7: Measured energy resolution of several scintillators for 662 keV gamma rays as a function of their light output (expressed as the number of photoelectrons observed with a photomultiplier tube). The solid curve indicates the theoretical lower limit placed by counting statistics.

Figure 4.7 shows how relevant is this effect in low energy spectroscopy: with very few exceptions, all the points lie considerably above the solid curve representing the theoretical lower limit due to counting statistics. The energy resolution of most scintillators is worse than the one predicted by counting statistic.

To include this effect a parametrization between the electron (or photon) energy and the relative light yield [34] was introduced in calorimeter simulation (see figure (4.8)). In the simulation, the corresponding corrections were applied to electrons (or photons)
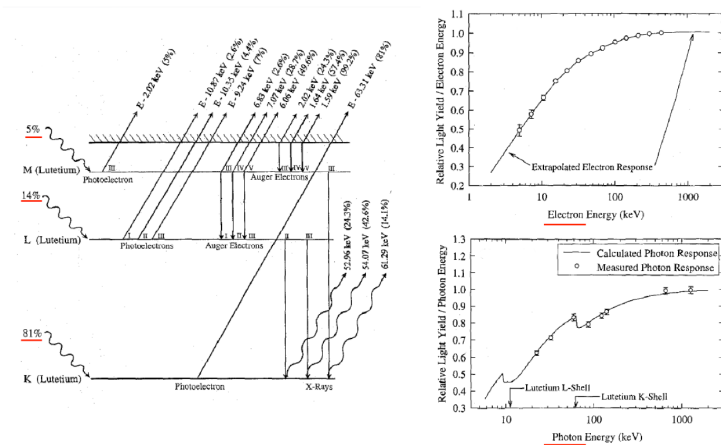
Figure 4.8: Plot of the electron kinetic (and photon) energy versus the normalized light yield [34].

with kinetic energy below 1 MeV. Figure 4.9 shows the resulting energy resolution: the effect gives a negligible contribute to the global resolution (an increase of about $\approx 2\%$
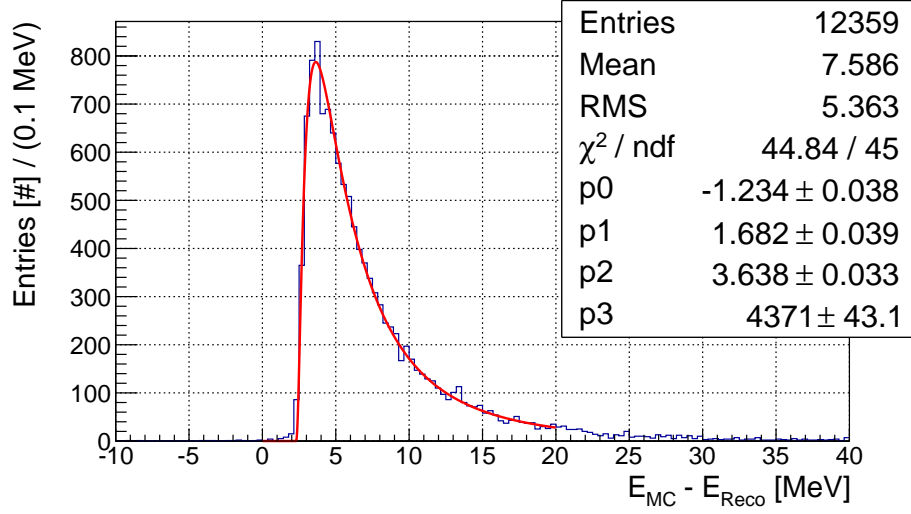
Figure 4.9: Distribution of the difference between the effective energy of the conversion electrons (E_{MC}) and the one reconstructed by the calorimeter; this plot belongs only to the clusters in the fiducial volume. The physical effects included are: non-uniformity and non-linearity.

with respect to figure (4.5)) and increase the mean energy loss of ≈ 1.14 MeV.

4.3.4 Fluctuations in charge production

Starting from most recent experimental results [35], a procedure that reproduces the Poissonian fluctuations associated to the charge production was implemented in the simulation.

Eq.(4.7), shows all the sources of this fluctuation:

$$LO = LY_{intr} \times \epsilon_{lightcoll} \times QE \times G \qquad (4.7)$$

- The intrinsic light yield of the crystal (LY_{intr}) depends on the cesium and yttrium concentrations (for LYSO is ≈ 25000 p.h. / MeV [31]), which changes crystal to crystal;

- The light collection efficiency ($\epsilon_{lightcoll}$) depends on a large number of parameters: the wrapping material, the geometry of the crystal, the temperature, the coverage area of the readout device and how the readout is connected to the crystal. For these reasons its parametrization is difficult;

- The quantum efficiency (QE) depends on the applied voltage, the wavelength of the collected light and on the device temperature;

- The device gain (G) depends on the condition in which the device operates: it depends mostly on temperature and applied voltage.

The *LO* value used inside the simulation is extracted from experimental results [35]. In [35] *LO* was evaluated to be (1380 ± 186) p.e. / MeV and was obtained using LYSO

samples from Crystal Photonics, Inc. (CPI) (25 mm × 25 mm × 20 cm) coupled to two Hamamatsu S8664-55 APD's with total readout area 0.5 cm^2 , corresponding to 8% coverage of the crystal readout face. The Quantum efficiency was 75% in the region of the LYSO wavelength peak and the gain was about 50 at the operating voltage (350 V). Scaling these values to the Mu2e crystal dimensions (3 cm × 3 cm × 11 cm) and APD's characteristics, the resulting Light Output (*LO*) is (3319 ± 448) p.e / MeV. To be conservative half of this value was used in simulations.

The adopted smearing process is the following:

1. first the energy collected by each crystal is converted in number of photo-electrons N_e, using as conversion factor LO a value extracted from a Gaussian distribution of mean 1660 p.e. / MeV and sigma of 224 p.e. / MeV. N_e is also scaled by 1.3 the expected APD Fano-factor (*F*),

2. then a number $\bar{N}_e$ is extracted from the Poissonian distribution of mean N_e,

3. at the end $\bar{N}_e$ is reconverted to an energy value using LO and .

Figure 4.10 shows the resulting distribution of the energy residuals: The comparison
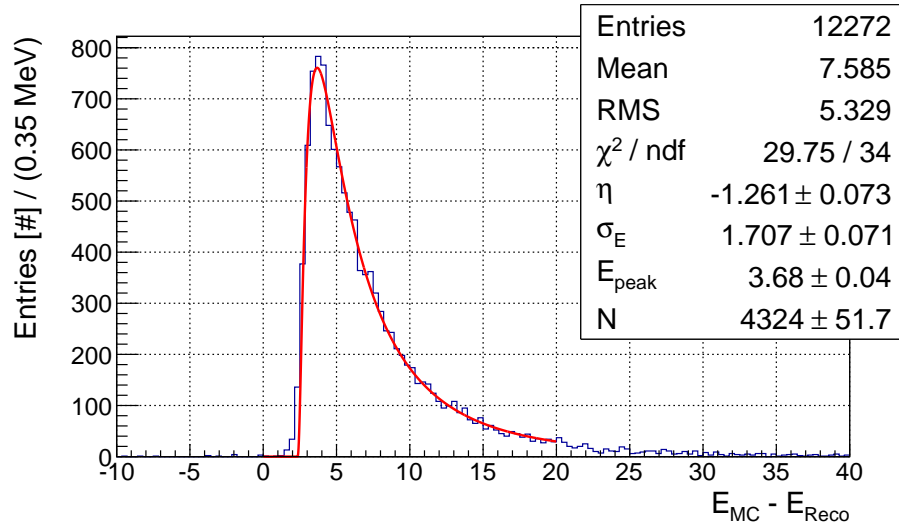
Figure 4.10: Distribution of the difference between the conversion electron energy (E_{MC} = 104.973 MeV) and the one collected by the calorimeter readouts; this plot belongs only to the clusters in the fiducial volume. The physical effects included are: LRU, non-linearity and charge production fluctuations.

figures (4.9) and figure (4.10) shows that charge production fluctuation, degrades resolution, from 1.682 to 1.707 MeV.

A consistency-check can be done by comparing σ_E with the square sum of the deviation standard resulting from figure (4.9) ($\bar{\sigma}_E$)and the one associated to the Poissonian

fluctuation (σ_{Pois}) used to derive the distribution in figure (4.10):

$$\begin{aligned}
\sigma_{Pois} &= F/LO \sqrt{E_{MC} \cdot LO/F} \\
\sigma_{Pois} &\approx 0.28 \text{ MeV} \\
\sigma_{EC} &= \sigma_{Pois} \oplus \bar{\sigma}_E \\
\sigma_{EC} &\approx 1.70 \text{ MeV}
\end{aligned} \qquad (4.8)$$

As expected σ_{EC} and σ_E (from figure (4.10)) are in agreement.

4.3.5 Electronic noise

Tests with a small prototype of the calorimeter front end electronic [29] show that the amplitude of the electronic noise fluctuation is ≈ 30 keV / channel. To simulate its contribution to the energy resolution a noise term is added to all the calorimeter APD's by extracting for each channel a noise term from a Gaussian distribution of mean 0 keV and sigma 30 keV [29].

To take into account this noise the clustering algorithm was also changed; adding a threshold on the energy of each crystal at 30 keV. The fit in figure 4.11 shows a
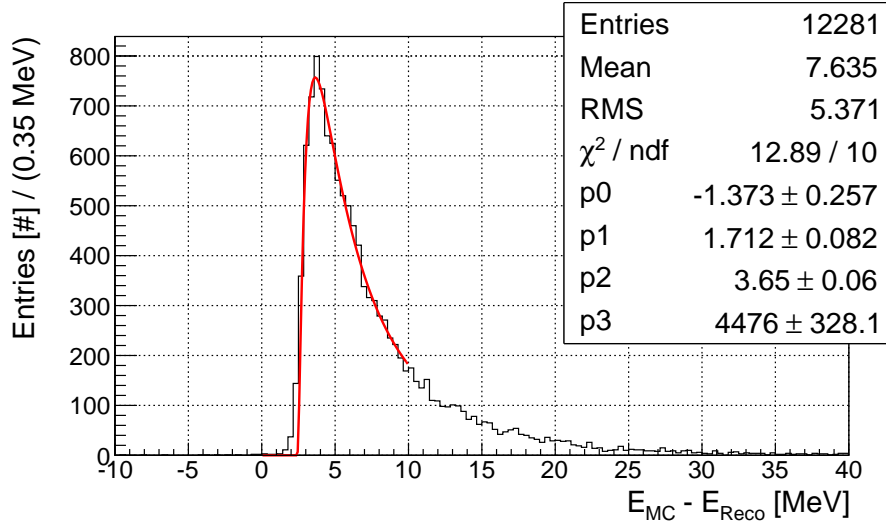
Figure 4.11: Distribution of the difference between the true energy of the conversion electrons (E_{MC}) and the one deposited in the calorimeter; this plot belongs only to the clusters in the fiducial volume. The physical effects included are: photo-statistic fluctuations and electric noise.

$\sigma_E = 1.712 \pm 0.082$ MeV and $E_{peak} = 3.65 \pm 0.06$ MeV.

4.3.6 Energy loss in passive materials

In the Mu2e experiment, the conversion electron traverses some materials (mainly Al targets, proton absorber and straw tubes) before reaching the calorimeter, so degrading the conversion spectrum. In figure 4.12 the resulting electron energy spectrum is reported. A fit to this spectrum shows a shift of the energy peak to 103.28 ± 0.01 MeV and a FWHM of the distribution 1.287 ± 0.012 MeV. Figure (4.13) shows the convolu-
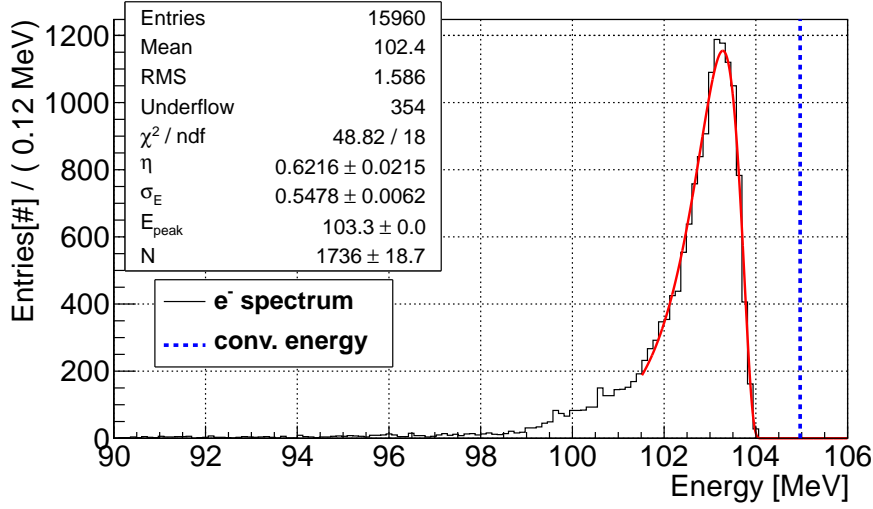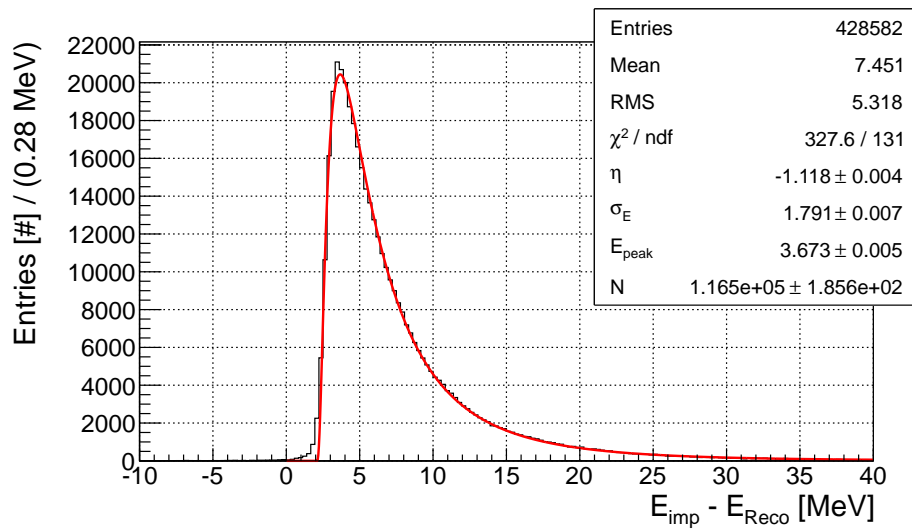

Figure 4.12: Distribution of the conversion electrum spectrum (black line); the red curve is the fit on the log normal Gaussian function (eq.(4.5) of the electron spectrum. The blue dashed line represents the conversion electron energy.

tion between figure (4.11) and figure (4.12), so describing all the effects degrading the energy resolution.

The resolution σ_E in figure (4.13) is 1.791 ± 0.007 MeV. The values of E$_{peak}$ in figure (4.13) for mono-energetic electrons (figures (4.11)) are compatible. Calculating the squared sum of the σ_E values of the two distributions in figures (4.11) and (4.12)) it is possible to derivethe expected value of σ_E for their convolution:

$$\begin{aligned} \sigma_E^2 &= \sigma_{4.11}^2 + \sigma_{4.12}^2 \\ &= \sqrt{1.712^2 + 0.547^2} \\ &\approx 1.797 \text{ MeV} \end{aligned}$$

where σ_{imp} is the sigma value from the fit of the energy distribution of the conversion electron (see figure (4.12)) and $\bar{\sigma}_E$ is referred to the previous case where a monochromatic electron (of energy $E_{MC} = 104.973$ MeV) reach the calorimeter (see figure (4.11)).

As expected, the small spread of the conversion electron spectrum is not a limiting factor for the calorimeter energy resolution.

Figure 4.13: Distribution of the difference between the true energy of the conversion electrons (E_{imp}) and the one reconstructed by the calorimeter; this plot belongs only to the clusters in the fiducial volume.

4.3.7 Crystal length optimization

The calorimeter resolution was also studied as a function of the crystal length. This has been done to improve the cost saving by taking into consideration that, since the conversion electrons impinge at a grazing angle of 45°, a long crystal is not necessarily needed to contain the shower. Figure (4.14) shows the energy resolution as a function of the crystal length.
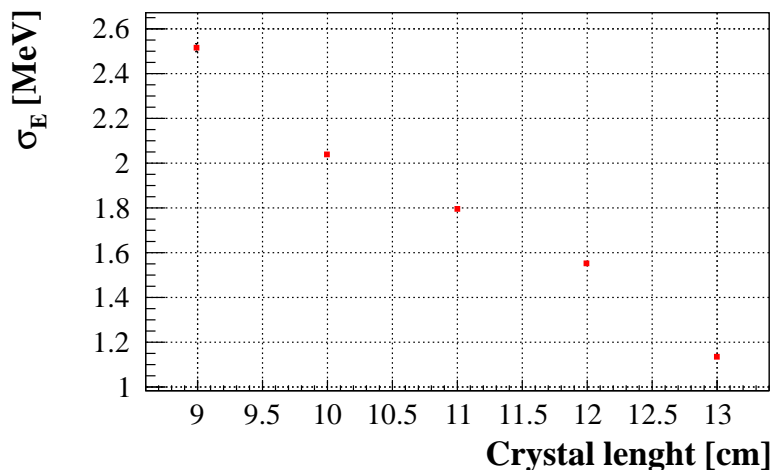
Figure 4.14: The plot shows the energy resolution (FWHM / 2.35) as a function of the crystal length [14].

The Mu2e collaboration selected the 11 cm length as reference solution: although this choice implies worst resolution (30%) with respect to a 13 cm long crystal, yet a 20-40% net saving is obtained.

4.4   Calibration and equalization methods

In order to provide the equalization between all the crystal, a relatively low energy source is desirable, but with an energy sufficiently high to produce signals well above electronic noise. The 6.13 MeV photon line from $^{16}O^*$ is well matching with this requirement.

$$^{19}F + n \rightarrow ^{16}N + \alpha$$
$$^{16}N \rightarrow ^{16}O^* \rightarrow ^{16}O + \gamma(6.13 \text{ MeV}) \tag{4.9}$$
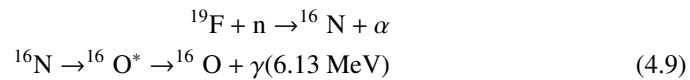
Such source has already been used successfully for routine weekly calibrations in an experiment [24]. As shown in 4.9 fluorine is activated with a neutron source, and ^{16}N isotope is produced. With a half-life of seven seconds ^{16}N decays into an excited state of ^{16}O, which in turn emits a 6.13 MeV photon.

The layout of reference [24] is shown schematically in figure (4.15). There are three
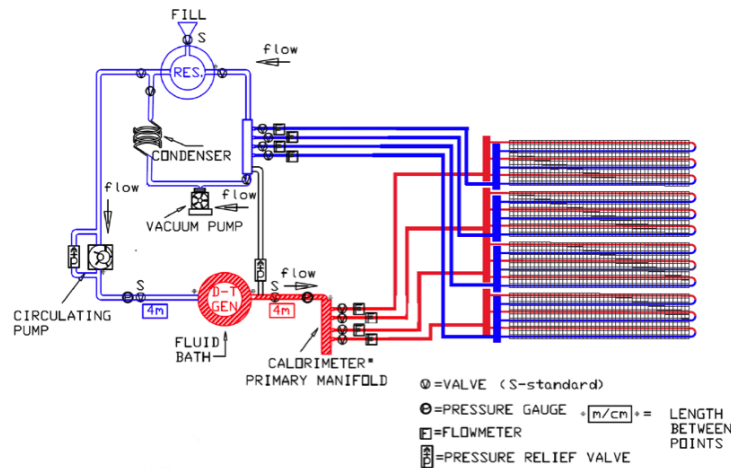
Figure 4.15: Scheme of the source calibration system.

principal contributions to the overall peak, one at 6.13 MeV, another at 5.62 MeV, and the third at 5.11 MeV, the latter two representing escape peaks. All three peaks have well-defined energies and thus all are useful in the equalization. In [24] calibrations were performed about once a month to a statistical uncertainty of $\leq 0.5\%$ and a systematic uncertainty of about 0.1%.

Changes of the crystal optical transmittance and of the APD gains will be monitored by means of a Laser system, following a scheme similar to the one used in [25]. A schematic diagram of the overall system is shown in figure 4.17:

For calibrating the calorimeter at higher energy (~ 100 MeV) the tracker will be used, as sources the calibration for the tracker is established [36]. Using $3\times1o^5$ reconstructed
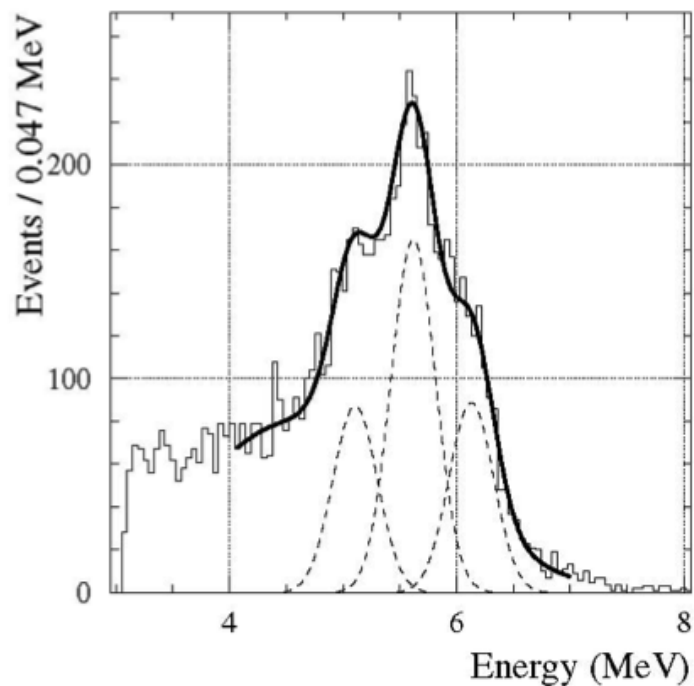
Figure 4.16: Energy spectrum in a BABAR CsI(Tl) crystal irradiated with 6.13 MeV photons from an $16O^*$ source [24] Readout is with a PIN diode. The solid curve is a fit to the data, including Gaussian contributions at 6.13 MeV, 5.62 MeV, and 5.11 MeV, indicated by the dashed curves.
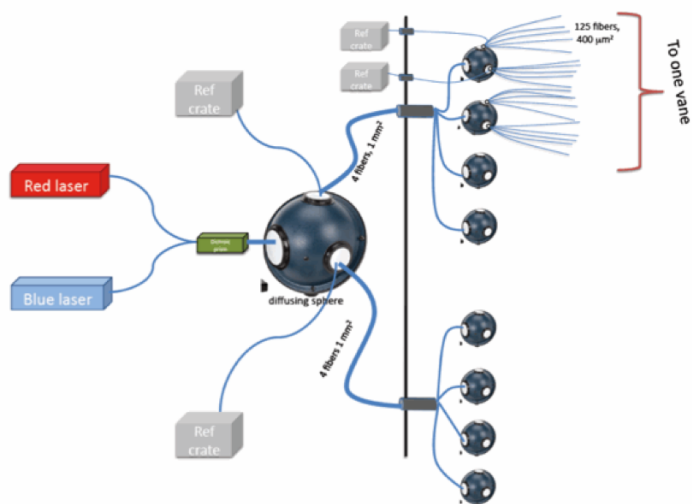

Figure 4.17: Laser control scheme.

DIO electrons in momentum range 69 - 81MeV a calorimeter calibration is achievable. Figures (4.18) and (4.19) show respectively the scatter plot of the reconstructed momentum versus the calorimeter response, and the related curve for the calorimeter calibration.
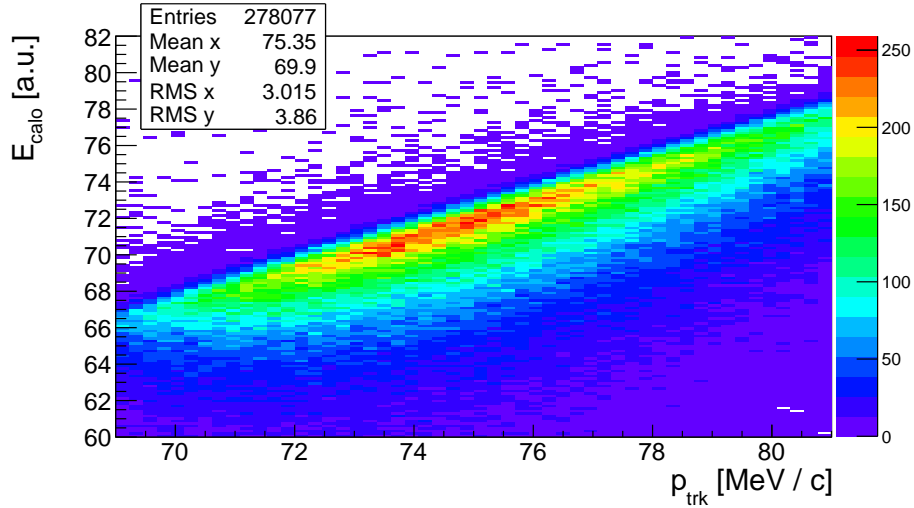
Figure 4.18: Scatter plot of the reconstructed momentum p_{try} (given in MeV) and the calorimeter response E_{Calo} (given in a. u.).
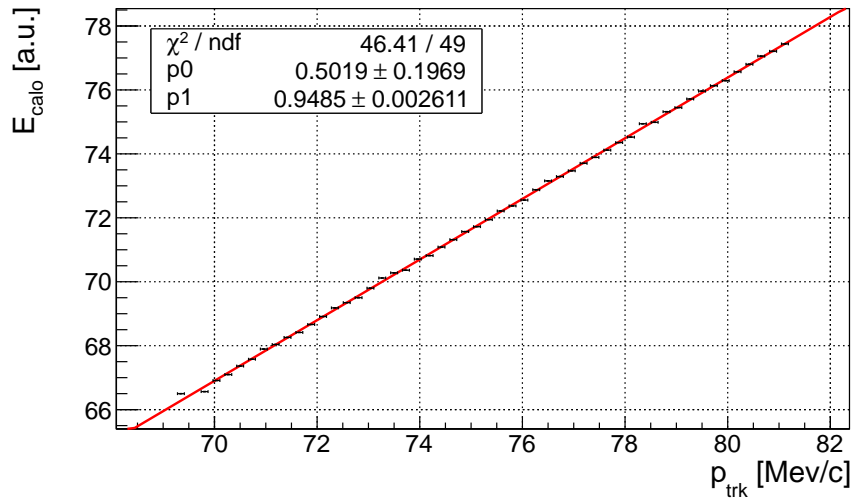
Figure 4.19: Calorimeter calibration curve; the data points are interpolated with a line $p_0 + p_1 x$. This plot is obtained by fitting slices of the scatter plot (4.18) with the logarithmic Gaussian function (4.5).

Figure (4.20) shows the calorimeter energy resolution when its response is corrected by the inverse of the linear function showed in figure (4.19) to correct the calorimeter
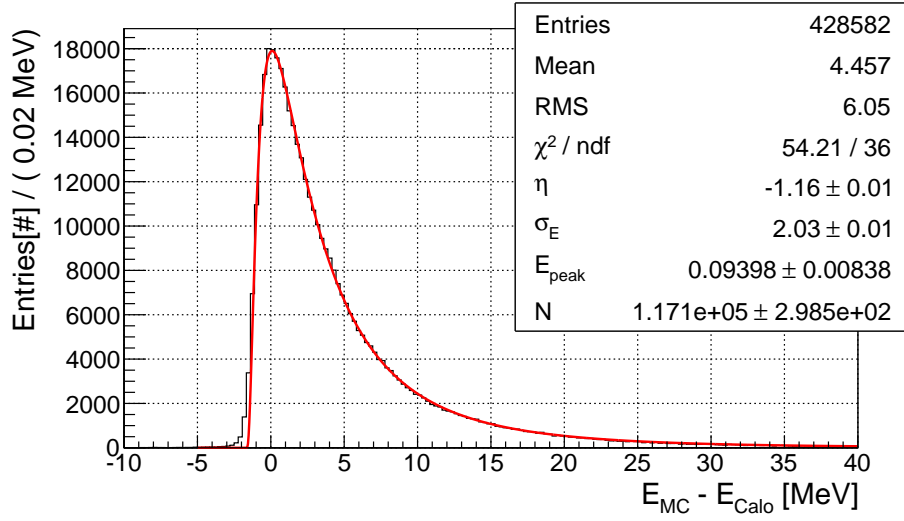
Figure 4.20: Plot of the calorimeter energy resolution after doing the calibration. E_{MC} represents the effective energy, E_{Calo} is the corrected calorimeter response. The distribution is fitted to the logarithmic Gaussian function 4.5.

response. The resulting energy resolution is $\sigma_E = (2.03 \pm 0.01)$ MeV, the peak value is $E_{peak} = 0.093 \pm 0.008$ MeV. So this scheme of calibration seems to be sufficient to satisfy the calorimeter requirements showed in section (3.2). An important parameter is the time needed for the calibration. Assuming a muon beam of $(5.26 \pm 0.52) \times 10^{14}$ $\mu^- stopped/day$ according t reference [14], simulation results shows that the number of DIO's with reconstructed momentum in the range 69 - 81 MeV/c is expected to be $(4.97 \pm 0.96) \times 10^7$ electrons / day. To create a calibration curve like the one of figure (4.19) about 3×10^5 reconstructed DIO's in the range 69 - 81 MeV/c are needed. Therefore:

$$
\begin{aligned}
\text{calibration time [minutes]} \quad &= \quad \frac{3 \times 10^5}{4.97 \times 10^7 (\mu^- stopped/day) \cdot 24(hours) \cdot 60(minutes)} \\
&\approx \quad 8 \text{ [minutes]}
\end{aligned}
$$

So the calibration time is really fast.

4.5 Apex reconstruction

A good determination of the particle impact point on the calorimeter is needed to perform a matching between reconstructed tracks and the calorimeter clusters. The search
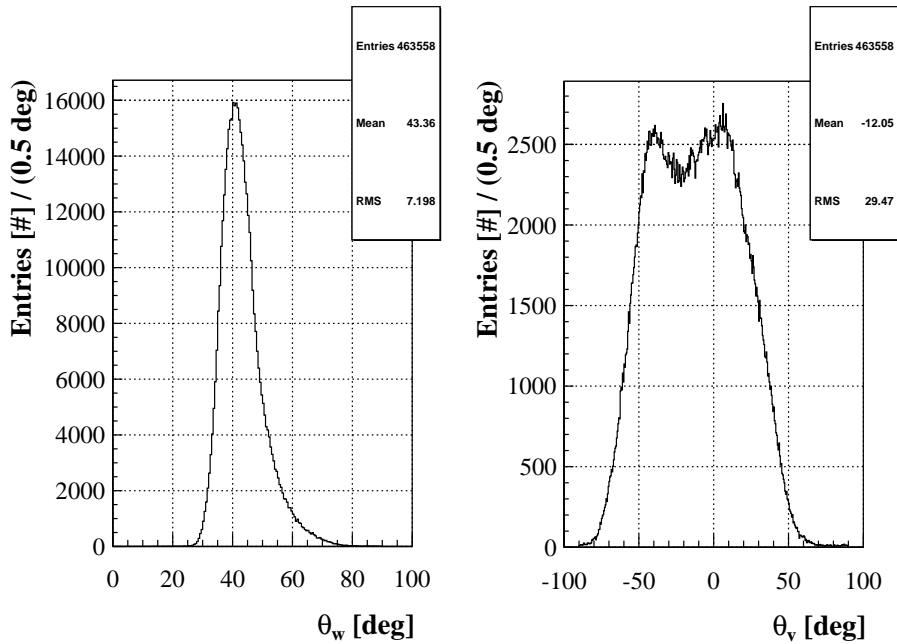

Figure 4.21: Distribution of the impact angle in the *w* and *v* directions.

for the cluster apex starts with the identification of the cluster center of gravity (COG), obtained by weighting the fraction of the cluster energy collected in each crystal. For each these resulting coordinates (v_{COG}, w_{COG}) were applied different set of corrections (the two directions are not equivalent due to the presence of the magnetic field). The need of different set of corrections is evident in figure (4.21), where the impact angle distribution for each plane, one orthogonal to the vane along the *v* direction and the other along the *w* direction, are shown. The θ_w (impact angle projected on the w-orthogonal plane) distribution has a mean of $\approx 43°$ because the electrons are boosted to the downstream part of the Detector Solenoid (DS).

To calculate the *w* coordinate with best accuracy, than the one reached with the COG algorithm, two informations of the reconstructed cluster are used: 1) the position of the most energetic crystal ($w_{cryMaxE}$), 2) the extension of the cluster (in crystal unit) along the *w* direction. To study the correlation between w_{COG} and $w_{cryMaxE}$, a scatter plot of the relative distances of the *w*-coordinate of the real impact point (w_{MC}) and of w_{COG} from $w_{cryMaxE}$ was made (see figure (4.22 top left).
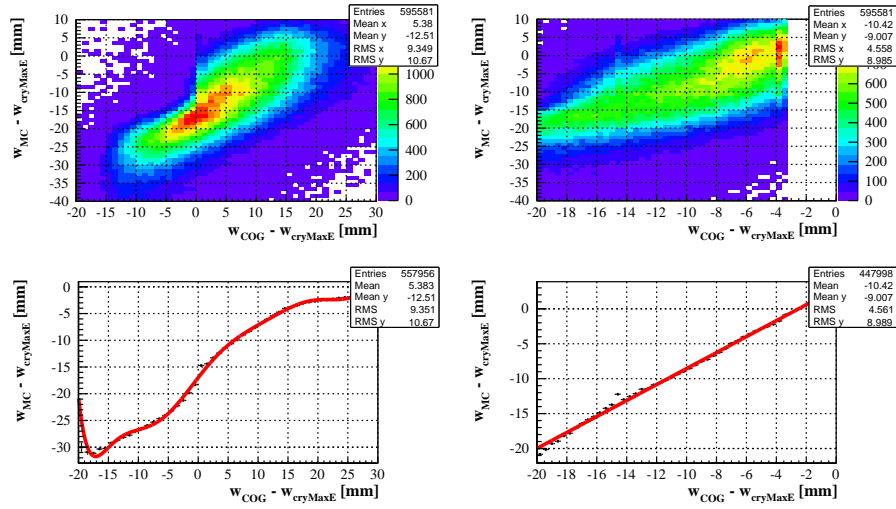
Figure 4.22: Upper left side: correlation between the linear COG (w_{COG}) and the position of the most energetic crystal ($w_{CryMaxE}$). Bottom left side: profile of the previous plot; a fifth degree polynomial function represents the red line which fits the profile. Right side: plots after correction; the slope of the profile (bottom right side) is close to one, so the correlation is almost removed.

So using the polynomial function ($F_1(x)$) which fits the profile of the plot in figure (4.22 top left), the new coordinate (w_{COG1}) was defined as follow:

$$w_{COG1} = w_{cryMaxE} + F_1(w_{COG} - w_{cryMaxE})$$

Figure (4.23) shows that the resolution achieved by using w_{COG1} is ≈ 7.2 mm. As a check that w_{COG1} was uncorrelated with $w_{cryMaxE}$, a scatter plot of the distances (w_{MC} - $w_{cryMaxE}$) and (w_{COG1} - $w_{cryMaxE}$) was made (see figure (4.22 top right)); its profile (see figure (4.22 bottom right)) fits quite good with a line $p_0 + p_1 x$, with $p_0 \approx 0.2$ and $p_1 \approx 1$, showing that the correlation with $w_{cryMaxE}$ was almost removed.
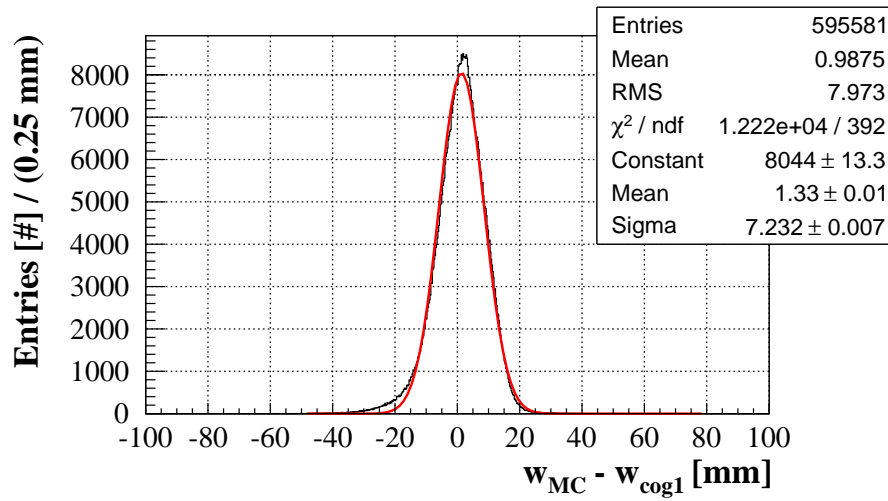
Figure 4.23: Resolution plot of the w_{COG1} coordinate; w_{seed} is the real coordinate and w_{COG1} is the corrected coordinate of the cluster.

A similar procedure was used such to use the information about the cluster extension along the w direction: so starting from the scatter plot of the cluster extension on the w direction with respect to the distance ($w_{MC} - w_{COG1}$) (see figure (4.24 top left)), a polynomial function $F_2(x)$ was obtained by the fitting its profile (see figure (4.24 bottom left)). Then the function $F_2(x)$ was used to define the new w-coordinate of the cluster w_{COG2} as follows:

$$w_{COG2} = w_{COG1} - F_2(\text{cluster w-extention})$$

Fit results from figure (4.25) shows that the resolution on the w coordinate is ≈ 6.5 mm.
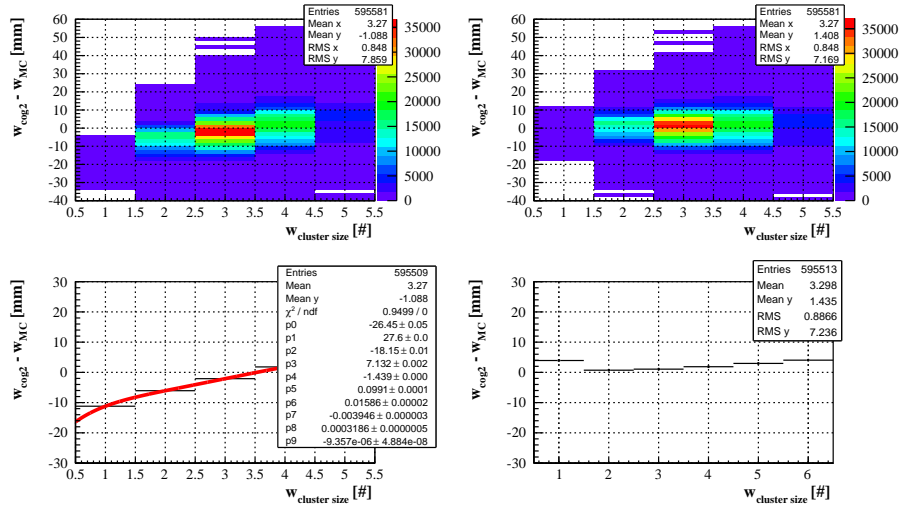
Figure 4.24: Resolution plot of the *w* coordinate after applying the first correction to the linear COG; w_{seed} is the MC coordinate and w_{COG1} is the corrected coordinate of the cluster.
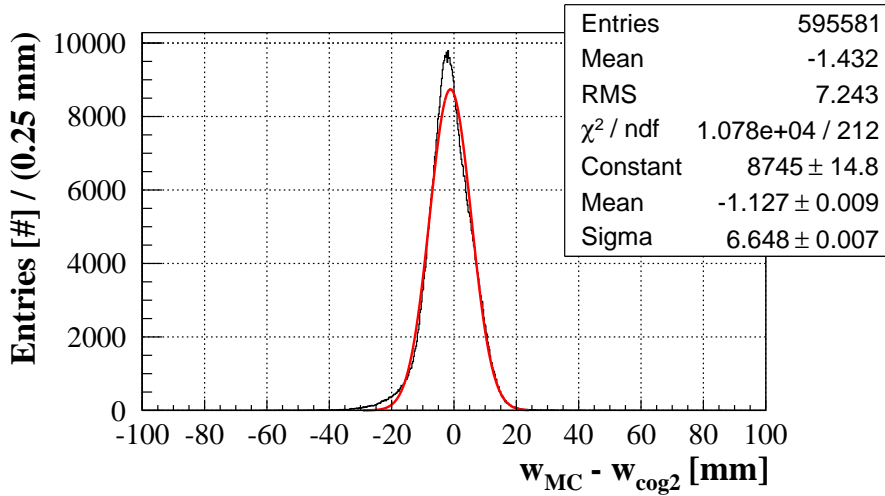

Figure 4.25: Resolution plot of the *w* coordinate after applying the second correction to the linear COG; W_{MC} is the real coordinate and W_{COG2} is the corrected coordinate of the cluster.

Figure (4.26) show the resulting resolution on the *v*-coordinate if v_{COG} is used to identify the *v*- coordinate of the reconstructed cluster.

56
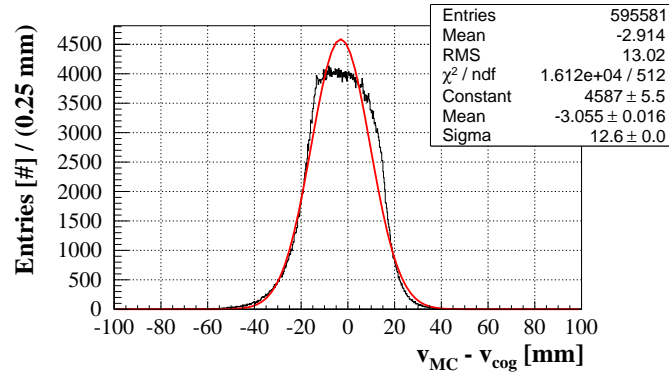
Figure 4.26: Resolution plot of the *v* coordinate after applying the correction to the linear COG.

For performing this result tthe only information that was used is about the impact angle along the *v* direction (θ_v); this decision follows the fact that both informations that were used for the evaluation of the *w*-coordinate are strictly dependent on the impact angle, which has a wide range along the *v*-direction (see figure (4.21 right)).

To study the correlation between v_{COG} and θ_v, a scatter plot of the distance of the *v*-coordinate of the real impact point (v_{COG}) from v_{MC} and θ_v was made (see figure (4.27 top left). Then, using the polynomial function ($G_1(x)$) which fits the profile of the plot in figure (4.27 top left) (see figure (4.27 bottom left)), the new coordinate (v_{COG1}) was defined as follow:

$$v_{COG1} = v_{COG} - G_1(\theta_v)$$

Figure (4.28) shows that the resolution achieved by using v_{COG1} is ≈ 7 mm. As a check that v_{COG1} was uncorrelated with θ_v, a scatter plot of the distances (w_{MC} - $w_{cryMaxE}$) and (w_{COG1} - $w_{cryMaxE}$) was made (see figure (4.22 top right)); its profile (see figure (4.27 bottom right)) is quite similar to a flat distribution set at zero, showing that the correlation with θ_v was almost removed.

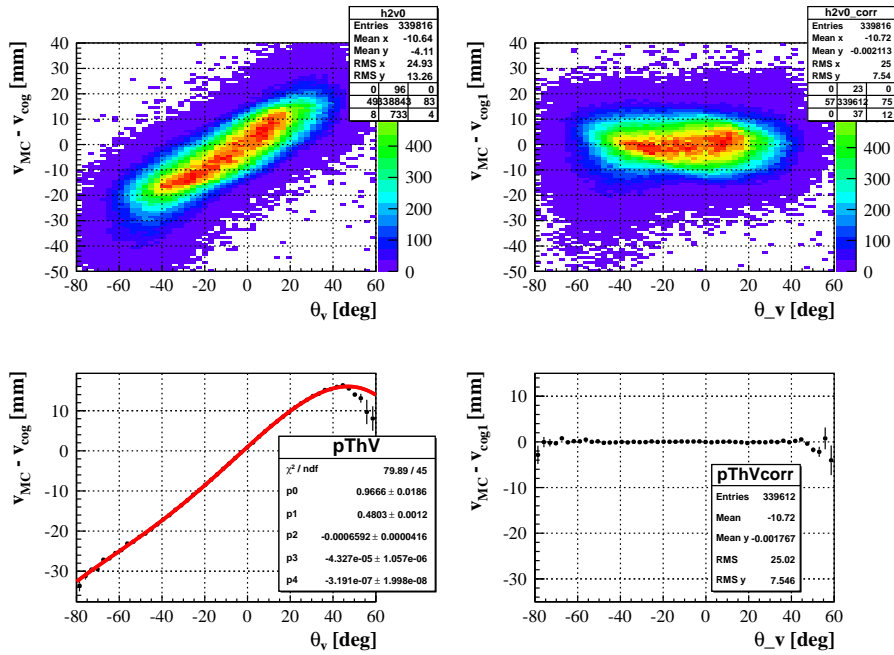Fit results from figure (4.28) shows that the resolution on the *w* coordinate is ≈ 7.0 mm.

Figure 4.27: (Top-left) the relation between the linear COG (v_{COG}) and the impact angle (θ_v) is shown. (Bottom-left) profile histogram of the previous correlation; a fifth degree polynomium function is used to fit the profile (red line). On the right side there are the equivalent plots after applying the correction; the profile in the bottom right side shows that the correlation is practicallyremoved.
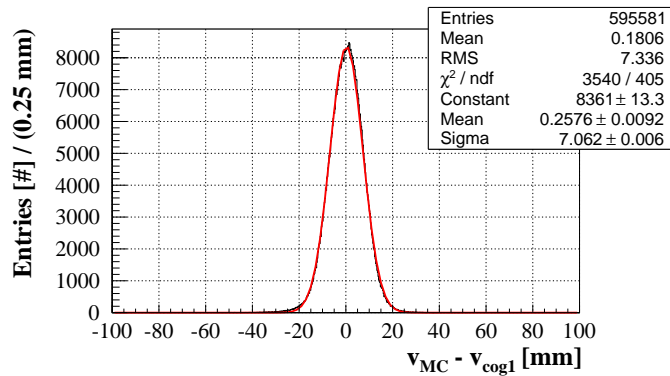

Figure 4.28: Resolution plot of the v coordinate after applying the correction to the linear COG.

4.6   Calorimeter and tracker information

Track extrapolation

Mu2e Tracker measures the momentum and the timing of the electron. The trajectory, reconstructed in the tracker [37], is extrapolated to the calorimeter using a linear extrapolation method and the impact point is calculated. Along the extrapolated path, the electron energy degrades due to the crossing of straws, tracker wall. This energy loss is calculated and correction on the trajectory is made.

The residuals for both coordinates (w and v) are showon in figures 4.29.The radial coordinate (v in the local vane frame) is extrapolated with better precision ($\sim$ 7 times) than the axial coordinate (w in the local vane frame).
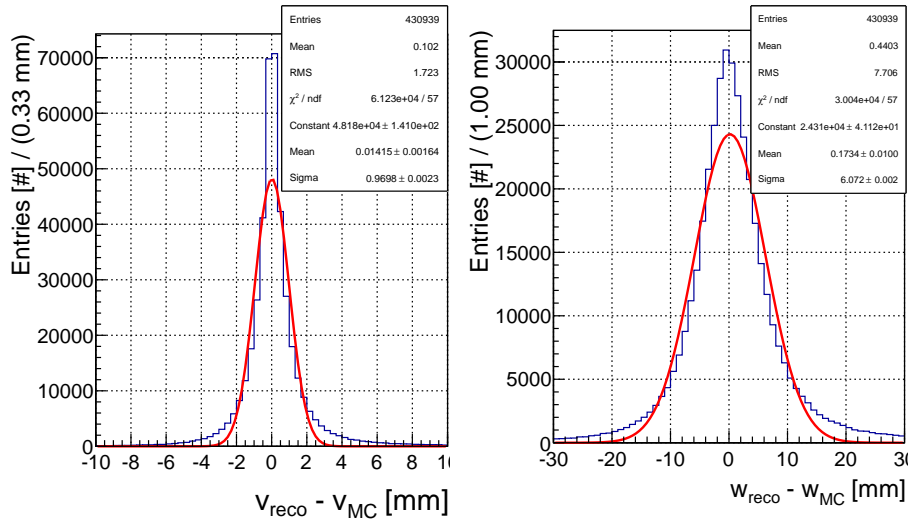

Figure 4.29: Distributions of the residuals of the two coordinates given in the local vane frame; v_{reco} and w_{reco} are the reconstructed impact positions, v_{MC} and w_{MC} are the values from Monte Carlo.

In figure (4.30) the residual for impact angles (θ_v and θ_w) are shown: both angles have a resolution better than $\approx 0.5°$
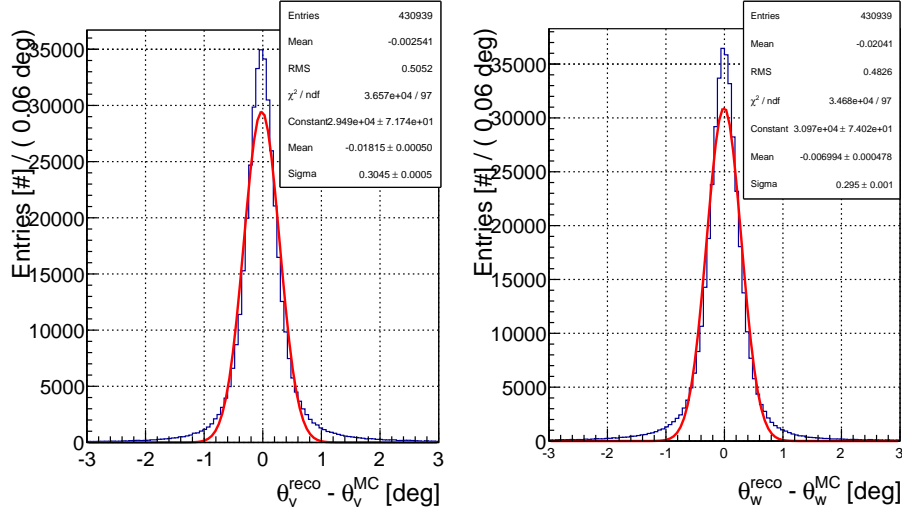
Figure 4.30: Distributions of the residuals of the two impact angles: θ_v^{reco} and θ_w^{reco} are the reconstructed impact angles, θ_v^{MC} and θ_w^{MC} are the values from Monte Carlo.

Track-cluster matching

In Mu2e experiment this matching is required because the calorimeter provides independent information useful either in likelihood analyses, and with Kalman filter to recover bad reconstructed tracks.

In the adopted to each reconstructed tracks a cluster is associated if the following function is minimized:

$$\Theta\left(t_{trj}, t_{clu}, p_{clu}, p_{trj}\right) = \frac{\left(t_{trj} - t_{clu}\right)^2}{\sigma_t^2} + \frac{\left(p_{i,trj} - p_{i,clu}\right)^2}{\sigma_{p_i}^2} \tag{4.10}$$

where:

- t_{trj} is the impact time of the reconstructed electron;

- t_{clu} is the cluster time;

- p_{trj} is the impact position of the reconstructed track in the local vane frame;

- p_{clu} is the cluster position.

The values of σ_t and σ_{p_i} were taken from the residuals plots the time and positions showon in figures (4.31), (4.32), (4.33), which are obtained from the simulation of the calibration run (DIO with reconstructed momentum ≥ 69 MeV):
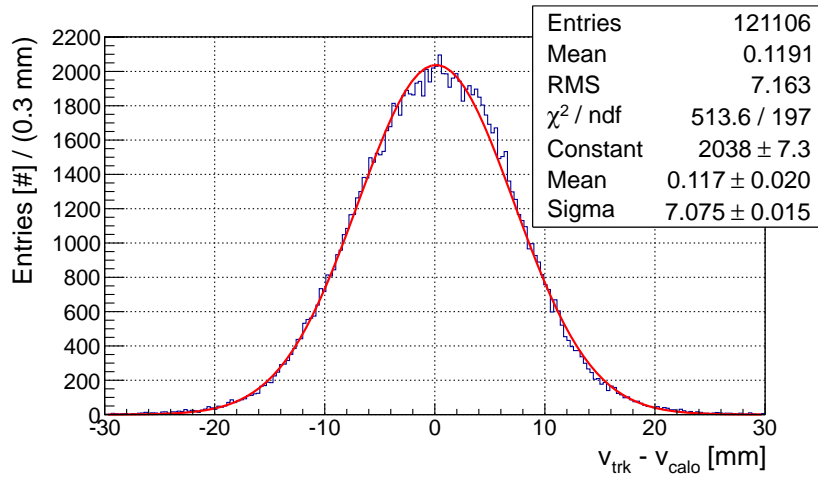
Entries	121106
Mean	0.1191
RMS	7.163
χ^2 / ndf	513.6 / 197
Constant	2038 ± 7.3
Mean	0.117 ± 0.020
Sigma	7.075 ± 0.015

Figure 4.31: Distributions of the residuals of the v coordinate; v_{trk} is referred to the extrapolated trajectory, v_{call} to the calorimeter.
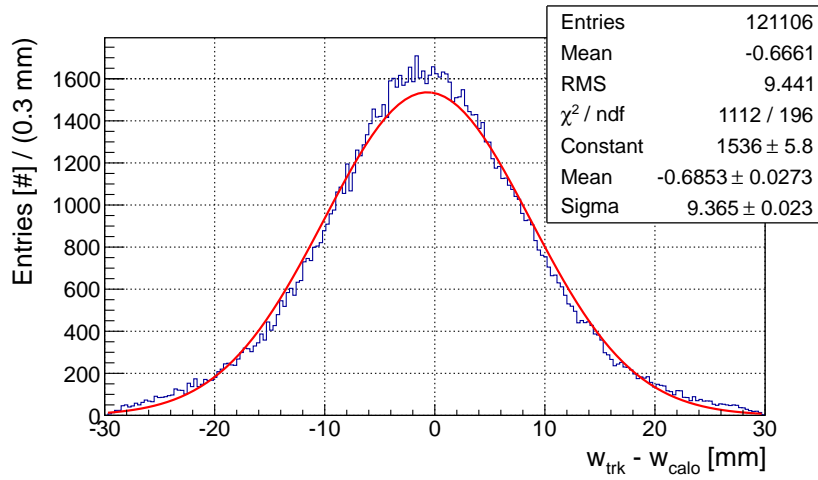

Entries	121106
Mean	-0.6661
RMS	9.441
χ^2 / ndf	1112 / 196
Constant	1536 ± 5.8
Mean	-0.6853 ± 0.0273
Sigma	9.365 ± 0.023

Figure 4.32: Distributions of the residuals of the w coordinate; w_{trk} is referred to the extrapolated trajectory, w_{call} to the calorimeter.

Eq.(4.10) does not use any information about the cluster energy or the track momentum: in this way no dependence on energy is introduced and comparison between track and cluster are unbiased.
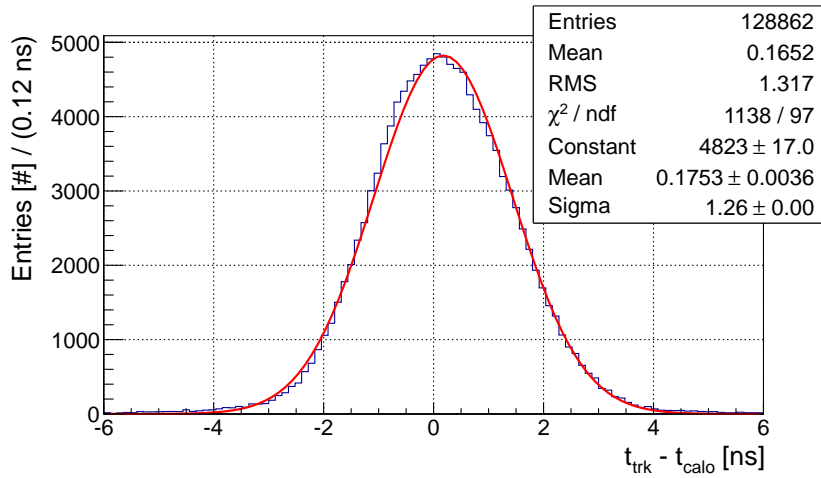
Figure 4.33: Distributions of the residuals of the impact time: t_{trk} is the trajectory extrapolated time and t_{calo} is the cluster formation time.

4.7 Experimental test on small size prototipe

In this section the results of a test Beam at Mainz Microton (MAMI) (executed on March 2011) are reported. For this beam test 9 LYSO crystals were included to a crystal matrix built at Frascati National Laboratory (LNF) [9].

The LYSO crystals (from the Shanghai Institute of Ceramics, Chinese Academy of Sciences (SICCAS)) had dimensions $20 \times 20 \times 150$ mm^3 and were surrounded by a "leakage recovery matrix" of PWO$_4$ crystals. figure (4.34) shows the matrix layout: Each LYSO crystal was read out by a single Hamamatsu S8664-1010 APD followed
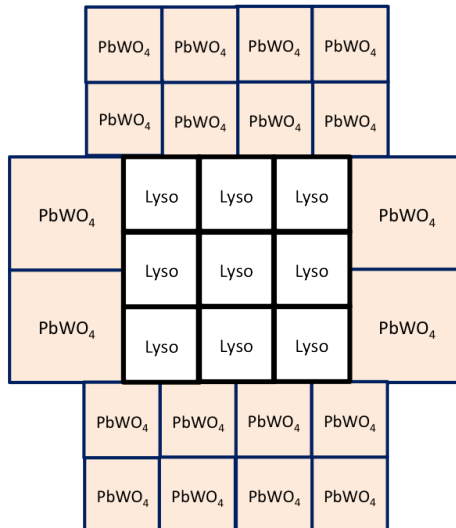

Figure 4.34: Matrix layout: on the inner side there is a 3 X 3 matrix of LYSO crystals, the outer crystal are PbWO$_4$.

by a discrete voltage amplifier, while the PWO$_4$ crystals were read out by conventional Hamamatsu PMTs. The bias to the APD's was provided by a Mu2e prototype high voltage board while the PMT high voltage was supplied by a CAEN High Voltage board.

The APD's were operated at ~ 50 V below the breakdown voltage at an average gain of ~300. The temperature stability of the APD's was maintained by adding two Peltier junction cells to a copper mask positioned on the calorimeter face and monitored by two thermo sensors. The data were taken with the APD temperature held at (24.5°± 0.5°) C. The transverse coverage for the matrix was ~2.5 R$_m$ (Molier radii). Each channel was calibrated with an accuracy of 2% by means of cosmic rays. The crystals were exposed to a tagged electron beam with energies ranging from 20 up to 400 MeV.The beam spot was ~8 mm in diameter. The trigger was provided by the coincidence between the discriminated sum of the matrix and the reference tagging signal. Data were taken at twelve different energies over a period of 2 days. Approximately 10,000 events were collected at each energy.
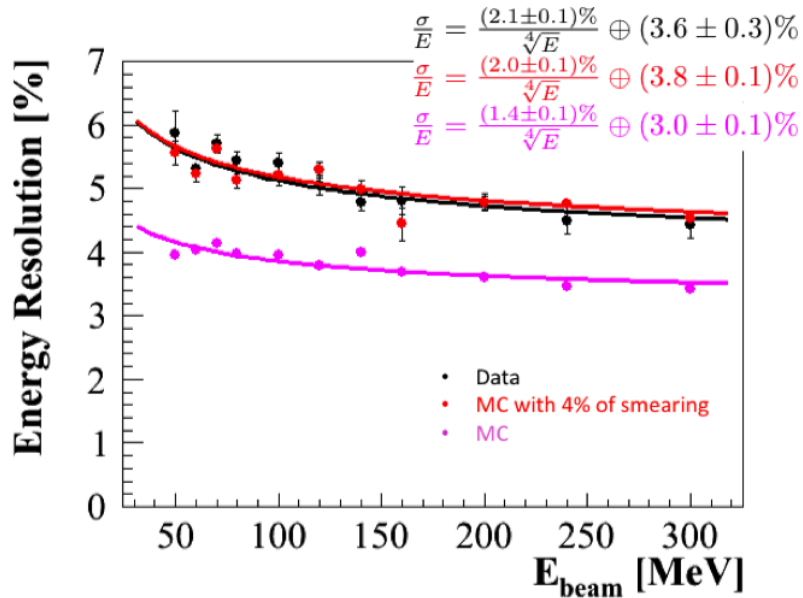

Figure 4.35: Test Beam results from MAMI. The measured energy resolution of the overall LYSO crystal matrix (black points) is compared to simulations (magenta curve). To obtain reasonable agreement with the data, the energy response of each crystal was smeared by 4% in the simulation (red curve).

Figure (4.35) shows the dependence of the energy resolution as a function of beam energy for test beam data (black points) and for the simulation (magenta curve). A fit to the data results in a stochastic term of 2.4% with an $E^{1/4}$ dependence, a negligible electronic noise term and a constant term of 3.2% due to shower leakage.

To obtain reasonable agreement with the data, the energy response of each crystal was smeared by 4% in the simulation using a Gaussian distribution. This was the fastest way to simulate the physical effects which were not included in the Monte Carlo simulation (like Longitudinal response uniformity and non-linearity). The LYSO crystals used for building this matrix were not treated to be uniformed below the 5 % (as asserted in the previous sections) and that clearly degraded the energy response. Introducing this smearing a good agreement between data and Monte Carlo is found, as shown in figure (4.35) and figure (4.36), for the raw energy distribution of the 9 inner LYSO crystals and their sum.
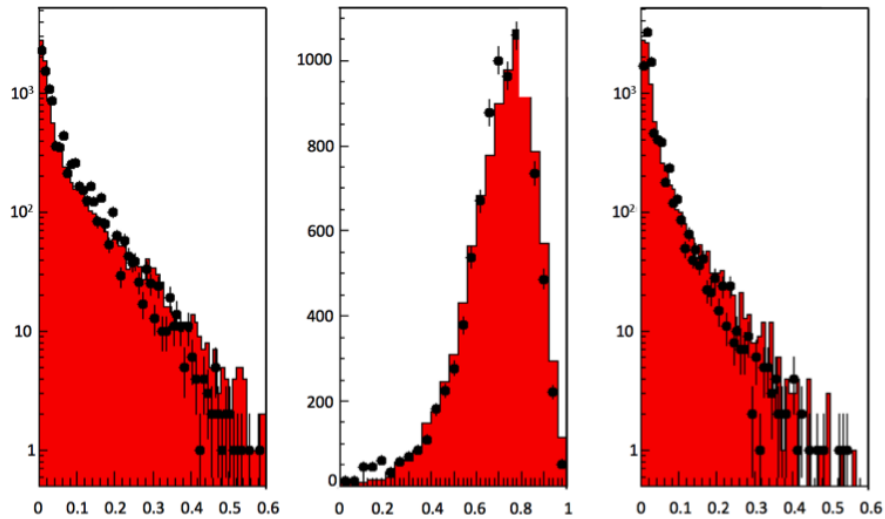

Figure 4.36: The LYSO crystal array in front of a tagged photon beam at MAMI. The three plots correspond to the 3 crystals in the center row of the LYSO array. The ratio of the crystal response to the beam energy is plotted in each case. The photons are incident on the center crystal (center plot). The raw energy distributions of the LYSO matrix (black data points) are compared to a GEANT-4 [17] simulation of the array (red histogram).

64

The position resolution of the LYSO array was also studied at MAMI and good agreement between data and Monte Carlo was obtained. Position reconstruction was done using a simple energy weighted centroid method. Figure (4.37) shows the average reconstructed position for 100 MeV electrons hitting the central crystal in the array at normal incidence. The reconstructed position as a function of the impact point exhibits
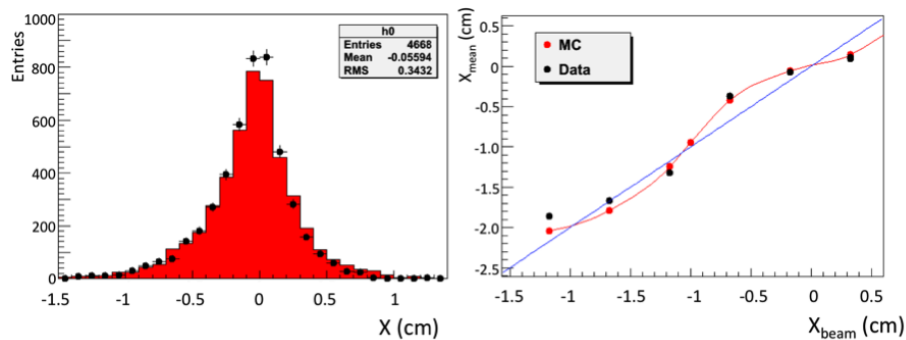

Figure 4.37: Position reconstruction for 100 MeV electrons at normal incidence with the beam hitting the central crystal. Data were taken at MAMI beam test.

a typical S-shape curve response, with a resolution of $\approx$ 3 mm.

Studies of the time resolution of the LYSO array at MAMI were limited by the large intrinsic timing jitter of the reference tagging signal (~800 ps). In a previous beam test at the Frascati Beam Test Facility [38], time resolution below 200 ps was obtained with an LYSO array exposed to 100 MeV electrons.

Chapter 5

Study of Sensitivity in a calorimeter stand alone configuration

5.1 Concept of Sensitivity

A rare-process experiment (such as Mu2e) relies on its sensitivity, so the design of the experiment must follows an optimization procedure based on a specific "figure of merit".

The most "significance-like" parameters that are commonly used for optimization process are:

1. $\frac{S}{\sqrt{B}}$;

2. $\frac{S}{\sqrt{B+S}}$;

where S is the number of signal events and B of the background.

Expression 2 cannot be maximized without knowing explicitly the cross section of the searched signal; furthermore it is more related to the uncertainty in the measurement of the yield from a new process (if any) rather than to significance. Expression 1, being linear in S, has the good property to be independent of the process cross section, but it has the problem of breaking down for small values of B. In the Mu2e Collaboration, there is still an open discussion of which is "the best figure of merit to choose". The proposed definition of "sensitivity" which are discussed here are:

1. 90%C.L. Sensitivity [39];

2. "Punzi" Sensitivity [40].

To compare the two methods, the experiment sensitivity was calculated assuming to make an analysis where only the calorimeter detects electrons. In this way, it is possible to test the performance of a LYSO calorimeter with $\approx 2\%$ energetic resolution and also to verify that a sensitivity goal of about $\approx 10^{-16}$ can be reached even in the

case of unexpected malfunctioning of the tracker. These sensitivity estimates were performed including all the information about the background spectra and the resolution functions previously calculated within the Mu2e framework. Figures (5.1) and (5.2) show respectively the conversion electron and the background spectra (at the entrance of the calorimeter) convoluted with the calorimeter energy resolution function reported in figure (4.20).
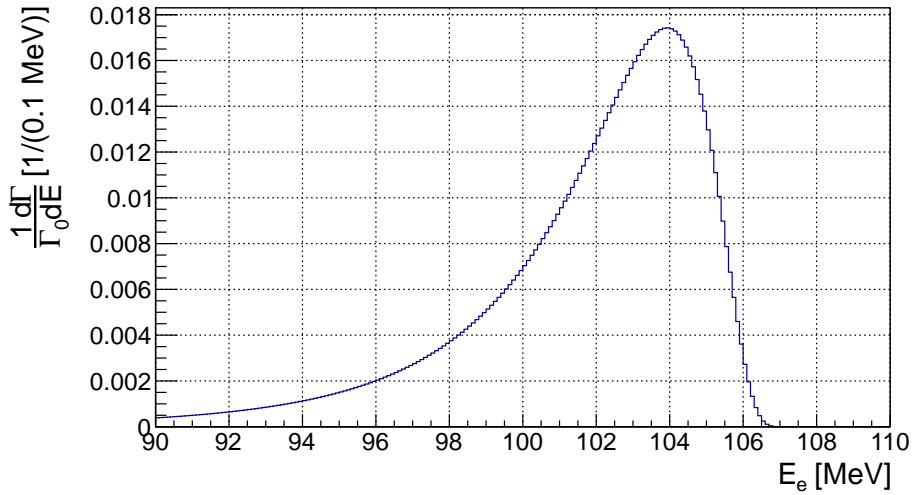

Figure 5.1: Conversion electron spectrum convoluted with the calorimeter energy resolution function reported in figure (4.20).
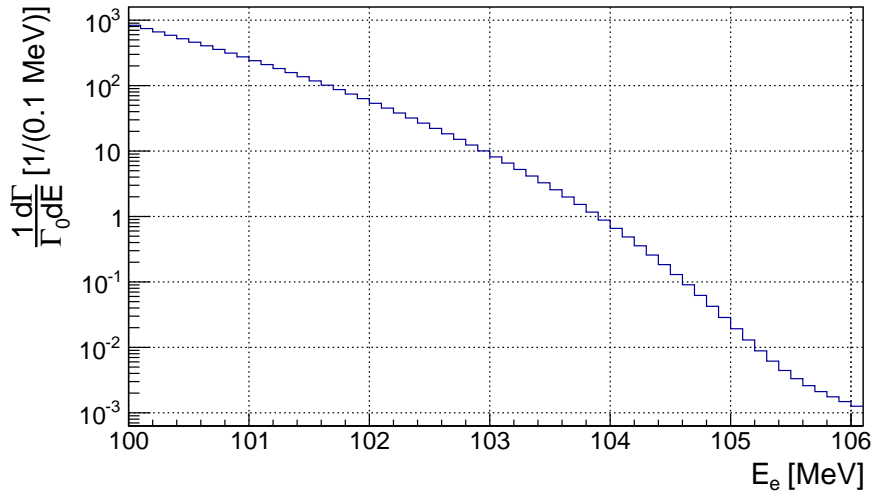

Figure 5.2: Background spectrum convoluted with the calorimeter energy resolution function reported in figure (4.20).

5.1.1 Punzi - Sensitivity

"Punzi" - Sensitivity (S) is defined such that if the true branching ration (BR) is $\leq$ S then the probability of 3σ evidence is $\geq$ 90%. This implies that if there is no a 3σ evidence then an upper limit $BR_{UppeLimit} \leq$ S at 90% confidence level can be set. There are several reasons to use it:

- It is a statistic definition with a simple and clear interpretation;

- It is a good metric both to make discovery and to set a limit;

- It is generally applicable to any search for new phenomena.

This definition of sensitivity was proposed [41] as a target for optimization, because it depends only on the nature of the experiment, and not on what hypothetically can be observed.

The best signal window was then obtained by doing a scan on the energy range and choosing the lower E_{min} and the upper E_{max} values such to optimize the sensitivity: figures (5.3) shows as example of the scan on the lower energy cut that was made for the calorimeter. Table 5.1 shows the results of this optimization procedure:
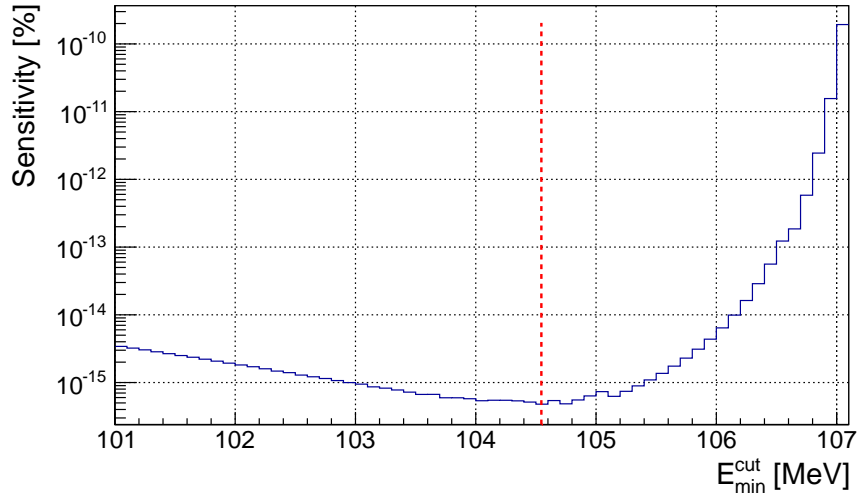

Figure 5.3: The plot shows the scan of the sensitivity with respect to the lower energy cut.

	Calorimeter	Tracker
Punzi Sensitivity	4.79×10^{-16}	1.39×10^{-16}
Expected background events	0.42 ± 0.12	0.46 ± 0.13
Number of events for 3σ discovery	4	2
E_{min} [MeV] (p_{min} [MeV/c])	104.55	103.76
E_{max} [MeV] (p_{max} [MeV/c])	108.25	107.44

Table 5.1: The table shows the sensitivity reached by the tracker and the calorimeter.

The sensitivity reached by the calorimeter is 4.79×10^{-16}, which is approximately four times worse than that one achievable by the tracker. This represents a good result and also shows that the optimum configuration of the detector should be a good compromise between the acceptance and the resolution. For the tracker the reconstruction cuts represent the main source for the acceptance degradation; studies are underway to modify the Kalman filter such to use the information from the matching with the calorimeter in order to help the tracker on the track reconstruction. Indeed a combined analysis with a likelihood method will be tried once all the reconstruction of tracking, calorimeter and track to calorimeter association will be completed in the framework.

To guide the understanding of the resolution and background, in Figure (5.4) the resolution convoluted background and the convoluted signal spectra are shown in the same plot, in the hypothesis of a branching ratio for the conversion process of 10^{-15}.
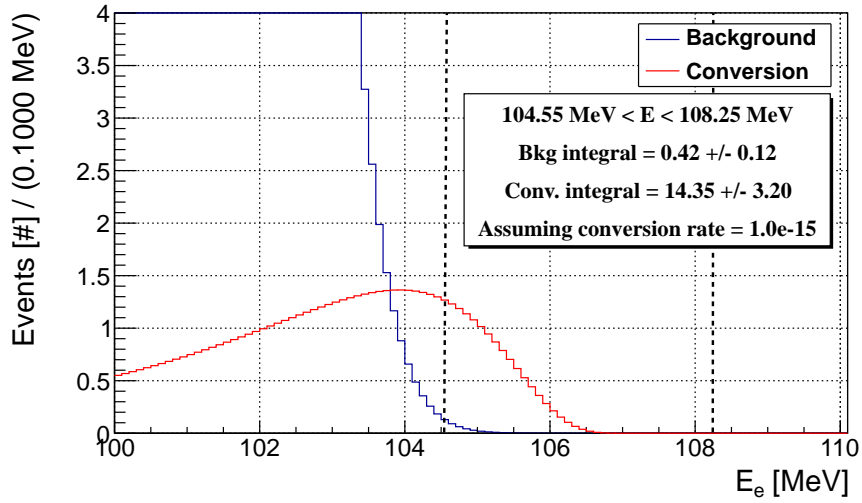

Figure 5.4: Plot of the convolution of the backgrounds and the signal electrons with the Calorimeter response function.

In order to understand how the sensitivity scales with respect to the calorimeter energy resolution, the same calculation was made by deteriorating the energy resolution function from 2.5% to 4%. Table (5.2) shows that a calorimeter with a resolution worst than $\approx 2.5\%$ reaches a sensitivity of $\approx 10^{-15}$ which is up two order of magnitude lower than the experiment goal.

σ_E [MeV]	2.03	2.50	3.00	3.5 0	4.00
"Punzi" Sensitivity	4.79×10^{-16}	6.60×10^{-16}	8.44×10^{-16}	1.07×10^{-15}	1.32×10^{-15}
Background events	0.42 ± 0.12	1.13 ± 0.31	0.75 ± 0.20	0.73 ± 0.20	0.75 ± 0.44
Events for 3σ discovery	4	6	5	5	5
E_{min} [MeV]	104.55	104.75	105.35	105.85	106.35
E_{max} [MeV]	108.25	108.95	109.65	110.35	111.05

Table 5.2: The table shows the sensitivity reached by calorimeter with respect to the achieved energy resolution σ_E.

5.1.2 90% C.L. Sensitivity

The 90% Confidence Limit Sensitivity is taken in the sense of the Feldman-Cousins confidence limit belt construction [39]. It is the "sensitivity" that they suggest reporting, defined as the average upper limit that would be obtained by an ensemble of experiments with the expected background and in case of no signal.

This represents the definition also adopted by other experiments on "rare processes", like MEG [6], COMET [14] and SINDRUM [4].

As in the previous case, a scan for optimizing the signal window was carried out. Table (5.3) shows the results on both calorimeter and tracker only configurations:

	Calorimeter	Tracker
Sensitivity @ 90% C.L.	1.21×10^{-16}	5.11×10^{-17}
Expected background events	0.74 ± 0.20	0.91 ± 0.25
E_{min} [MeV] (p_{min} [MeV/c])	104.45	103.26
E_{max} [MeV] (p_{max} [MeV/c])	107.25	107.38

Table 5.3: The table shows the sensitivity reached by the calorimeter (left) and tracker (right) and the corresponding expected background. E_{min}^{cut} and E_{max}^{cut} (expressed in MeV) are the lower and upper bounds of the optimum signal window found.

In this case the calorimeter will reach a 90% C.L. sensitivity of 1.21×10^{-16}, which is a factor of 4 smaller than what obtained with the "Punzi" sensitivity method.

Chapter 6

Conclusion

In the last year a lots of studies were done to validate the calorimeter performance for the Mu2e Experiment, and in this thesis some of the most improvements reached were presented.

By using the most recent experimental results [31, 34, 42] physical and tecnical effects were included in the official Mu2e framework in order to make a more realistic simulation of the calorimeter response. A complete set of algorithms for the time, position and energy reconstruction of the electromagnetic cluster has been also performed.

A first scheme for the "in situ" calibration (based on E/p comparison with tracked decay-in-orbit electrons), and the estimated time necessary have been also presented.

Moreover, a matching algorithm, that associates the tracks and electromagnetic clusters with high efficiency, was implemented.

This method allowed to implement also an in-situ calibration algorithm based on comparison of reconstructed energy and track momentum for DIO events.

Results of two tests beam with a small LYSO array [29] proved both that the timing resolution is excellent, $\approx$ 150 ps, and allowed to validate the importance of many physical effects (such as longitudinal non uniformity and non-linearity response) that could degrade the energy resolution of LYSO crystals. Moreover, by comparing the presented simulation results with the presented test beam it emerges that, when all the physics effects were included in the simulations, the most relevant one to control is the longitudinal not-uniformity of the crystals.

Finally, the proposed definitions of sensitivity discussed in the Mu2e collaboration have been shown, and an estimate of the sensitivity achievable by the experiment using only the calorimeter information has been presented.

A new test beam with a bigger LYSO matrix is planned, such to study how the LYSO response can be improved using specific treatment of the crystals [35].

Appendix A

Alternatives

This appendix will discuss about the alternative geometries (disk geometry and tilted vanes), chosen of crystals (PbWO$_4$) and readouts (SiPm).

A.1 Geometry

Since the conversion electron tracks enter the vanes at the average angle of about 45°, how the efficiency can be improved tilting the vanes was also studied; in that way the fraction of front face hits increase relative to lateral or bottom edge hits. Figure A.1 shows the comparison between the nominal vane orientation with the tilted configuration. The vanes are tilted about an axis parallel to the solenoid axes centered at 54 cm from the axes. Figure A.2 shows that tilting the vanes by ~ 0.4 radians improves the reconstruction efficiency for good tracks after fiducial [**?**] cuts to 78%. The improvement is due to the reduction of the number of hits on the inner edge of the vane, with a corresponding increase of hits on the face. The downside of this configuration is that the effective thickness of the calorimeter in radiation lengths is reduced, since the tracks enter the vane face at closer to normal incidence.
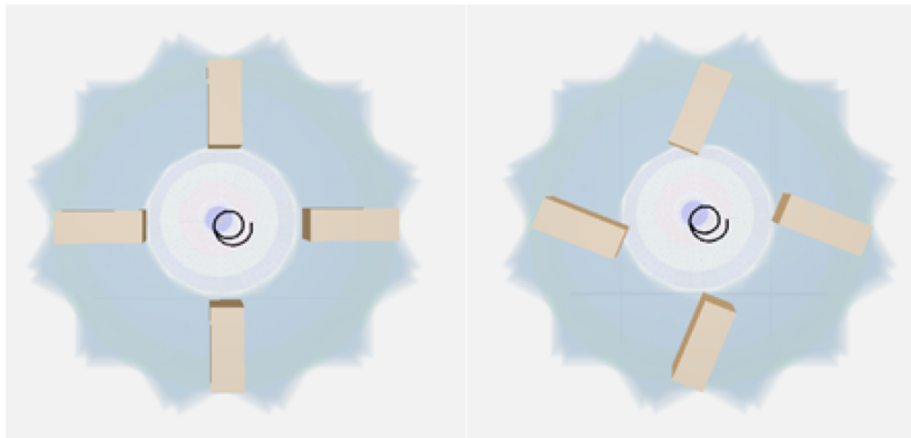
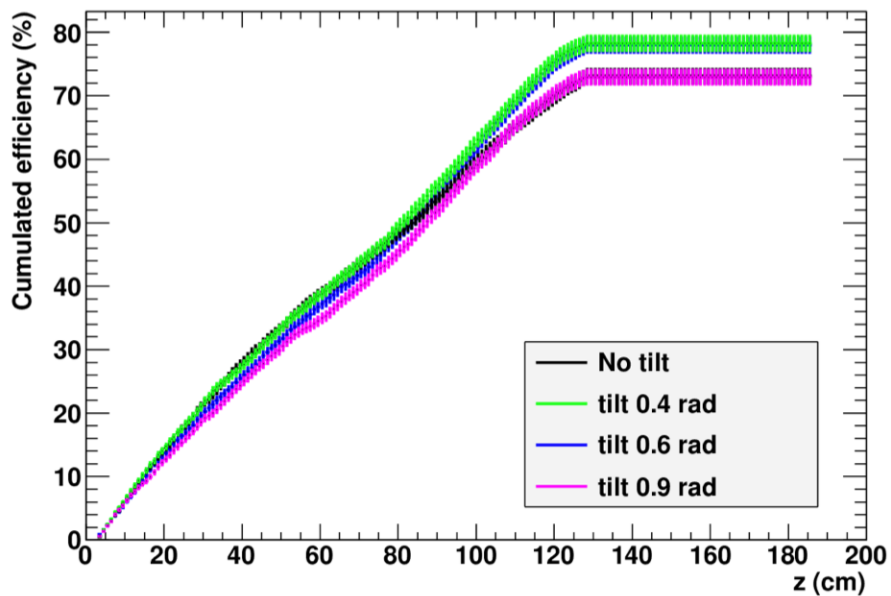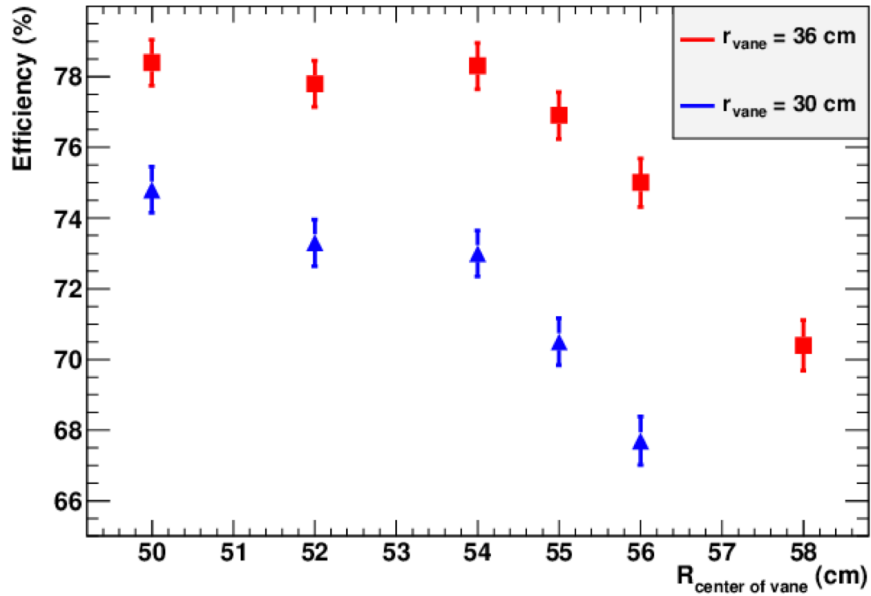Figure A.1: Nominal vane orientation (left) and tilted vane configuration.

Figure A.2: Efficiency, with fiducial cuts (defined in section (4.2)), for four orientation of the tilted vanes.

Another degree of freedom is the position of the axis about which the vane is rotated. Figure A.3 shows the variation of reconstruction efficiency, after fiducial cuts (defined in section (4.2)), as a function of the radial position of the tilt axis for the nominal vane height of 36 cm (78% maximum at 54 cm) and a 30 cm vane with two fewer rows of crystals (maximum 75% at 50 cm).

Figure A.3: Efficiency, with fiducial cuts (defined in section (4.2)), for four orientation of the tilted vanes.

A.2 Disk geometry

The baseline vane geometry for the calorimeter of Mu2e is actually derived from the MECO experiment [16]. It is then natural to explore calorimeter geometries for Mu2e to see whether improvements over the vane geometry are possible as well. The most promising direction appears to be a design based on two disks, spaced apart by one half wavelength of the conversion electron helical trajectory. This design provides improved reconstruction efficiency per unit volume of crystals and can reach absolute efficiency values higher than the vane geometry. Figure (A.4) shows the nominal placement of the two disk calorimeter placed downstream from the tracker.
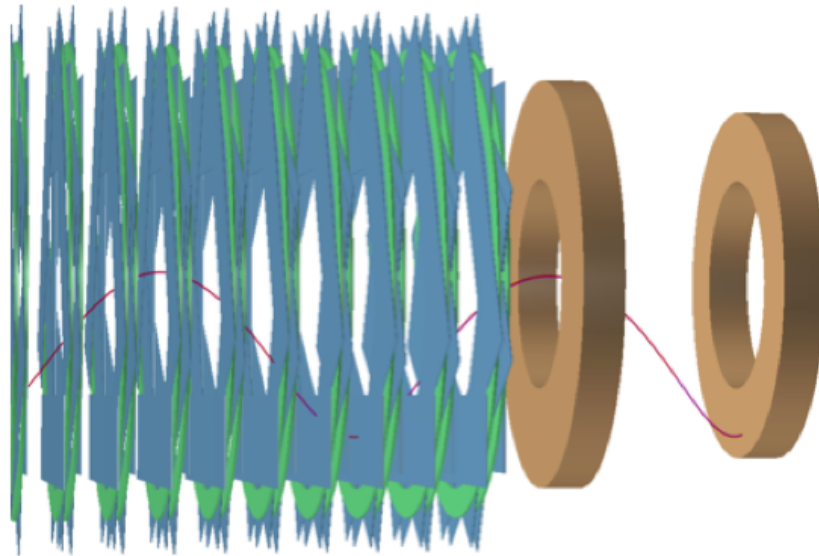
Figure A.4: Two disk calorimeter configuration in position downstream of the tracker.

Figure (A.5) shows that the angle of incidence of conversion electron tracks on the disks is similar to the angle of incidence on the vanes. Thus appropriate clustering algorithms and crystal thickness optimization should be similar for the two options.
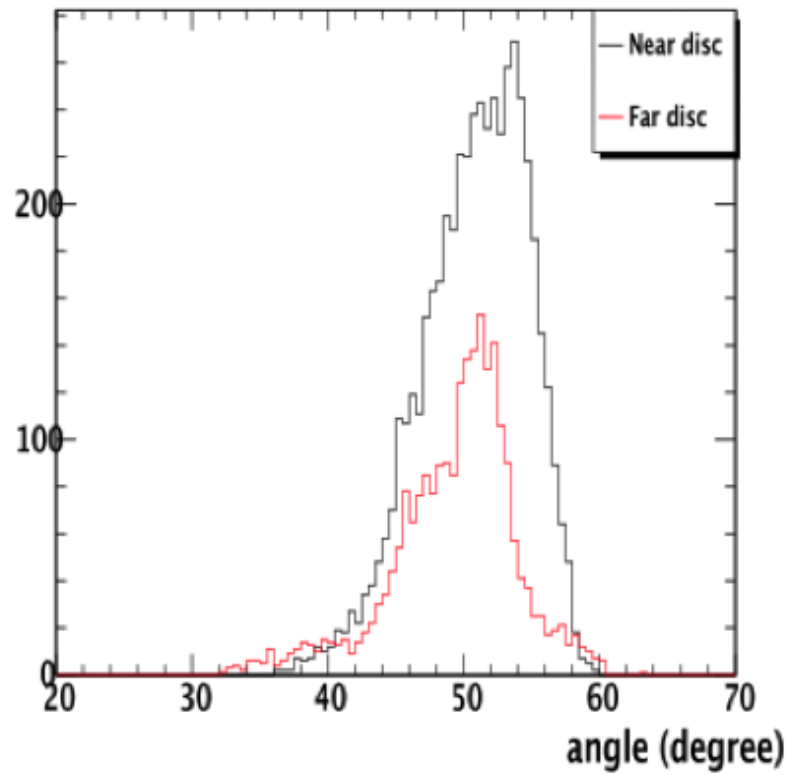
Figure A.5

Assuming that the inner radius of the disks is the same as that for the vanes (36 cm), the outer radius of the two disks does not have to be identical. Figure (A.6) shows the reconstruction efficiency for conversion electrons as a function of the separation between front faces of the two disks, for an outer radius of the near disk of 70 cm, and three choices of outer radii for the far disk.
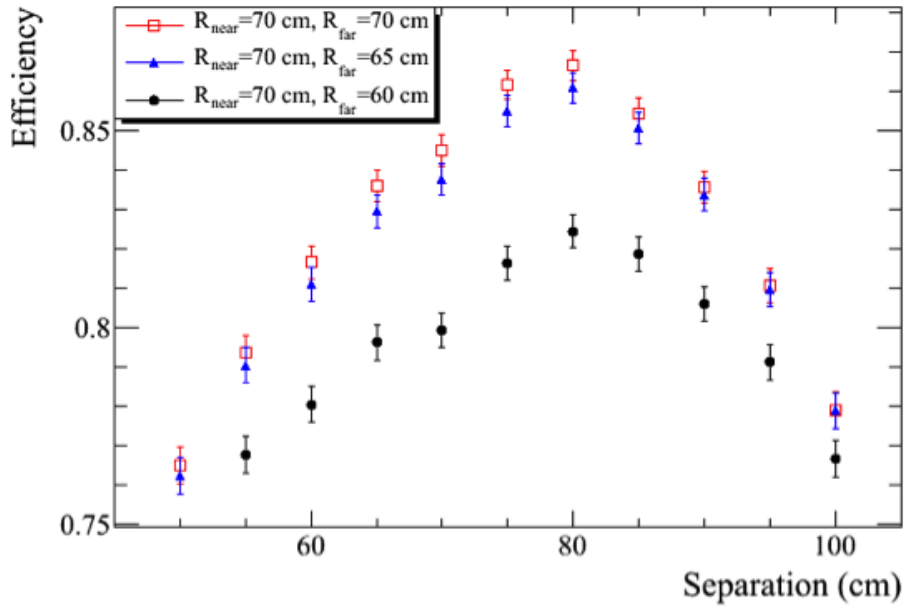
Figure A.6: The reconstruction efficiency for conversion electrons as a function of the longitudinal separation between the front faces of the two disks, for an outer radius of the upstream disk of 70 cm, and three outer radii for the downstream disk.

An outer radius of 70 cm produces an efficiency of 84%, after fiducial cuts (defined in section (4.2)), at a disk separation of 80 cm. Reducing the outer radius to 65 cm lessens the efficiency to 83% but uses a smaller volume of crystals. This is a substantial efficiency gain over the maximum vane efficiency of 78% for four tilted vanes, albeit with an increased crystal volume. This is demonstrated in figure (A.7), which compares the reconstruction efficiency for a variety of four vane and two disk configurations of differing volume. The disks are shown as blue circles, the vanes as red squares. Clearly, at any given crystal volume the reconstruction efficiency of a two-disk design surpasses that of four vanes. In addition, it can be seen that the efficiency of a four vane design peaks at 78%, while the two disk design can achieve an efficiency of as much as 10% higher.
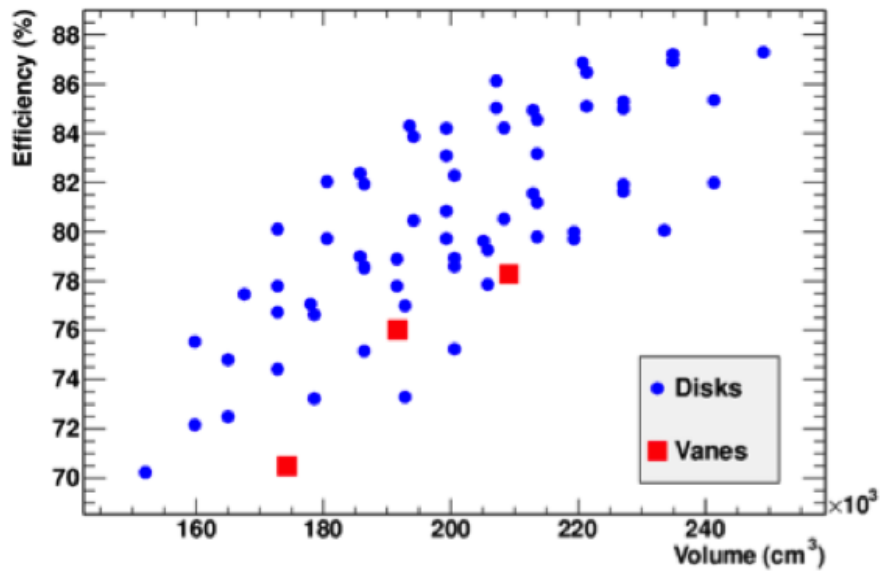
Figure A.7: The reconstruction efficiency for a variety of four vane and two disk configurations of differing volume. The disks are shown as blue circles, the vanes as red squares.
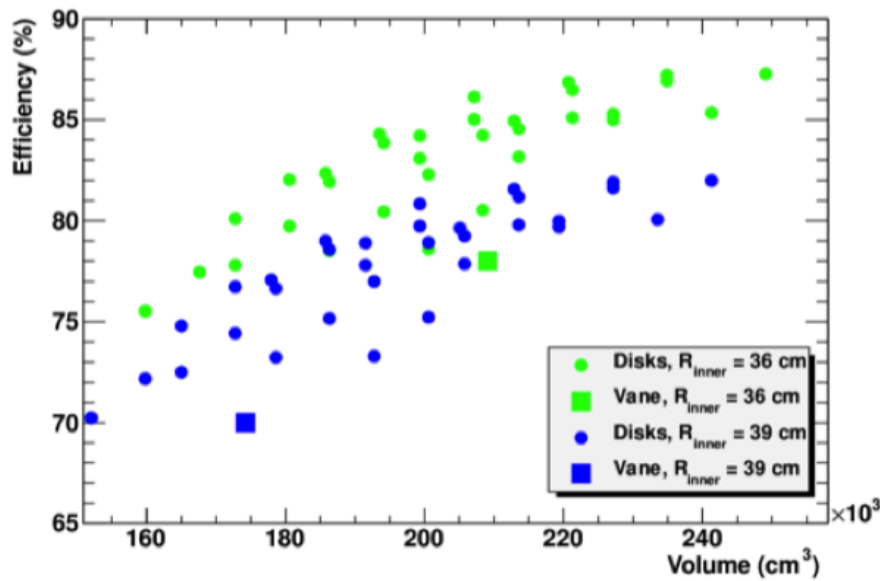

Figure A.8: The reconstruction efficiency of several vane (squares) and disk (circle) configurations.

Since at the inner radius, there is a substantial background from DIO electron tracks, the efficiency was studied increasing the inner radius of the disks and vanes by 3 cm, from 36 cm to 39 cm. The result is shown in figure (A.8), It is clear that again, for a

given volume, the disk design offers higher efficiency.

A.3 PbWO$_4$ crystals

Lead tungstate, PbWO$_4$, which has been used in the CMS [25], ALICE [43] and PANDA [26] experiments has been evaluated as an alternative to LYSO. The light yield from standard lead tungstate is marginal at Mu2e energies. The photon emission spectra have a maximum yield at 420 nm. The CMS experiment measured the light yield of lead tungstate with a standard bi-alkali photomultiplier tube with a quantum efficiency of $\approx 20\%$, to be 8 - 12 p.e./MeV [25] for 23 cm long samples at room temperature. Research & Development carried out by the PANDA experiment over the past decade, in close collaboration with INP Minsk (Belarus) and the technical facilities at the Bogoroditsk Technical Chemical Plant (Russia), has led to the development of a new crystal, PWO-2, with a light yield that is double that of standard lead tungstate. The light yield was increased by improving the quality of the crystal structure and by modifying the lanthanum (La) concentration. PANDA reports that over a large sample of crystals the light yield has been improved to 17 - 22 p.e./MeV [26].

While the light yield of LYSO crystals has only a slight dependence on temperature, PWO-2 crystals have a strong dependence. Variations of 0.2%/°C have been measured for LYSO; -2.5%/°C variations have been measured for PbWO$_4$. A LYSO crystal calorimeter can be operated at room temperature; for use in the 100 MeV regime, a PbWO$_4$ crystal calorimeter must be operated at reduced temperature.

In order to increase the functionality and the energy resolution at low energies, PANDA is designing a calorimeter that will operate at -25°C. The benefits are three-fold:

- The light yield doubles, but is still less than 1% that of LYSO;

- A cooling system provides a means of regulating the crystal temperature to 0.1°C to reduce variations in light output;

- The same cooling system can also be used to cool the APD's to increase their gain and reduce the noise.

The design for the alternative PbWO$_4$-based calorimeter would be similar to the design for PANDA; PWO-2 crystals, cooled to -25°C, with APD's readout, deployed in 4 vanes.

The limiting factor in resolution for a PbWO$_4$ calorimeter will be the electronic noise, which is expected to be of O (1 MeV)/channel. The NYU group from MECO [16] built a system with two $3.0 \times 3.0 \times 13$ cm^3 PbWO$_4$ crystals read out by means of two 13×13 mm^2 RMD APD's and their own charge preamplifier, achieving an ENC of 0.7 MeV and a light yield of 38 p.e./MeV in a cosmic ray test. From these numbers, they estimated an energy resolution of 4.1 MeV at 100 MeV. Moreover, a more dedicated test with a 3×3 matrix of $20 \times 20 \times 200$ mm^3 PWO-2 crystals has been performed by the PANDA collaboration. At 100 MeV, they measure an energy resolution of 5.5 MeV (3.9 MeV) with the crystals cooled to 10 (-25)°C when reading them out with conventional PMTs [26]. A slightly worse result, 7.5 MeV at -25 °C, is obtained when reading out each crystal with a 10×10 mm^2 APD.

A.4 Readout

The second option is to replace the APD's with the new generation large area silicon photomultipliers (SIPM). The SIPM, or Geiger-APD, is a digital device containing a matrix of APD's working in Geiger Mode. Large gains are reached for these devices, of O(106), with functionality close to a conventional PMT. The dark noise of a SIPM is a general concern when running with many pixels. Non-linear response and saturation problems related to the digital nature of the device are additional concerns.

A few large area SIPM's have been tested, including the Hamamatsu MPPC with a 6 $\times$ 6 mm^2 active area and an SMD device (4×4 mm^2) from IRST/FBK (Trento, Italy). The gain has been tested along with the time resolution and rate-dependence when coupled to a LYSO crystal excited with a UV LED. A beam test of a new matrix prototype equipped with Large Area SIPMs is being planned. The results will be compared with beam test measurements already made on an array equipped with APD's.

Appendix B

Temperature fluctuations

Temperature stability is an important element for the development of detector. In this subsection how the temperature fluctuations deteriorates the energy resolution is shown. The LYSO temperature coefficient is (-0.2 ± 0.1) %/C° [31] while the APD-S8664-1010 has a temperature coefficient which is (2.0 ± 0.6)%/C°[25]. The values of these coefficient where extracted from a Gaussian distribution (with mean and standard deviation as shown) for each crystal, and the temperatures of the crystal sample and the readout device where also extracted from two independent Gaussian distributions. In order to understand which temperature stability is required, different simulations were carried out with temperature fluctuations (σ_T) ranging from 0.5 C°to 10 C°; figure (B.1) shows the dependence of the calorimeter resolution as a function of σ_T: The recent beam test performed by the Mu2e Frascati group [14] (with a small
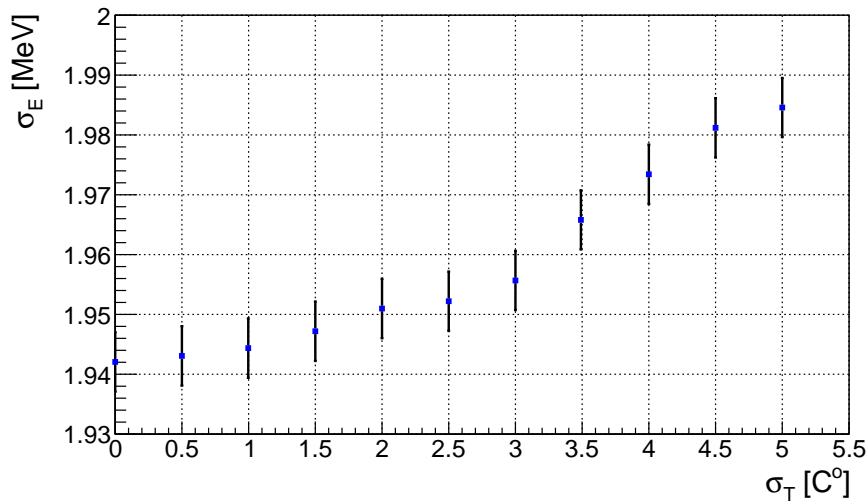

Figure B.1

LYSO prototype and an electronic readout system very similar to the one proposed for the Mu2e calorimeter) reached a temperature stability of 0.5°C; so figure (B.1) shows

asserts that the temperature fluctuations will not be a limiting factor on the energy resolution.

Bibliography

[1] W. Bertl *et al.* A search for $\mu - e$ conversion in muonic gold. *The European Physical Journal C*, 47(2):337–346, 2006.

[2] M. Raidal *et al. Eur. Phys. J.*, C57(13):109–112, 2008.

[3] J. Adam *etl* (MEG Collaboration). An experimental search for lepton flavor violating μ - e conversion at sensitivity of 10^{-16} with a slow-extracted bunched proton beam. *An Experimental Proposal on Nuclear and Particle Physics Experiments at the J-PARC 50 GeV Proton Synchrotron*, 2007.

[4] U. Bellgardt *etal..* Search for the decay $\mu^+ \rightarrow e^+ e^+ e^-$. *Nucl. Phys.*, B(299):1, 1988.

[5] W. Bertl *etal..* A search for $\mu - e$ conversion in muonic gold. *Eur. Phys. J.*, C(47):337, 2006.

[6] J. Adam *etl* (MEG Collaboration). *Nucl. Phys.*, B843(1), 2010.

[7] COMET Collaboration. An experimental search for lepton flavor violating μ - e conversion at sensitivity of 10^{-16} with a slow-extracted bunched proton beam. *An Experimental Proposal on Nuclear and Particle Physics Experiments at the J-PARC 50 GeV Proton Synchrotron*, 2007.

[8] J. Appel *et al. FERMILAB-FN-0904*, 2008.

[9] M. Blanke *et al. JHEP*, 0705(13), 2007.

[10] David Easday. The physics of muon capture. *Physics Reports*, 354:243–409, 2011.

[11] T. Suzuki et al. *Phys. Rev.*, C35(2212), 1987.

[12] Andrzej Czarnecki *et al.* Muon decay in orbit: spectrum of high-energy electrons. *Phys.Rev.*, D84(013006), 2011.

[13] C. Dohmenl *etal.. Phys. Lett.*, B(317):631, 1993.

[14] Mu2e Collaboration. Mu2e Conceptual Design Report. *(unpublished), see Mu2e-doc-1364*, 2012.

[15] Paul C. Bergbusch. Radiative muon capture on Oxygen, Aluminum, Silicon,Titanium, Zirconium, and Silver. page 1, 1995.

[16] MECO Collaboration. Technical report, Brookhaven National Labs. *(unpublished), see MU2E-doc-358.*

[17] Geant4 Collaboration. *Nuclear Instruments and Methods in Physics Research*, A(506):250–303, 2003.

[18] A. Ribon et al. Transition between hadronic models in geant4. *IEEE Nuclear Science Symposium Conference Record*, N(13):89, 2009.

[19] M. G. Catanesi et al. *Phys. Rev.*, C77(055207), 2008.

[20] D. Armutliiski et al. *JINR*, P1(91):191, 1991.

[21] R. Bossert. Requirements and Specifications Documen, WBS 5.9, Neutron Absorbert. *(unpublished), see Mu2e-doc-1371*, 2012.

[22] R. Bernstein. Requirements Document for Mu2e Tracker. *(unpublished), see Mu2e-doc-732*.

[23] R. Bernstein. Calorimeter Requirements. *(unpublished), see Mu2e-doc-864*.

[24] Johannes M. Bauer. The BaBar Electromagnetic Calorimeter: Status and Performance Improvements. *IEEE Nucl. Sci. Symp.*, 2005.

[25] Franco Cavallari. CMS Conference report. 1997.

[26] Panda Collaboration. Panda TDR.

[27] G. Onorato. Upgrade on calorimeter background simulations. *(unpublished), see Mu2e-doc-2297*, 2012.

[28] David Brown. Pattern Recognition Update. *(unpublished), see Mu2e-doc-2082*, 2012.

[29] S. Miscetti. EMC Status and Plans. *(unpublished), see Mu2e-doc-2325*.

[30] C. Grupen and B. A. Shwartz. *Particle Detectors*. Cambridge, 2008.

[31] Ren yuan Zhu *etal.*. A Further Study on Large Size LSO and LYSO Crystal Samples. *IEEE Nuclear Science Symposium Conference Record*, page 1, 2005.

[32] C. Cecchi *etal*. A LYSO Calorimeter for the SuperB Factory. *J. Phys.: Conf. Ser.*, 293(012066), 2011.

[33] William W. Moses. Current trends in scintillator detectors and materials. *NIM*, A(487), 2002.

[34] B.D. Rooney and J.D. Valentine. Current trends in scintillator detectors and materials. *IEEE Trans. Nucl Sci.*, 44(509), 1997.

[35] Ren yuan Zhu et al. Large size lso and lyso crystal scintillators for future high-energy physics and nuclear physics experiments. *Nuclear Instruments and Methods in Physics Research*, A(572):218–224, 2007.

[36] Robert Bernstain. Tracker Requirements Document. *(unpublished), see Mu2e-doc-732*, 2012.

[37] David Brown. SuperB FastSim Status. 2008.

[38] S. Miscetti *et al*. Test of a lyso matrix with an electron beam between 100 and 500 MeV for KLOE-2. *Nucl.Instrum.Meth.*, A617:109–112, 2010.

[39] G. Feldman and R. Cousins. A Unified Approach to the Classical Statistical Analysis of Small Signals. *Phys.Rev.*, D84(013006), 1999.

[40] Giovanni Punzi. Sensitivity of Searches for New Signals and Its Optimization. *PHYSTAT*, 2003.

[41] Gianantonio Pezzullo Luciano Ristori. Progress on sensitivity studies. *(unpublished), see Mu2e-doc-1886*, 2011.

[42] Ivano Sarra. Crystal calorimetry for mu2e. *(unpublished), see Mu2e-doc-908*.

[43] ALICE Collaboration. ALICE TDR.

[44] Ivano Sarra. Various Sensitivity Measures in context of Mu2e Configuration Tuning. *(unpublished), see Mu2e-doc-2124*, 2012.

[45] Ivano Sarra. Simulation Pileup. *(unpublished), see Mu2e-doc-2299*, 2012.

[46] *(unpublished), see Mu2e-doc-1364*, 2012.

[47] *(unpublished), see Mu2e-doc-1087*, 2012.

[48] P. C. Bergbusch *etal.*. Radiative muon capture on O, Al, Si, Ti, Zr, and Ag. *Phys. Rev.*, C59(2853), 1999.

[49] J. A. Bistirlich *etal.*. Photon Spectra from Radiative Absorption of Pions in Nuclei. *Phys. Rev.*, C5(1867), 1972.

[50] Particle Data Group. *Rewiew of particle physics*. Springer, 2010.

[51] Ren-Yuan Zhu *et al*. Large Size LYSO Crystals for Future High Energy Physics Experiments. *Nuclear Science*, 52(6):109–112, 2005.

[52] R. W. Novotny et al. Calorimeter Requirements. *IEEE Trans. Nucl. Sci.*, 57(3):1441, 2010.

Acknowledgments

First of all I would like to thank the Mu2e group, whence I learned the meaning of working in a group and not only with the single group members: Luciano Ristori whose knowledge and experience guided through those months spent at Fermilab; Stefano Miscetti who taught me how much physics one can make, and enjoy it; Giovanni Onorato and Giovanni Francesco Tassielli who taught me how much one can enjoy making physics; Ivano Sarra and Alessandra Lucá, whom, being closer to me in age, I could constantly question without shame on whatever physics topic I was struggling with, and get an answer. Franco Cervelli is named for last only because he deserves a special thanks: he has all these qualities together and is able to show each one at the correct time; but furthermore had the most difficult task of being my advisor.

It was amazing to work with all the physicists of the Mu2e - Fermilab collaboration, but a particularly warm thanks goes to Robert Kutschke, Dave Brown and Robert Bernstain. They helped me in many ways and I really hope that they can enjoy my results.

I also thank Marco Trovato, Stefano Ghelain, Damiano Lupetto for the beautiful time spent together in Chicago (not only in the sushi restaurants!) and for their help on solving the "little-Tony-theorem". An especially thank goes also to the Italian engineers working at Fermilab:Giuseppe Gallo, Donato Passarelli, Paolo Berrutti, Pier Paolo Stabile and Margherita Merio, who introduced me in the "USA" way of life and showed me how magic (and "diffiicile") Illinois can be. I will never forget these months and wherever I will go these memories will make me happy.

My being away from home during these months would have been much more difficult without the love and patience of my parents and of my twin-sister.

In the these five years of preparation I think that a huge number of people crossed my life; all they changed my mind and made me grow up. I had the fortune of having special friends in my native town; Giacomo Citti, Gabriele Pelusio, Sonny Terranova, Luca Santangeli, Tommaso Franchi, Sofia Martini. I consider them as my second family and I really thank them for their patient and their true love.

Another thank goes to my friends living in Pisa; all the emotions an all the experiences I spent with them are like an incredible collection of dreams. Sometimes I really thought that it could not be real! All the hours, days spent in Pisa should not be the same without them. All together we built something that no one can understand and there are no words for explaining it: they supported me and I stressed them like no other.

First I'd like to thank Francesco Muia for the long time spent together during the writing of this thesis and also for the preparation of our Phd tests; than I thank also all my